UNIVERSITA' DEGLI STUDI DI PAVIA

FACOLTA' DI INGEGNERIA
DIPARTIMENTO DI INGEGNERIA INDUSTRIALE E DELL'INFORMAZIONE

DOTTORATO DI RICERCA IN BIOINGEGNERIA, BIOINFORMATICA E TECNOLOGIE PER LA SALUTE
XXXVII CICLO - 2025

ADDRESSING MULTIPLE ASPECTS OF FUTURE RADAR AND TOMOGRAPHIC MICROWAVE DIAGNOSTIC IMAGING

PhD Thesis by

Alessia Cannatà

Advisors:
Prof. Marco Pasian and Prof. Giulia Matrone

PhD Program Chair:
Prof. Silvana Quaglini

Sintesi

Il presente elaborato raccoglie l'insieme delle ricerche condotte e dei risultati ottenuti nel corso del mio percorso di dottorato. Quest'ultimo si è svolto presso i laboratori di Microonde e di Bioingegneria del Dipartimento di Ingegneria Industriale e dell'Informazione dell'Università di Pavia, sotto la guida del Professor Marco Pasian, della Professoressa Giulia Matrone e della ricercatrice Simona Di Meo.

La presente tesi si pone l'obiettivo di affrontare diversi temi legati allo sviluppo di sistemi di imaging innovativi legati all'ambito della diagnostica e basati sull'utilizzo di microonde. Dispositivi di questo tipo sono stati investigati a lungo negli studi esistenti nella letteratura di riferimento, trovando applicazione in contesti oncologici e non. Le principali applicazioni esistenti riguardano la diagnosi precoce del cancro al seno, l'imaging del cervello e in particolare la detezione di ictus ischemici ed emorragici, la diagnosi di malattie ossee e la valutazione di varie condizioni muscolo-scheletriche, la valutazione dell'attività cardiaca. Il vantaggio di maggior rilievo nell'impiego di sistemi di imaging a microonde in ambito clinico riguarda l'utilizzo di radiazioni non ionizzanti. Sistemi come quelli riportati e analizzati nella presente tesi hanno il potenziale di fornire diagnosi accurate sulla base delle proprietà dielettriche rilevate negli organi e/o nei tessuti biologici di interesse, senza causare danni permanenti dal punto di vista cellulare e tissutale, come potrebbe avvenire in seguito all'esposizione a radiazioni ionizzanti, che vengono invece usate in alcune tecniche di diagnostica per immagini attualmente adottate nella pratica clinica.

In questa tesi, due delle applicazioni sopra citate verranno investigate sotto diversi aspetti. In particolare, la prima parte della tesi si concentrerà sullo sviluppo di un sistema di imaging a microonde/onde millimetriche, in ambito oncologico, per la diagnosi del cancro al seno. La prima parte di questa ricerca si occupa di riprodurre e definire materiali adatti (*phantom*) a rappresentare i tessuti di interesse del seno. Verranno approfonditi gli aspetti di caratterizzazione dielettrica di tali phantom e studiata la compatibilità degli stessi a rappresentare i tessuti di interesse anche dal punto di vista di altre proprietà (meccaniche e acustiche), al fine di estendere la loro futura applicazione anche a contesti di imaging multi-modale, che combini le tecniche di imaging a microonde e ultrasuoni. La tecnologia su cui si basa il sistema di imaging a microonde proposto è di tipo *radar*. Vengono curati, quindi, gli aspetti di realizzazione del sistema dal punto di vista hardware e

software, con particolare attenzione all'ottimizzazione dei parametri di scansione, utilizzando due diversi algoritmi di beamforming per ricostruire l'immagine diagnostica a partire dai segnali acquisiti (*Delay and Sum*, DAS e *Filtered- Delay Multiply and Sum*, F-DMAS). Il sistema prevede l'utilizzo di una schiera di antenne lineare in grado di coprire una larga parte dello spettro delle onde elettromagnetiche, da 8 a 40 GHz.

La seconda parte della tesi espone la ricerca e i risultati ottenuti durante una collaborazione di cinque mesi presso il Translational Medical Device Lab dell'Università di Galway, in Irlanda, sotto la guida dei Professori Martin O'Halloran e Adnan Elahi e del ricercatore Bilal Amin. L'applicazione di interesse in questo caso riguarda lo sviluppo di un sistema di imaging a microonde per la diagnosi di patologie ossee, in particolare l'osteoporosi e l'osteoartrite. Il distretto anatomico di interesse per tale studio è il calcagno, vantaggioso per la sua posizione periferica nel corpo umano. Seguendo lo stesso ordine di cui sopra, vengono investigati dapprima i phantom più promettenti da essere impiegati in questo tipo di sistema. Secondariamente, il sistema viene validato numericamente e sperimentalmente. Il sistema proposto differisce dal precedente sia dal punto di vista dell'architettura, in questo caso conforme, sia da quello dell'approccio utilizzato per l'elaborazione dei segnali e la ricostruzione delle immagini diagnostiche, in questo caso l'approccio tomografico. In particolare, verrà dettagliatamente investigato l'algoritmo *Distorted Born Iterative Method* (DBIM) e discussa l'ottimizzazione dei parametri ad esso legati. Le frequenze di lavoro di tale sistema occupano una piccola porzione dello spettro delle microonde, da 1 a 4 GHz.

I risultati ottenuti dimostrano che i materiali sviluppati e i sistemi proposti (basati su due approcci di ricostruzione dell'immagine differenti) possiedono un notevole potenziale nell'ambito della diagnostica clinica non invasiva. La capacità di emulare accuratamente le proprietà dei tessuti biologici, combinata con l'efficacia degli algoritmi di imaging, evidenzia l'innovazione delle soluzioni sviluppate, le quali si dimostrano promettenti tanto per la diagnosi precoce del cancro al seno quanto per la valutazione delle patologie ossee. Questi sistemi, grazie all'utilizzo di radiazioni non ionizzanti e alla versatilità offerta dalle diverse frequenze di lavoro, aprono nuove possibilità per lo sviluppo di tecniche di imaging sicure e accessibili. La presente ricerca rappresenta dunque un importante contributo all'avanzamento delle tecnologie di imaging a microonde, ponendo solide basi per applicazioni future in campo diagnostico e per un miglioramento delle pratiche cliniche attuali.

Abstract

The present work gathers the research conducted and the results obtained during my PhD program, which took place in the Microwave Laboratory and Bioengineering Laboratory of the Department of Electrical, Computer and Biomedical Engineering at the University of Pavia, under the supervision of Professor Marco Pasian, Professor Giulia Matrone and the researcher Simona Di Meo.

The aim of this thesis is to address various topics related to the development of innovative imaging systems for diagnostics, based on the use of microwaves. Devices of this type have been extensively investigated in the existing literature, finding application in both oncological and non-oncological contexts. The main existing applications include early breast cancer detection, brain imaging (particularly in the detection of ischemic and hemorrhagic strokes), bone diseases and various musculoskeletal conditions assessment, as well as cardiac monitoring. The most significant advantage of using microwave imaging systems in clinical settings lies in the use of non-ionizing radiations. Systems like those developed in this thesis have the potential to provide accurate diagnoses based on the dielectric properties detected in the organs and/or in the biological tissues of interest, without causing permanent damage at the cellular or tissue level, as may occur with exposure to ionizing radiation which are instead used in some other medical imaging systems currently employed in the clinical practice.

In this thesis, two of the aforementioned applications will be investigated in detail. In particular, the first part of the thesis will focus on the development of a microwave/millimeter-wave imaging system for breast cancer detection, thus presenting an application in the field of oncology. The first part of this research deals with reproducing and defining suitable materials (*phantoms*) to represent the tissues of interest of the breast. The dielectric characterization of these phantoms will be explored in depth, and their suitability in representing the tissues of interest from the perspective of other physical properties (mechanical and acoustic) will be examined too, with the aim of extending their future application to multi-modal imaging contexts, combining microwave and ultrasound imaging techniques. The technology behind the proposed system is *radar-based*. Thus, the development of the system will be addressed from both hardware and software point of views, with particular attention to the optimization of the scan parameters, using two different beamforming algorithms to reconstruct the diagnostic image from the acquired signals (*Delay and Sum*, DAS, and

Filtered-Delay Multiply and Sum, F-DMAS). The system uses a linear antenna array capable of covering a wide portion of the electromagnetic spectrum, ranging from 8 to 40 GHz.

The second part of the present thesis collects the research and the results obtained during a collaboration with the Translational Medical Device Lab, at the University of Galway, in Ireland, under the supervision of Professor Martin O'Halloran, Professor Adnan Elahi, and the researcher Bilal Amin. The application of interest, in this case, concerns the development of a microwave imaging system for the diagnosis of bone diseases, particularly osteoporosis and osteoarthritis. The anatomical region of interest for this study is the calcaneus, advantageous due to its peripheral location within the human body. Following the same workflow as above, the most promising phantoms to be used in this kind of system will first be investigated. Subsequently, the system will be validated both numerically and experimentally. The proposed system differs from the previous one in terms of its architecture, which is conformal in this case, and in the approach used for signal processing and diagnostic image reconstruction, which is based on tomography. Specifically, the *Distorted Born Iterative Method* (DBIM) algorithm will be investigated in detail, and the optimization of its parameters will be discussed. The operating frequencies of this system occupy a small portion of the microwave spectrum, from 1 to 4 GHz.

The achievements of the whole thesis demonstrate that the developed materials and proposed systems (encompassing two different imaging approaches) possess significant potential in the field of non-invasive clinical diagnostics. The ability to accurately emulate the properties of biological tissues, combined with the effectiveness of the employed imaging algorithms, highlights the innovation of the developed solutions, which prove to be promising for both early breast cancer detection and the assessment of bone diseases. These systems, thanks to the use of non-ionizing radiations and the versatility offered by the different working frequencies, open up new possibilities for the development of safe and accessible imaging techniques. This research, thus, represents an important contribution to the advancement of microwave imaging technologies, laying a solid foundation for future applications in diagnostic fields and for the improvement of current clinical practices.

Contents

List of figures

List of tables

Chapter 1

Introduction

1.1. Biomedical imaging for diagnostics purposes: focus on breast cancer detection and bone health assessment

Biomedical imaging plays a fundamental role in many steps of the current healthcare, including diagnosis, assessment of the response to a specific therapy and guided treatment and surgery [1]. Its main advantage is to provide a representation (often non-invasively) of the investigated organs or anatomical structures of interest. In many medical contexts, the possibility of using biomedical imaging for screening or diagnosis purposes may help in detecting anomalies within the human tissues and preventing surgery.

Nowadays, biomedical imaging holds a crucial importance in medical science, encompassing a range of techniques. This field utilizes various imaging technologies, including X-ray radiography, X-ray computed tomography (CT), ultrasound echography (US), endoscopy, magnetic resonance imaging (MRI), magnetic resonance spectroscopy (MRS), positron emission tomography (PET), thermography, medical optical imaging, as well as single-photon emission computed tomography (SPECT) [2]. The aforementioned technologies are currently involved in the identification of all major medical conditions including trauma, various types of cancer, cardiovascular diseases, neurological disorders, and numerous other health issues.

In breast cancer screening, which is of main interest within the present thesis, the early detection of tumors is of paramount importance since it strongly influences the quality of life and the life expectancy of the patient after the process of diagnosis and treatment. Breast cancer occurs in every country worldwide in women of any age, with increasing probability in later life. According to the *World Health Organization* (WHO), 2.3 million women were diagnosed with this cancer and 670 000 deaths were recorded

in 2022. For this reason, it is fundamental to control the incidence and prevalence of this pathology. Screening investigations allow for the recognition of this cancer before the appearance of any sign or symptom related to the disease. In particular, the early detection of such pathology demonstrated to determine a 90% five-year survival rate [3]. X-ray mammography is primarily used for early breast cancer detection even though it has several limitations, firstly due to the employment of ionizing radiations. Further, the procedure requires breast compression, which can cause pain or discomfort for the patient. Additionally, it is challenging to differentiate tumors in dense breast tissues since both appear echogenic in mammogram images. This can result in false positives, leading to unnecessary and often invasive follow-up tests, such as biopsies. Although mammography involves a small amount of radiation exposure, the risk is generally considered negligible compared to the benefits of early detection.

Also ultrasound imaging is largely used in breast cancer screening and diagnostic, since it can overcome some of the limitations related to X-ray mammography. Overall, ultrasound is a widespread imaging technology employed in diagnostic laboratories and clinics for many medical applications. It is free from radiation exposure risk, relatively cheaper, non-invasive and highly portable compared to other imaging techniques. This kind of clinical investigation is normally adopted as a supplementary screening technique to mammography in women with dense breasts. Breast ultrasonography is normally performed in a frequency range between 5 and 15 MHz, since it allows for a good trade-off between resolution and penetration depth in such a superficial organ [4].

Another application of ultrasound in this field is represented by ultrasound elastography. Specifically, it was developed in the 1990's with the aim to image a map of the tissues' stiffness, in such a way to reproduce the manual palpation performed by clinicians [5].

Nonetheless, both the ultrasound-based techniques described above suffer from a strong dependence to the operator ability, which constitutes their main limitation. This is primarily due to the fact that often the applied stress cannot be controlled and quantified.

The overall adopted screening practice, encompassing both X-ray mammography and ultrasound techniques, demonstrated to achieve successful outcomes in decreasing the deaths rate recently. Specifically, breast cancer mortality showed a 40% drop between the 1980s and 2020 in high-income countries. Countries that have succeeded in reducing breast cancer mortality have been able to achieve a reduction of 2–4% per year.

Beyond the first discussed screening/diagnostic question related to breast cancer detection, the second topic of interest of this thesis falls out of the oncological field. Specifically, the diagnosis and assessment of musculoskeletal conditions represents the second subject which will be discussed over this thesis. Musculoskeletal health refers to the functionality of the locomotor system, which includes muscles, bones, joints, and surrounding connective tissues. Musculoskeletal conditions include over 150 different diseases and issues that affect this system, leading to temporary or

permanent limitations. These conditions are typically associated with chronic pain and reduced mobility. Pain in the musculoskeletal structures is the most prevalent type of non-cancer-related pain. In the framework of the present thesis, in particular, the diagnosis of osteoporosis and osteoarthritis will be presented. Nowadays, in clinical routine, the dual-energy X-ray absorptiometry (DXA) is used to quantitatively assess the bone mineral density (BMD). Nonetheless, it presents limitations, again, firstly due to the employment of ionizing radiation, which may cause long-term effects on the tissues, as well as the low portability of equipment. On the other hand, quantitative computed tomography (QCT), which can provide good-resolution images of the regions of interest, is less used in the clinical routine for bone disease detection because it employs high-intensity X-ray doses, involving even very expensive equipment [6].

The limitations of the listed techniques for both the discussed diagnostic questions, primarily related to the health risk given the employment of ionizing radiations, can be overcome by the use of novel techniques based on microwave (MW) and millimeter (mm)-waves.

Microwave imaging is an alternative method based on non-ionizing electromagnetic (EM) signals working over the frequency range between hundreds of megahertz to tens of gigahertz. Low health risk, low-cost resources, ease of use and non-invasiveness are among the advantages brought about by this technology. Microwave imaging has been recently explored in the fields of cancer detection, blood clot detection, brain stroke detection, cardiac imaging and bone imaging, suggesting promising results in imaging the anatomical regions of interest.

The present thesis will discuss several aspects of the development, characterization and evaluation of microwave/millimeter-wave imaging systems for the two mentioned diagnostic questions. The objective of this thesis is to deeply investigate different facets of novel imaging systems, with the aim of bridging the gap between the current state-of-the-art of the development and future applications closer to the medical practice.

More in detail, this thesis will address the design of the tissue-mimicking phantoms (which will be introduced in Section 1.2 and further in Chapter 2) and the optimization of two different imaging systems and algorithms (some details about the employed imaging approaches are provided in Section 1.3 while an in-depth analysis on their applications will follow in Chapter 3 and 4). Specifically, the thesis is organized as follows:

Chapter 2 will deal with the realization and tailoring of tissue-mimicking phantoms aimed at emulating multiple physical properties of the human breast tissues. This part of the research was meant to develop suitable phantoms to be employed within the validation of experimental multi-modal imaging systems based on information about both the dielectric and mechanical/acoustic properties of the breast tissues, in order to combine diverse characteristics of the same tissues and get highly reliable diagnoses.

Chapter 3, instead, will analyze in detail the realization of a microwave/millimeter-wave radar-based imaging prototype for biomedical applications, with a major focus on breast cancer detection. In particular,

both the creation of the hardware structure and the optimization of the software aspects will be faced. The performance of the proposed system has been evaluated by using numerical and experimental phantoms, which were previously characterized in Chapter 2.

Finally, **Chapter 4** will investigate another application of microwave imaging (i.e., the tomographic approach) in the field of bone health assessment. Even in this Chapter, both numerical and experimental phantoms have been involved to validate the proposed system and imaging algorithm.

1.2. Phantoms' role in diagnostic imaging

Phantoms are defined as versatile tools, models or materials which are used in many medical fields to reproduce the physical or behavioral characteristics of real biological tissues or organs. The employment of phantoms within the development and the testing of new technologies in the biomedical field, is a crucial step since biological samples are not always available for both ethical and practical reasons [7]. Phantoms allow for the reproduction of the desired characteristics of a tissue or an anatomical region within the human body. Within the literature, several examples of phantom models have been reported. Specifically, phantoms can be designed both as experimental (i.e., tissue-mimicking materials (TMMs)) or numerical models, according to their intended functionality. The main advantage in dealing with experimental phantoms relies in the fact that very often they can be obtained through low-cost, safe and easy-to-manage resources [8].

Concerning the development of various tissue-mimicking experimental phantoms, many studies have been conducted with the aim to reproduce diverse properties of various human tissues [8], [9], [10], [11], [12], [13], [14], [15], [16], [17]. One of the main distinctions that could be observed between the reported examples of phantoms within the literature refers to their composition and consistence. Depending on the final application, it may be advisable or required to develop liquid, solid or 3D-printed phantoms, realized through varying ingredients. Several works in the existing literature have reported detailed reviews on phantoms of various categories. To date, as an example, phantoms for microwave, ultrasound, magnetic resonance, mammography and computed tomography imaging have been deeply explored, showing that the most common recipes to obtain solid TMMs are gelatin-based, agar-based, polyvinyl alcohol (PVA)-based, or silicon-based [14], [18], [19]. 3D-printed phantoms, instead, are usually obtained through polylactic acid (PLA) or acrylonitrile butadiene styrene (ABS) filaments. Finally, liquid phantoms, are mostly based on mixtures of water and simple powders, like sucrose or sodium chloride, or chemical formulations (which may be toxic, as ethylene glycol) [20].

Among the main aims of this thesis, there was initially the development of suitable phantoms for microwave imaging. Thus, the dielectric properties of these phantoms needed to be tuned to the properties of the corresponding

human-tissues. To assess such properties, phantoms needed to undergo dielectric characterization. In this thesis, mostly, water-based tissue-mimicking phantoms have been exploited for both the emulation of the breast and bone tissues properties. Such kind of phantoms has been adopted since the dielectric properties of human tissues are strongly related to the water content of the tissues themselves. Hence, water-based phantoms allowed for the fine reproduction of the desired dielectric properties by tailoring the percentage content of water and other ingredients within the mixtures.

In particular the tissue-mimicking breast phantoms involved in this thesis have been obtained through oil-in-gelatin/oil-in-agar mixtures, as already done in previous works [8], [9], [11], [13], [21], resulting in solid phantoms. This even allowed to create multi-layered phantoms with various shapes and dimensions. After assessing the dielectric validity of the developed breast phantoms, some of them have been modified in such a way to be suitable to represent even the mechanical and acoustic properties of the corresponding breast tissues, making them multi-modal phantoms according to such properties. Chapter 2 will discuss in detail the production, the dielectric, mechanical and acoustic characterization of such phantoms as well as the procedure leading to the realization of phantoms with a more complex geometry. The main novelty introduced by this part of the thesis relies in the fact that suitable phantoms have been realized that are able to reproduce at the same time three different physical properties of the corresponding healthy and diseased human breast tissues.

The developed bone tissue-mimicking phantoms of the present thesis, instead, were obtained by employing Triton-X 100-based mixtures. In this case, the phantoms were meant to be liquid. This kind of phantoms have been already explored in multiple studies [16], [22], [23], [24], [25], aimed at mimicking the properties of bone, breast and head tissues. The choice of developing liquid mixtures has been made based on a list of advantages, such as the opportunity to store and reuse the materials, the stability of their dielectric and rheological properties and their quick realization. Moreover, the project of this thesis on bone microwave imaging implied, for practical reasons, the production of liquid phantoms. Indeed, for imaging purposes a 3D-printed plastic mold has been used, which had subtle layers that could only be filled by liquid phantoms.

As a further investigation in terms of realization of bone phantoms, during the thesis, even solid carbon black-based phantoms have been employed [17], [26], [27], which even served as molds to contain liquid Triton-X mixtures. Further details regarding the models, comprising solid and liquid phantoms, employed in this investigation will be discussed in Chapter 4.

Thus, the wide range of diverse materials available for developing phantoms is highly suitable for representing a variety of human tissues. In particular, tissues of varying water content can be emulated, allowing for the reproduction of the properties of both soft and extremely dense biological tissues, mimicking both healthy and diseased conditions. This characteristic makes them extremely convenient and versatile in the biomedical field when

biological samples are not available. The importance of phantoms relies in the fact that they represent reliable, accurate and reproducible models, with known characteristics, which can be exploited for imaging purposes in the early stages of the development of novel imaging systems.

1.3. Microwave and millimeter-wave imaging in oncology and other contexts

As previously mentioned, in Section 1.1, to date, several systems based on microwave and millimeter-wave frequencies have recently arisen, gaining interest among the researchers, since they provide a series of advantages compared to the currently used biomedical imaging techniques. Particularly, microwave imaging (MWI) offers a safe and non-invasive alternative for the diagnosis of functional and pathological tissue conditions. The working principle of such technique involves mapping the internal structure of an object (i.e., an anatomical region) using electromagnetic fields at microwave frequencies (300 MHz – 30 GHz) [28]. Even millimeter (mm)-wave imaging has been spreading recently involving applications working at tens of gigahertz.

In particular, microwave imaging systems are normally composed by multiple antennas constituting an array, which can be either linear or conformal depending on the application. A transmitter emits EM signals that pass through the object to be imaged and are detected by receivers positioned along the designed array. When a significant change of the dielectric properties occurs, scattering phenomena affect the propagation of the incident wave. This may alter the amount of detected energy. The final 2D or 3D images are then formed using the information contained within the collected signals at the receivers [3], [29], [30]. Normally, the collected information refers to a *scattering matrix* (or S-matrix), which is used as a tool to describe how the electromagnetic field interacts with a material or system (i.e., with phantoms in the case of this thesis and, in the future, with biological systems). Each element in the scattering matrix represents the amplitude of the wave scattered from one antenna element to another and it is defined for the frequencies between the selected range for a specific application (making it three-dimensional).

Thus, the scattering matrix provides information on how energy is scattered or transmitted when it encounters an object. As an example, for a two-antenna system, at a certain fixed frequency the scattering matrix S can be written as:

$$S = \begin{bmatrix} S_{11} & S_{12} \\ S_{21} & S_{22} \end{bmatrix} \tag{1.1}$$

where S_{11} represents the reflection coefficient at antenna 1, S_{22} represents the reflection coefficient at antenna 2, S_{12} represents the transmission

coefficient from antenna 2 to antenna 1 and S_{21} represents the transmission coefficient from antenna 1 to antenna 2.

The process described above allows for different methods of creating microwave images. Among them, applications concerning the reflection approach and the transmission-reflection approach, which are schematized in Figure 1.1, will be discussed in this thesis. The next sections provide an in-depth analysis of these approaches with respect to the imaging methods adopted over this thesis. In particular, the radar and the tomographic approaches will be discussed in detail.

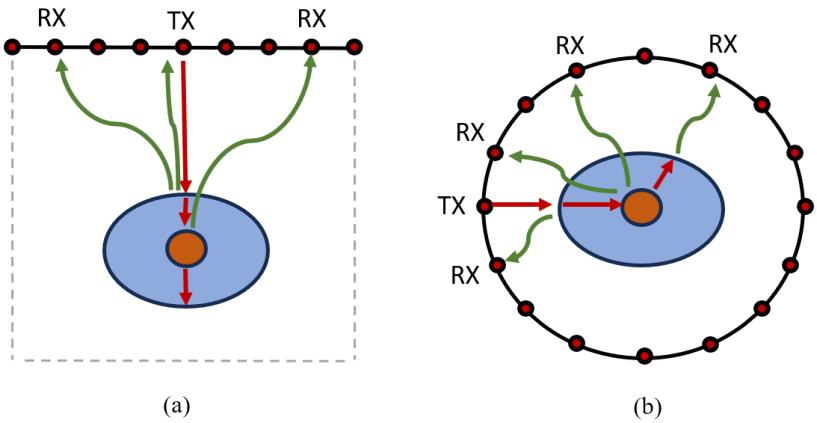

Figure 1. 1: Basic microwave imaging principle determining two different approaches: reflection imaging (a) and transmission-reflection imaging (b). Red arrows represent the incident waves, while the green ones represent the scattered waves. Blue and orange regions refer to objects with different dielectric properties.

1.3.1. Radar reconstruction techniques

The radar approach for image reconstruction is a particular application of reflection imaging. It is common to refer to radar-based imaging approaches as *qualitative imaging* [30]. Indeed, in many medical applications, the primary goal of imaging is not to map and quantify the dielectric properties of the various tissues but rather to detect and localize the presence of anomalies. This is fundamental in oncological applications, especially in the phase of screening and early detection. Radar imaging has been explored mostly in breast cancer detection [31], [32], [33], [34], even though multiple studies have been focusing on non-oncological applications including brain stroke detection [35], [36], [37] and cardiac monitoring [38], [39]. Within the mentioned applications, ultra-wideband (UWB) signals are normally employed in such a way to have a good time resolution. Basically, each antenna of the array transmits a short pulse at a time (UWB in the frequency domain) and the backscattered response is received by the same antenna (mono-static configuration). Recently, multi-static imaging approaches have been introduced, which exploit both the reflected and the transmitted scattering parameters [40].

In the framework of this thesis, a new radar-based system for breast cancer detection will be explored. As already mentioned, the dielectric properties of biological tissues may differ a lot according to their water content. Moreover, different studies in the literature have shown that the permittivity of tumor tissues is nearly 10-20% greater than that of the healthy breast tissues [28], [40]. Thus, radar-imaging in breast cancer detection exploits the fact that a large dielectric contrast exists between normal and malignant tissues. This is due to the fact that in normal conditions the breast is mostly fat. When anomalies occur, instead, a rapid growth and proliferation of abnormal cells may lead to masses formation which influence blood perfusion of an organ altering its dielectric properties. For this reason, tumors have higher dielectric properties compared to fatty and fibro-glandular breast tissues, making them easily detectable even when small [28].

In comparison to other systems and architecture, UWB radar-imaging in breast cancer detection brings several advantages, including:

- ease to implement and low computational effort, since it does not involve solving an *inverse scattering problem* to reconstruct the complete dielectric profile of the object of interest, as in tomographic approaches;
- good resolution: radar-based imaging systems allow for a resolution of less than 5 mm, which is sufficient to detect and localize a tumor at the early stages;
- good specificity in discriminating between malignant or benign lesions: this is due to the different strength of the scattered waves from benign and malignant tissues. Benign tumors have similar dielectric properties to normal tissues, but lower than those of malignant tumors.

Most of the applications in this field work in the frequency range between 1 a 10 GHz [3]. Nonetheless, recently, some millimeter-wave imaging systems have been proposed, which can provide better resolution (due to the employment of EM waves with higher frequencies) at the cost of reduced penetration depth [41], [42], [43]. In [41] the authors developed a mm-wave imaging system for breast cancer detection working at a frequency of 30 GHz demonstrating that a penetration depth of a few centimeters can be achieved. Moreover, the findings of this work showed that both a linear and a conformal system layout can be adopted achieving good results in detecting targets in numerical and experimental breast phantoms.

In the present thesis, specifically in Chapter 3, a similar radar-based imaging system for future application in breast cancer detection has been realized. The proposed system has been characterized and validated through the use of numerical and experimental breast phantoms (previously designed in Chapter 2). Three different frequency bands (i.e., X-band (8-12 GHz), Ku-band (12 GHz-18 GHz) and K/Ka-band (18-40 GHz)) have been adopted for the investigations on the performance of the system, covering a wide band of the electromagnetic spectrum up to millimeter waves. To obtain the final images, the *Delay and Sum* (DAS) and the *Filtered-Delay Multiply and Sum*

(F-DMAS) beamforming algorithms have been used. These two algorithms have been deeply investigated and their parameters have been optimized to obtain reliable diagnostic images within the novel imaging system working up to the millimeter wave frequency range. Further details about the employed imaging algorithms, as well as the working principles of the beamformers will be discussed in Chapter 3.

1.3.2. Tomographic techniques

On the opposite to radar-imaging, the tomography approach represents an example of *quantitative imaging* [30]. Indeed, microwave tomography (MWT) can be defined as a method that produces two-dimensional (2D) images (*tomos*, from the Greek word for "slice") of the dielectric properties of an object of interest. This approach is already employed in other established imaging technologies, as magnetic resonance and X-ray computed tomography. Thus, the internal representation of the 3D human body is given to the user as a series of slices (2D images) along a determined axis.

This approach provides a quantitative map of the distribution of various tissues dielectric properties (relative permittivity and conductivity). Thus, tomography allows for the collection of information about the presence, position and even the properties of the elements included in the field of view. This facet suggests that the described approach deals with the quantification of the properties of a known region rather than the detection of a possible target. This implies its utilization even out of the context of oncology.

In MWT systems, typically, the object to be imaged is surrounded by a bounded domain where the antennas of the array are placed, as illustrated previously in Figure 1.1 (b). Such architecture of the system is related to the fact that, within this approach, as already mentioned, transmission-reflection scattering parameters are used to form the final image. An EM signal is transmitted by one antenna and received by multiple antennas after passing through the object of interest. The incident wave, when encountering different interfaces (thus dielectric discontinuities), is scattered in several directions. This implies resolving an *inverse scattering problem* [3], [28], [30], [44], which is intrinsically ill-posed and non-linear. This results in being computationally more expensive, time-consuming and subjected to scattering errors with respect to radar-based imaging approach. Several quantitative methods have been proposed to solve this problem iteratively, in order to minimize the error between the measured field and the expected one [45], [46], [47], [48], [49], [50].

The described imaging approach has been widely investigated in breast cancer detection [47], [51], [52], diagnosis of breast stroke [53], [54], [55], cardiac imaging [56] and bone diseases diagnosis [25], [49], [50], [57], [58], [59].

In the framework of this thesis, microwave tomography approach has been adopted in the context of bone health assessment, particularly related

to the detection of pathologies as osteoporosis and osteoarthritis. As already mentioned, these conditions alter the inner microscopic structure of the bones resulting in a variation of their dielectric properties. Chapter 4, in particular, will discuss about the numerical and experimental validation of a MWT imaging system for the imaging of the human calcaneus. A conformal array of nine antennas have been employed without the use of any matching medium, surrounding a 3D model which resembled in shape, dimension and properties to the human calcaneus. The 1-4 GHz frequency band has been adopted for the dielectric characterization and imaging acquisitions and the reconstructed images have been achieved around 3 GHz as already done in previous works in both breast and bone imaging [25], [60], [61]. A combination between the Distorted Born Iterative Method (DBIM) and an Iterative Method with Adaptive Thresholding for Compressed Sensing (IMATCS) has been employed to solve the *inverse scattering problem*, reaching promising results in terms of reliability of the reconstructed dielectric properties. The findings of this part of the study demonstrated that the combination of the proposed microwave imaging system and the imaging algorithm are suitable to obtain accurate mapping of the properties of the proposed bone phantoms. An in-depth analysis of the employed imaging prototype, phantoms and imaging algorithms will be presented in Chapter 4.

Chapter 2

Design and characterization of multi-modal tissue-mimicking breast phantoms

2.1. Background

Breast cancer is one of the most common cancers among women worldwide. The early diagnosis is fundamental in order to increase the effectiveness of the treatment and, consequently, reduce the mortality related to this pathology. Nowadays, the most widespread imaging techniques for breast cancer screening are X-ray mammography and ultrasound (US) imaging. Moreover, several techniques (e.g., magnetic resonance imaging (MRI), computed tomography (CT)) are available in clinical routine to study breast anomalies in depth. Currently, also microwave and millimeter (mm)-wave imaging techniques are spreading in this context and some prototypes and methods have already been proposed [42], [61], [62], [63], [64], [65]. This imaging modality allows to overcome some limitations given by the more common techniques mentioned above. As an example, the greatest advantage is the use of non-ionizing radiations, as opposed to X-ray imaging. Microwave (MW) and millimeter-wave (mm-wave) imaging systems are capable to provide images with a very good contrast between healthy and tumor tissues. This is possible as breast tissues in physiological conditions are mostly fat, while the neoplastic components show a high blood perfusion and their behavior is affected by the water content in the frequency range of interest. To experimentally validate and test this kind of systems, the dielectric properties of tissues should be investigated first. There are several works concerning the dielectric characterization of *ex-vivo* breast tissue samples [66], [67], [68], [69], [70]. However, for ethical and practical issues,

it is not always possible to conduct measurements on biological samples and tests on artificial phantoms are more convenient. Several experimental campaigns on breast tissue-mimicking phantoms were conducted as well [8], [9], [10], [11], [71] to determine their dielectric properties (i.e., the real and imaginary part of the dielectric permittivity). The most commonly used experimental setup is composed by a network analyzer (VNA) able to perform measurements in a desired range of frequencies, connected to an open-ended coaxial probe which is put in direct contact with the sample under test.

Moreover, it is useful to consider also the mechanical properties of breast tissues, as it is known that tumor tissues are harder than healthy ones [72]. This is due to the fact that, in case of tumor, the normal architecture of cells and tissues is disrupted. This disorganization, along with changes in cell adhesion and mechanical properties, contributes to an overall increase in tissue stiffness.

With ultrasound (US) imaging modalities (e.g., US B-mode imaging and US elastography), it is possible to investigate the morphology of the anatomic region of interest and achieve quantitative information related to the stiffness of tissues using non-ionizing mechanical waves. Thus, by combining US with MW imaging it would be possible to obtain complementary information to improve the accuracy of the diagnosis.

Indeed, multi-modal phantoms play a prominent role in this context, as they could be able to mimic, at the same time, different physical properties (e.g., the dielectric, the mechanical and acoustic ones) of human breast tissues. In the literature, there are only a few examples of works in which multimodal phantoms for microwave/mm-wave imaging and ultrasound have been developed [13], [14], [15], [73]. Most of the works usually focus on the characterization of one of the mentioned US related properties (mechanical or acoustic). Those concerning the mechanical characterization of phantoms are mainly interested in evaluating the Young's modulus or, in some cases, the mechanical contrast between couples of different mimicked tissues [7], [12], [13], [21]. The most common way to measure the mechanical properties of interest is the unconfined compression test, performed by a press with a fixed plate and a mobile one. Usually, this system provides to the user the force-displacement curve, through which it is possible to calculate the Young's modulus.

The acoustic properties, instead, are investigated in terms of US wave speed, US attenuation and backscattering coefficient [74], [75], [76], [77], [78], [79]. One of the most widely used measurement approaches is the insertion technique, which involves a differential method using water as the reference medium [80]. Measurements are usually carried out through the pulse-echo approach, in which a single transducer is used both as a transmitter and as a receiver.

Within this Chapter, an overview on the design, production and characterization of the dielectric, mechanical and acoustic properties of multi-modal breast phantoms is provided. In the literature, there is a limited

number of works concerning the characterization of more than two properties of breast phantoms developed for MW/mm-wave and US imaging. Works on multi-modal phantoms more frequently address other imaging modalities [81], [82], [83], [84]: in [81], for example, a review on both geometric and anthropomorphic phantoms for combined PET and MRI is reported. Moreover, in [82], the authors developed a heterogeneous PVC breast phantom obtained by 3D printing and evaluated its characteristics using mammography, MRI and US imaging.

Even when phantoms for US imaging are considered, acoustic and mechanical properties are often investigated singularly, as under appropriate assumptions the Young's modulus can be calculated from the US shear wave speed [85]. As can be noticed, the literature lacks of works concerning the simultaneous dielectric, mechanical and acoustic characterization of phantoms (Table 2.1). Even when all these properties are considered, the experimental conditions are not always declared. To make the procedures reproducible, proper guidelines on the employed measurement methods, experimental settings and also regarding the shape and dimension of the phantom samples should be provided.

Table 2. 1: Properties of breast phantoms characterized in several works in the literature.

	Type of characterization			
	Dielectric	***Mechanical***	***Acoustic***	***Other***
Akki et al., 2014 [12]	x	x		
Henin et al., 2015 [13]	x	x		
Ng et al., 2019 [86]		x	x	
Ruvio et al., 2020 [14]	x		x	MRI, CT, X-ray
Di Meo et al., 2021 [7]	x	x		
Li et al., 2021 [15]	x		x	
Cannatà et al., 2022 [73]	x	x	x	
Di Meo et al., 2022 [87]	x	x		

Since there are still some open points regarding both the definition of the measurement protocols and the standardization of phantoms for characterization and imaging, the aim of this Chapter is to address the limitations in terms of the production and characterization procedures in which bi-modal and multi-modal phantoms for combined microwave and ultrasound imaging are involved. In particular, the following sections collect the results achieved by different investigations conducted over multiple projects and collaborations. The main aim, at the beginning, was to design and characterize bi-modal (i.e., dielectric and mechanical) tissue-mimicking breast phantoms. To do this, diverse materials have been created and large

experimental campaigns have been conducted. The dielectric characterization aimed to cover a part of the spectrum as large as possible (up to 50 GHz), to ensure the compliance of the proposed phantoms with the reference breast tissues over both the microwave and the mm-wave frequencies. Regarding the mechanical characterization, instead, the main objective was to establish clear experimental conditions, to fill the existing gap in literature. Hence, different combinations of the fundamental parameters involved in the mechanical tests have been explored and promising results have been achieved.

At the same time, for a small group among the developed materials a further analysis has been conducted as well to assess the impact of the ingredients of the mixtures on the investigated properties. In this phase some tissue-mimicking phantoms have been modified to reach improved mechanical properties.

Subsequently, the proposed bi-modal phantoms underwent acoustic characterization to evaluate whether they could be suitable even to represent the acoustic properties of the corresponding human tissues. Two of the proposed materials were found to be compliant with the breast tissues properties from a multi-modal point of view.

Finally, some multi-layer heterogeneous planar or conformal phantoms are presented, intended to be used as a model to develop and test microwave imaging systems for breast tumor detection.

The results of the study also proved the time-stability of the properties of the proposed mixtures. Thus, these works evaluated the overall validity of the materials in mimicking the desired physical tissues properties and their possible application in the development of anatomic 3D breast models to be imaged through novel microwave imaging devices.

2.2. Realization of tissue-mimicking phantoms: recipes and preparation

In this framework, a large number of tissue-mimicking breast phantoms have been produced and characterized. Starting from the recipes proposed by a previous study on dielectric characterization of breast phantoms [8], during the present thesis a total of 18 different materials have been realized with the aim of mimicking different physical properties of healthy and tumor breast tissues. All mixtures were based on low-cost, non-toxic and easy-to-handle components: deionized water, sunflower seed oil, dishwashing liquid, and gelatin, agar or waste-oil hardener as solidifying agents. In [8], particularly, the authors designed and characterized different materials trying to mimic the dielectric properties of the human healthy and diseased breast tissues in the frequency range of 0.5-50 GHz. Due to the large variability of the properties of the healthy breast tissues, the “healthy phantoms” have been split into three different categories mimicking the corresponding tissues based on their adipose percentage content. In

particular, phantoms were designed to mimic low-density (i.e., >80% fat content), medium-density (i.e., 20%-80% fat content), and high-density (i.e., <20% fat content) breast tissues. The goal of the present study, instead, was to specifically modify and tailor the previously proposed tissue-mimicking materials to assess whether they could be suitable to represent even other physical tissues properties (i.e., mechanical and acoustic properties). All the proposed multi-modal phantoms were originally designed to match the desired dielectric properties of the corresponding human breast tissues according to an estimation of the expected dielectric permittivity of each mixture, based on the percentage content of water and oil given by the Bruggeman formula [8], [88]:

$$p\frac{\varepsilon_{oil}-\varepsilon_{eff}}{\varepsilon_{oil}+\varepsilon_{eff}}+(1-p)\frac{\varepsilon_{water}-\varepsilon_{eff}}{\varepsilon_{water}+\varepsilon_{eff}}=0 \quad (2.1)$$

where ε_{water} represents the permittivity of water, ε_{oil} is the permittivity of sunflower seed oil, ε_{eff} is the permittivity of the mixture and p is the concentration of sunflower seed oil within the mixture. Indeed, each ingredient, based on its percentage content within the mixture, may potentially influence the properties of the final phantom.

As shown in [21], as an example, small percentages of gelatin do not have a significant impact on the variation of dielectric properties of the produced mixtures. Nonetheless, a first attempt to reproduce the mechanical properties of breast tissues showed that a slight increase in the percentage of gelatin is not enough to reproduce the mechanical properties of breast tissues [89]. Therefore, the recipes proposed in [8] have been further modified aiming to reliably mimic, at the very first stage, the mechanical properties of breast tissues, both healthy and diseased.

Specifically, at first, the amount of gelatin was considerably increased and both the dielectric and mechanical properties of the resulting phantoms were measured. In particular, the volume percentage of gelatin was increased up to the point where either the mixture was no longer able to mix and solidify, or the dielectric properties of the produced mixture fall below one standard deviation from the average value of human *ex-vivo* breast tissues.

Moreover, the phantoms mimicking human breast neoplastic tissues underwent a further analysis, with the objective to make a comparison between the performance of two different solidifying agents (i.e., gelatin and agar) and to quantify the influence of the fat percentage content (i.e., sunflower oil) within the mixture on the dielectric and mechanical properties.

The next step consisted of the characterization of the acoustic properties of the obtained bi-modal (i.e., dielectrically and mechanically compliant) phantoms. In this context, it was necessary to introduce new ingredients within the proposed recipes to make the phantoms acoustically compliant against the corresponding human breast tissues. In particular, agar was considered as solidifying agent since it allows for the control of specific

acoustic parameters (e.g., the speed of propagation of the ultrasound wave through the medium based on its percentage content [76]).

The proposed recipes are a modified version of those presented in [8]. Table 2.2 shows all the phantoms produced with the corresponding ingredients quantities. The acronyms in the second column refer to the volume percentage of gelatin (G), agar (A) and waste-oil hardener (K), and sunflower oil (O) in the mixture. The total volume considered to compute the percentages reported in the acronyms was given by the overall amount of liquid ingredients (i.e., water and oil). For example, G3.3O66.6 indicates that the volume percentage of gelatin and oil are 3.3% and 66.6%, respectively.

In particular, phantoms ranging from #1 to #11 have taken part to the first step of the project, aiming to test their bi-modal compliance against the human breast tissues. Phantoms ranging from #12 to #17 have been specifically realized to assess the influence of the type of solidifying agent on the dielectric and mechanical properties of the produced materials and finally, phantom #18 was designed to mimic even the acoustic properties of a malignant breast tissue. The investigation of the properties will be further explained within the next sections of this Chapter.

Table 2. 2: Composition of phantoms mixtures.

	Mixture	**Mimicked breast tissue**	**Deionized water (ml)**	**Gelatin (g)**	**Sunflower oil (ml)**	**Dishwashing liquid (ml)**
1	G3.3O66.6	Low-density	68	6.8	136	3.8
2	G4.9O66.6	Low-density	68	10	136	3.8
3	G5O50	Medium-density	68	6.8	68	3.8
4	G7.35O50	Medium-density	68	10	68	3.8
5	G9.55O50	Medium-density	68	13	68	3.8
6	G6.6O33.3	High-density	68	6.8	34	3.8
7	G9.8O33.3	High-density	68	10	34	3.8
8	G12.74O33.3	High-density	68	13	34	3.8
9	G8O20	Malignant	68	6.8	17	3.8
10	G16O20	Malignant	68	13.6	17	3.8
11	G21.17O20	Malignant	68	18	17	3.8
#	**Mixture**	**Mimicked breast tissue**	**Deionized water (ml)**	**Agar (g)**	**Gelatin (g)**	**Sunflower oil(ml)**	**Dishwashing liquid (ml)**
12	A6O5	Malignant	95	6	-	5	3

13	A6O15	Malignant	85	6	-	15	3	
14	A6O20	Malignant	80	6	-	20	3	
15	G6O5	Malignant	95	-	6	5	3	
16	G6O15	Malignant	85	-	6	15	3	
17	G6O20	Malignant	80	-	6	20	3	
#	**Mixture**	**Mimicked breast tissue**	**Deionized water (ml)**	**Agar (g)**	**Sunflower oil (ml)**	**Dishwashing liquid (ml)**		**Waste-oil hardener (g)**
18	A6K0.6O20	Malignant	80	6	20	3		0.6

The protocol for preparing the mixtures is hereby described. The procedure is analogous to that proposed in [7], [8], [73]. The setup for preparing the phantoms consists of:

- a precision digital balance (VWR) with a resolution of 0.01 g;
- two hot-plate magnetic stirrers (ARE Hot Plate Stirrer, VELP SCIENTIFICA);
- several graduated 250 ml beakers, cylinders and an electric pipettor.

The phantoms have been obtained as follows: the solidifying agent (i.e., gelatin or agar), previously weighted with the digital balance, is slowly added to the beaker containing water. The mixture is stirred constantly and heated to a temperature of 85°C using a hot plate magnetic stirrer. During this procedure, it is preferable to cover the beaker with an aluminum foil to prevent water from evaporating. This process takes from 10-15 minutes to an entire hour depending on the amount and the type of solidifying agent to dissolve within the water. This phase is considered complete only when the solution appears clear. Subsequently, the beaker is moved to another magnetic stirrer and cooled; the stirring continues and, while the solution reaches a temperature of 65°C, the sunflower seed oil is heated to the same temperature. When the contents of both beakers reach 65°C, the one containing the oil is poured into the one containing the water in which the solidifying agent has been dissolved. At the same time, the surfactant (i.e., the dishwashing liquid) is introduced into the mixture to obtain a uniform emulsion. This phase is the most delicate, as it determines the homogeneity of the final product. The mixture is then allowed to cool until the temperature drops below 50°C. Subsequently, the resulting product is poured into a mold and allowed to solidify at room temperature (approximately 25°C) for about 3 hours before performing dielectric measurements. Figure 2.1 shows the setup for preparing the phantoms.

For what concerns the phantom #18, containing a small amount of waste-oil hardener, instead, the only difference within the whole procedure is that this ingredient is supposed to be poured into the beaker where the oil is.

During the whole project, before performing measurements, the temperature of all the phantoms was always checked using an infrared thermometer: as much as possible, efforts were made to standardize the measurement by conducting the dielectric characterization of all the phantoms at room temperature.

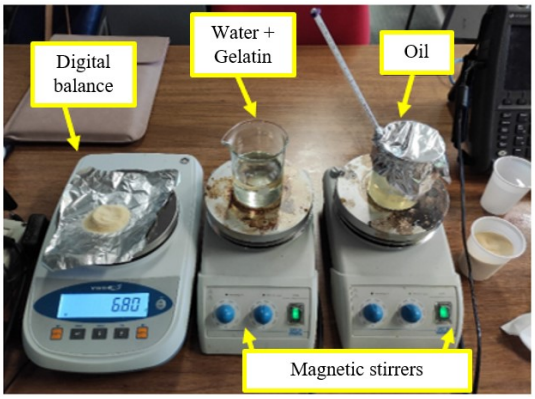

Figure 2. 1: Mixtures preparation.

2.3. Experimental setups for characterization

2.3.1. Dielectric measurements

The first aim of the study implied the dielectric characterization of the realized tissue-mimicking breast phantoms. The experimental setup used to measure the dielectric properties of all phantoms consisted of:

- an open-ended coaxial probe (Keysight 85070E Dielectric Probe Kit), able to provide reliable dielectric measurements in the frequency range from 0.2 to 50 GHz and for temperatures from −40 °C to 200 °C;
- a FieldFox Handheld Microwave Analyzer (Keysight N9916A, 14 GHz), able to perform measurements from 30 kHz to 14 GHz;
- a high-precision flexible coaxial cable (provided with the Keysight 85070E Dielectric Probe Kit), to connect the probe to the FieldFox Analyzer;
- a mechanical probe holder, to keep the probe position fixed for the whole measurement session;
- a mechanical mover, to put the sample and the probe in contact, avoiding any kind of undesired movement of both the probe and the coaxial cable after calibration;
- a laptop to get the dielectric measurements and process experimental data.

In Figure 2.2 (a), a picture of the experimental setup for the dielectric characterization of the produced phantoms is shown.

The calibration of the system has been performed through the measurement of the properties of three known loads (i.e., air, short circuit and deionized water) to get more reliable properties from the samples under test. Three measurements in different position and depth from each sample were

acquired, in order to assess the homogeneity of the produced tissue-mimicking materials, as shown in Figure 2.2 (b).

As mentioned above, the dielectric properties (i.e. the real and imaginary part of the complex dielectric permittivity ε) of the produced phantoms were measured up to 14 GHz according to the limit of the instrumentation. Since one of the aims of this study was to design suitable phantoms even for millimeter-wave imaging, the Cole–Cole single-pole model [90] has been employed, to predict the frequency dependence of the measured properties up to 50 GHz:

$$\varepsilon = \varepsilon'(\omega) - j\varepsilon''(\omega) = \varepsilon_\infty + \frac{\varepsilon_S - \varepsilon_\infty}{1+(j\omega\tau)^{1-\alpha}} + \frac{\sigma_S}{j\omega\varepsilon_0} \tag{2.2}$$

where ε_s and ε_∞ indicate the dielectric constant at zero and infinite frequencies, respectively, τ is the time constant, $\omega = 2\pi f$ is the angular frequency, α is a shape factor ranging from 0 to 1, and σ_S is the static conductivity. Specifically, the Cole–Cole parameters were derived using the least squares method. Such method is considered as one of the most reliable fitting tools to describe the relaxation mechanisms which occur in biological tissues when stimulated with electromagnetic field. The Cole-Cole equation allows to interpolate the measured permittivity and conductivity and model the behavior of frequency-dependent materials in a desired frequency range, even beyond 50 GHz [91].

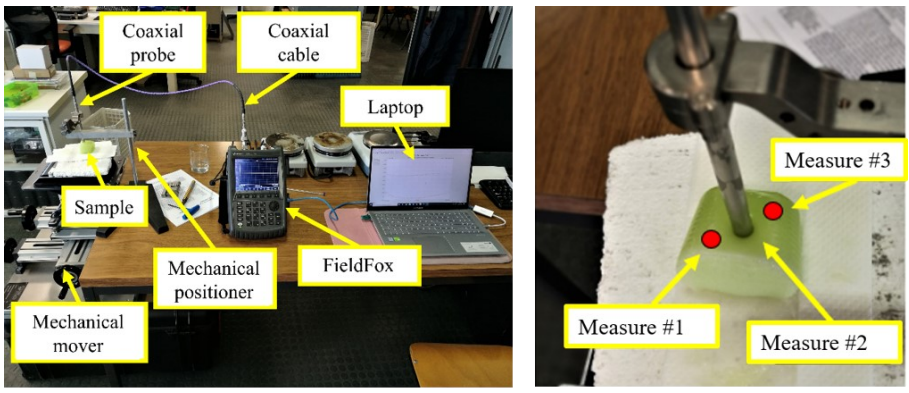

Figure 2. 2: Experimental setup for dielectric measurements (a); sample under test with three measurements sites (b).

2.3.2. Mechanical measurements

In the context of the mechanical characterization of biological breast samples, the main objective is to get a measurement of the stiffness (i.e., Young's modulus) of the material under test. Breast tissues, in particular, are extremely subject to changes throughout a woman's life. Their diverse composition normally undergoes physiological mutations over time. The development of neoplastic anomalies can also modify the morphological and functional conformation of the mammary organ and influence its mechanical

parameters. Tumor masses, in fact, are stiffer than mammary tissues under physiological conditions: they often appear as nodules harder than the surrounding tissues [72]. Manual palpation techniques, as a matter of fact, are currently widely practiced for the diagnosis of breast cancer.

In this thesis, unconfined compression was chosen among different techniques (i.e. unconfined compression, confined compression and indentation) for measuring the mechanical properties of the phantoms, as it is the most widely used technique in the literature for measuring samples of this type [12], [21], [92], [93]. In this method, a load is applied to the sample, that is held between two metallic plates, larger than the surface area subjected to the load, and a lateral deformation of the sample is allowed. The experimental setup used for mechanical measurements consisted of:

- an electromechanical traction/compression machine equipped with precision guide columns (MTS Insight 10, MTS System Corporation);
- a load cell of 250 N maximum capacity (MTS Load Cell);
- a digital controller for fine-tuning the crosshead position;
- two aluminum compression plates: the lower one is fixed and the upper one moves in accordance with the movement of the crosshead;
- a computer, to monitor the compression test in real time with the TestWorks software.

In Figure 2.3, a picture of the experimental setup used for the mechanical characterization of the produced phantoms is shown. Samples were derived from each phantom using a standard cylindrical mold with a diameter (d) of 28 mm and a height (l_0) of 10 mm, as shown in Figure 2.4. Mechanical measurements were done on samples at room temperature [72], [94], [95], [96], [97], [98], [99], [100].

The goal of such measurements is that of deriving the Young's modulus from the force (f)– displacement (l) curves achieved as output from the traction/compression machine. In particular, from the force–displacement curves, the stress (σ)–strain (ε) curves were derived in this way:

$$\sigma = f/A \tag{2.3}$$

$$\varepsilon = \Delta l/l_0 \tag{2.4}$$

where $A = \pi d^2/4$ is the area of each sample, d is the diameter of the sample, and $\Delta l = l_0 - l$ is the difference between the initial (l_0) and the final length of each sample.

The literature related to the mechanical properties of phantoms, as well as that of human breast tissues, does not show clear and unambiguous guidelines for the determination of the stiffness (e.g. the Young's modulus). However, in order to properly know this property as well as to achieve comparable and reproducible results, it is fundamental to know the impact of the experimental conditions on the measurements. Consequently, in this paper, the impact of preload and test speed on the mechanical properties of phantoms was quantitatively evaluated. The test speed refers to the speed of the movable plate of the electro-mechanical press. The preload represents

the force threshold from which the compression test formally starts. This experimental condition does not affect the mechanical response of the material under test. Indeed, it is basically a method to focus in different zones of the stress–strain curve (which may result in different Young's modulus values). Specifically, mechanical measurements of phantoms ranging from #1 to #11 were made considering different combinations of preload (0.1 N, 0.2 N, and 0.4 N) and test speed (0.5 mm/min, 1 mm/min, 2 mm/min) as described in Table 2.3, in which PL stands for preload and TS stands for test speed. In [21], where similar phantoms were considered, preloads of 0.1 N and 0.2 N together with a test speed of 0.5 mm/min were used. Thus, this analysis started from these same values.

Particularly, the experimental condition referring to 0.2 N preload and 0.5 mm/min test speed (i.e., PL02TS05) has been chosen as preferred for the ancillary investigations of the main project, since other directions were not found across the literature. In [21], indeed, gelatin- and agar- based tissue-mimicking materials were employed to mimic the mechanical behavior of healthy and diseased breast tissues, allowing for a comparison against the results achieved by the present thesis.

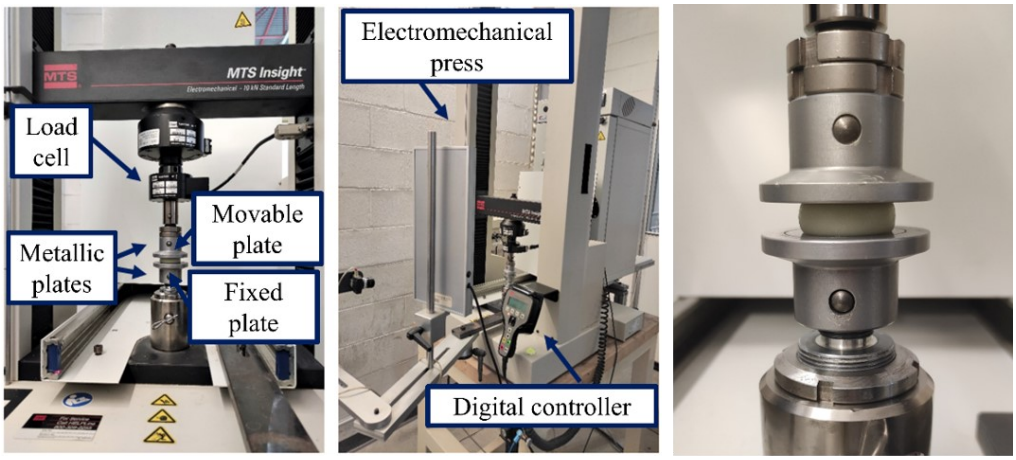

Figure 2. 3: Experimental setup for mechanical measurements: setup components (a), overview of the electromechanical press (b) and unconfined compression applied to the sample (c).

Figure 2. 4: Samples derived from the G8O20 (top) and G16O20 (bottom) phantoms, numbered to indicate the different mechanical measurement conditions under which they were tested. For both the G8O20 and G16O20 sample '1' was measured with 0.4 N preload and 2 mm/min test speed (PL04TS2); sample '2' was measured with 0.2 N preload and 2 mm/min test speed (PL02TS2); sample '3' was measured with 0.2 N preload and 1 mm/min test speed (PL02TS1); sample '4' was measured with 0.4 N preload and 1 mm/min test speed (PL04TS1).

Table 2. 3: Experimental conditions for the mechanical characterization of phantoms.

Test	Preload (N)	Test speed (mm/min)
PL04TS2	0.4	2
PL02TS2	0.2	2
PL02TS1	0.2	1
PL04TS1	0.4	1
PL02TS05	0.2	0.5
PL01TS1	0.1	1
PL01TS05	0.1	0.5

2.3.3. Acoustic measurements

The last step of the project explained in the present Chapter aimed at the acoustic testing of the realized and characterized tissue-mimicking materials, to assess whether they could reproduce even the acoustic properties of the corresponding human breast tissues. Thus, the developed bi-modal phantoms (those ranging from #1 to #11) underwent acoustic characterization.

The acoustic measurements were carried out using the insertion technique, which involves a differential measurement method, employing water as the reference, to study the propagation of ultrasonic waves through solid media in an aqueous environment [80]. A pulse-echo approach with an US linear array probe (model LA533, Esaote s.p.a., Florence) was performed using an almost square active aperture of 24 elements. The probe was connected to the ULA-OP research system [101]. A connection with a PC is required for the data storage and elaboration. The processing of the signals, indeed, was done with MATLAB (The MathWorks, Natick, MA, USA). A 10-cycle sinusoidal burst was used in transmission. A metal plate (reflector) was placed at the focal depth (i.e., 23 mm) and the received radiofrequency signals were acquired with and without the phantom sample in place. In Figure 2.5 (a) the experimental setup is shown. Acquisitions were carried out at three different points along the phantom sample diameter, in order to assess the robustness of the measurements within the same sample. The measurements were performed at six different frequencies (5-10 MHz, with a 1 MHz step size) in order to estimate the speed of sound in the material under test and its ultrasound attenuation.

Actually, only a single material among the healthy tissue-mimicking phantoms was found able to reproduce at the same time the dielectric, mechanical and acoustic properties of the human low-density tissues (i.e., phantom #2: G4.9O66.6). For what concern the tumor-like materials, none of them revealed comparable properties against the corresponding biological tissues. For this reason, an agar-based material has been introduced (i.e., phantom #18: A6K0.6O20) since it has been proved that this ingredient allows for the tuning of the ultrasound speed through the medium [73], [75], [76], [102].

At least 10 samples for each of the two materials and for each frequency were acoustically characterized, for a total of 154 samples. A representation of the shape and dimension of the samples is given in Figure 2.5 (b). The speed of sound (m/s) within the medium under test was calculated as follows:

$$c_{ph} = c_w / \left(\frac{\Delta t}{2h} * c_w + 1\right) \tag{2.5}$$

where c_w = 1480 m/s is the speed of sound in water, Δt is the delay between the received signal with and without the sample in place and h is the known thickness of the sample (in centimeters). The attenuation (dB/cm), instead, was estimated as:

$$\alpha = \frac{1}{2h} 20 log_{10}\left(\frac{A_w}{A_{ph}}\right) \tag{2.6}$$

where A_{ph} and A_w are the spectrum amplitude at the frequency of interest, with and without the sample in place, respectively.

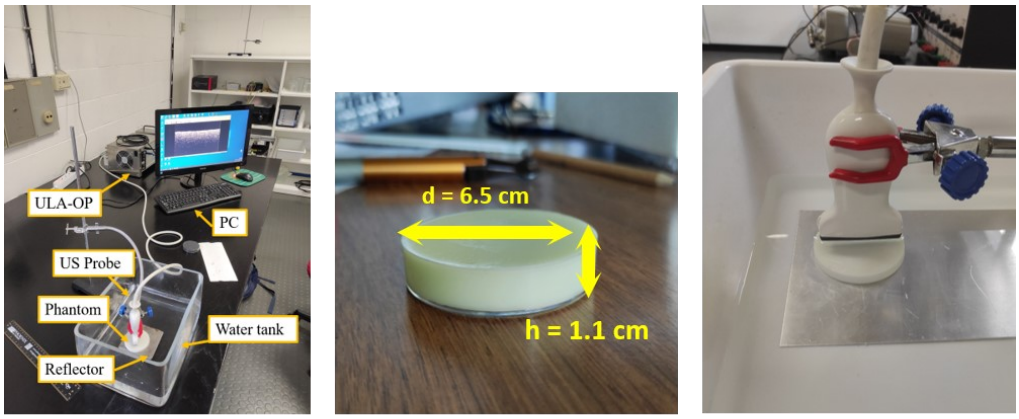

(a) (b) (c)

Figure 2. 5: Experimental setup for acoustic measurements in pulse-echo configuration (a), sample dimensions (b) and zoom on the sample under test (c).

2.4. Achieved results

2.4.1. Dielectric properties of the produced phantoms

2.4.1.1. Impact of gelatin on bi-modal phantoms dielectric properties

The impact of gelatin on phantom dielectric properties had already been evaluated in [8] for small volumetric increases and has been shown not to drastically affect the mixture dielectric properties. However, these small increases of gelatin concentration were not enough to mimic the mechanical properties of breast tissues [89]. For this reason, within this project, more significant increases in the gelatin volume percentage were evaluated, and the impact on dielectric properties was continuously monitored. In particular, each of the phantoms ranging from 1# to 11# was replicated 3 times (i.e., 33 phantoms) and dielectric measurements were conducted on each of these phantoms at 3 independent points along the diagonal of the phantom for homogeneity assessment, as described in [8]. Thus, 99 dielectric measurements were conducted from which the average was computed (i.e., for each of the 11 phantom types, the average was calculated over 9 dielectric curves).

Specifically, as an example, in Figure 2.6 the real and imaginary part of the phantom dielectric permittivity at 6, 10 and 14 GHz as a function of the gelatin volume percentage is shown for all tissue-mimicking phantoms from #1 to #11. These graphs, divided based on the different phantoms' category (i.e., low-, medium-, high-density, malignant), show a decreasing trend of the dielectric properties of the mixtures as gelatin increases. Comparing these values with those of *ex-vivo* breast tissue dielectric permittivity at 10

GHz, as reported in Table 2.4, it can be observed that they are always in the range of one standard deviation from the average dielectric properties of the target tissues.

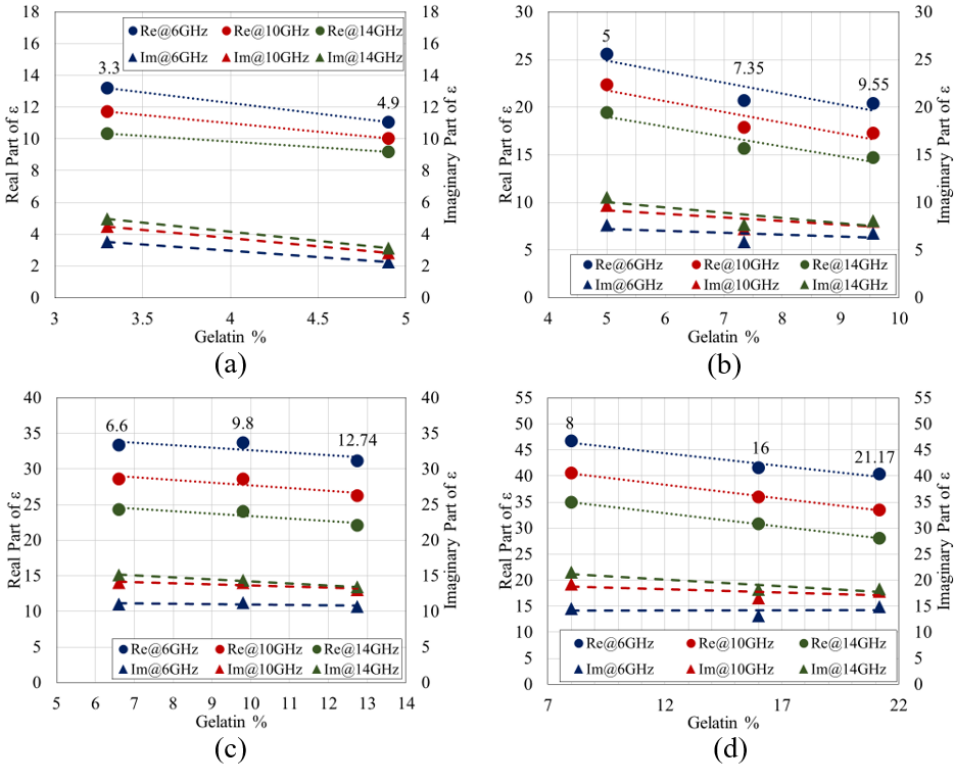

Figure 2. 6: Trend for real (dot markers) and imaginary part (triangle markers) of dielectric permittivity at 6, 10 and 14 GHz for the 4 categories of tissue-mimicking breast phantoms (i.e., low-density (a), medium density (b), high-density (c)) and malignant (d) tissue-mimicking phantoms)- as a function of the gelatin percentage volume. The dotted and the dashed lines indicate the linear trend of dielectric permittivity as a function of gelatin percentage.

Table 2. 4: Dielectric properties of breast *ex-vivo* tissues.

	ε' @ 10 GHz (mean ± standard deviation)	ε'' @ 10 GHz (mean ± standard deviation)
Low-density	9.87 ± 10.19	3.35 ± 5.32
Medium -density	22.01 ± 13.08	9.93 ± 7.28
High-density	32.85 ± 12.25	16.05 ± 6.92
Malignant	39.29 ± 7.17	19.43 ± 4.36

2.4.1.2. Cole-Cole parameters of the bi-modal phantoms

The Cole-Cole parameters have been estimated to describe the dielectric behavior of the proposed tissue-mimicking materials (phantoms ranging from #1 to #11) up to 50 GHz. Their average values for all phantoms are shown in Table 2.5. To show the quality of the fitting procedure, two extreme cases were chosen, i.e. G4.9O66.6 and G21.17O20, and the comparison between measured and fitted curves is reported in Figure 2.7 (a) and (b) for the real and imaginary part of ε, respectively. The Cole–Cole parameters for each of the 11 phantom types were derived by considering the average of the 3 independent measurements made on each of the 3 replicates of the phantom (as explained above). Then, for each phantom type the average between 9 measurements was made and, from this, the Cole–Cole parameters were derived.

Table 2. 5: Cole-Cole parameters of all the produced phantoms.

Mixture	$\Delta\varepsilon$	ε_∞	τ (ps)	α	σ_s (S/m)
G3.3O66.6	13.73	1.95	7.5	0.198	0.055
G4.9O66.6	11.09	2.06	5.5	0.315	0.036
G5O50	25.9	4	8.5	0.13	0.152
G7.35O50	20.6	4.2	9	0.19	0.09
G9.55O50	25.82	0.5	8.05	0.261	0.1
G6.6O33.3	35.44	3.61	8.95	0.095	0.195
G9.8O33.3	39.18	2.02	8.61	0.165	0.171
G12.74O33.3	37.96	1.03	8.67	0.195	0.172
G8O20	50	3	8	0.08	0.304
G16O20	40.85	7.15	9.1	0.082	0.313
G21.17O20	42	8	12	0.1	0.25

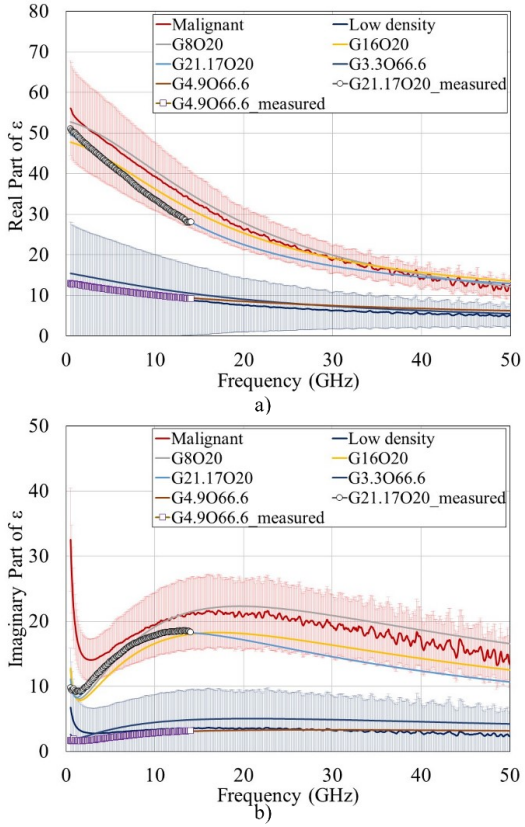

Figure 2. 7: Comparison between the fitted dielectric properties of the produced phantoms (G3.3O66.6, G4.9O66.6, G8O20, G16O20 and G21.17O20) with the measured dielectric properties of low-density and malignant human breast *ex-vivo* tissues (derived from **[70]**): (a) real part and (b) imaginary part of $\boldsymbol{\varepsilon}$. Shaded regions indicate a standard deviation from the mean value of the dielectric properties of *ex-vivo* tissues (derived from **[70]**). The dielectric properties of the produced phantoms were fitted up to 50 GHz by the Cole–Cole model. The lines with circles and squares indicate the dielectric properties of the G4.9O66.6 and G21.17O20 phantoms measured up to 14 GHz.

2.4.1.3. Investigation on the influence of the solidifying agent on the dielectric properties

Phantoms ranging from #12 to #17 were specifically designed to monitor both the role of the type of solidifying agent within the mixture and that of the percentage amount of the fatty component (i.e., sunflower seed oil). In this section an analysis of the results referred to the dielectric measurements conducted on these phantoms is presented.

A similar experimental setup has been employed for the dielectric characterization except for the fact that a vector network analyzer (ENA Network Analyzer E5080B) able to perform measurements from 100 kHz to 44 GHz has been adopted as a new purchase, used instead of the FieldFox Handheld Microwave Analyzer (Keysight N9916A, 14 GHz).

Thus, all measurements were acquired from 500 MHz to 40 GHz. A minimum pressure on the sample under test was applied, to ensure a perfect contact between the tip of the probe and the sample itself, avoiding any leakage of liquids from the phantom. For each phantom, three independent measurements were performed to assess the mixture homogeneity. Both real and imaginary part of the complex dielectric permittivity were measured and compared to those of human breast *ex-vivo* malignant tissues [70]. The dielectric properties of the phantoms involving oil percentages from 15% to 20% fall within one standard deviation from the mean values obtained for human breast *ex-vivo* malignant tissues, both for the real and imaginary part of the dielectric permittivity, as shown in Figure 2.8 (a) and (b), respectively. In these figures, only the average values for all phantom samples are shown. As can be seen from the picture, the two phantoms with 5% percentage content of oil (phantoms #12, #15), regardless of the type of solidifying agent, exhibited higher dielectric properties than the reference values from *ex-vivo* data. The other developed mixtures with oil percentages from 15% to 20% (i.e., phantoms #13, #14, #16, #17), are instead able to mimic the dielectric properties of malignant breast tissues in all the investigated bandwidth, regardless of the solidifying agent.

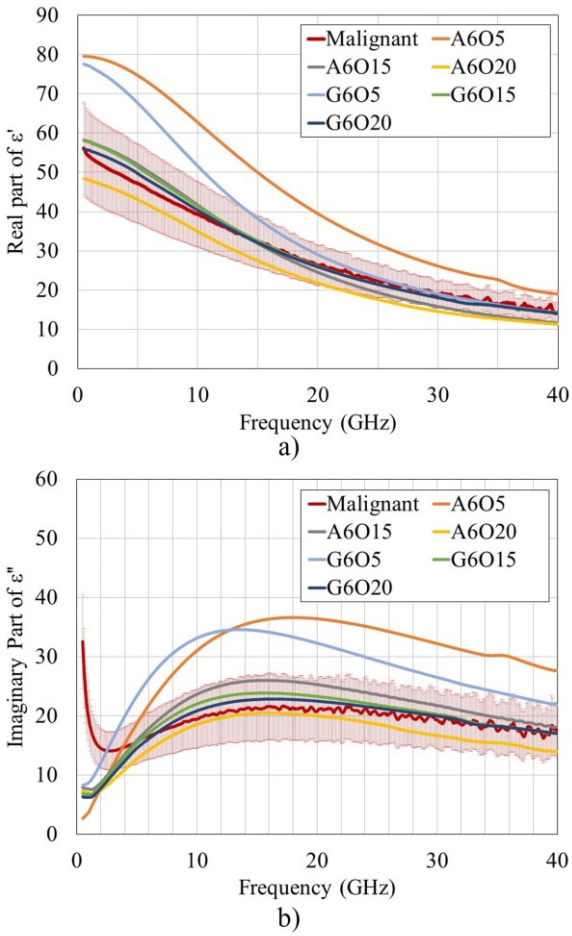

Figure 2. 8: Comparison between the average dielectric properties of the produced phantoms and those of human breast *ex-vivo* malignant tissues for

a) real and b) imaginary part of the dielectic permittivity. Shaded region indicates ± one standard deviation from the mean value for human breast *ex-vivo* malignant tissues **[70]**.

2.4.2. Mechanical properties of the produced phantoms

2.4.2.1. Design of the experimental campaign and derivation of Young's modulus of the bi-modal phantoms

The mechanical characteristics of the produced phantoms are described through their average Young's modulus. All the developed phantoms underwent mechanical measurements through the same experimental setup. For what concerns bi-modal phantoms ranging from #1 to #11, for each of the 7 experimental conditions, the average of the mechanical measurements conducted on 9 samples was calculated (3 samples from each of 3 replies per phantom type in different days). This procedure was carried out for each one of the 11 phantoms produced (3x3x7x11=693 samples in total).

Four samples for each of the phantoms from #12 to #17, instead, have been tested with the PL02TS05 condition only, as already mentioned.

Finally, twelve samples were prepared for testing for each of the two phantoms designed even for acoustic purposes (i.e., #2 and #18).

In Figure 2.9, an example of stress–strain curves for two different phantoms are shown, both measured under the experimental condition PL02TS1 (preload of 0.2 N and test speed of 1 mm/min). In particular, G3.3O66.6 (healthy low-density mimicking material) and G21.17O21 (tumor-like material) were chosen, since these represent the phantoms with the lowest and highest percentage of gelatin, respectively. From these curves, in addition to the obvious result that higher percentages of gelatin correspond to greater slopes of the curves, indicating greater stiffness of the samples, it is possible to note that in the 0%–5% strain region the behavior of both phantoms can be reasonably assumed as linear; in the 5–20/25% strain region, the behavior is quasi-linear, while for higher strain percentages the behavior follows different trends (it is even highly non-linear in the case of stiffer samples) until the phantom breaks. To quantitatively describe the mechanical behavior of all phantoms within the 0%–5% strain region, the Young's modulus, defined as the slope of the straight line interpolating the corresponding first tract of the experimental stress-strain curve, has been computed. It's worth noticing the choice to calculate only the Young's modulus of the phantoms at 5% strain only, because, on top of the approximate linearity of the material response, which ease the calculation, this threshold allowed to compare the results with those obtained by [21], in which the authors produced similar materials. As shown in Figure 2.9, as the percentage of strain increases, the response of the phantoms (Figure 2.9 shows the two limiting cases, at highest and lowest percentages of gelatin) tends to assume a non-linear behavior. In addition, low percentages of strain

are widely used in the literature to mechanically characterize biological samples in order to remain in the region of linearity of both biological *ex-vivo* and phantom samples. Indeed, in [72] the mechanical characterization of *ex-vivo* biological samples was proposed and the Young's modulus was calculated under the conditions of 5% and 20% 'pre-strain' to show that, as the initial compression level increases (in terms of 'displacement'), the values of the mechanical properties (including contrast) increase. In addition, the stress–strain characteristics of healthy tissues were shown to have a constant slope up to about 30% of strain (for tumor tissues, the linear behavior is kept over a shorter range, i.e. about 10% strain). In another example of characterization of *ex-vivo* samples [94], the decision not to consider the curve above 15% strain is clearly justified because of the non-linearity (and of damage to samples above this threshold) of tumor tissues.

On the other hand, there also seems to be a sensible limit on the stress level at which the Young's modulus should be calculated: [98] mentions the concept of 'light touch' (stress < 0.2–0.4 kPa), which is an optimal compression threshold in order to obtain clearer and more accurate US elastographic images. In the same paper, it is mentioned that tests are performed up to 50% strain on healthy specimens, but for tumors, due to their non-linear behavior, they stop at 30%. In other works, compression/indentation tests are carried out with very small displacements (0.5 mm maximum), but the size of the specimens is not specified, so it is not possible to determine the level of strain at which the Young's modulus is calculated [103], [104].

In [12], PVAL phantom characterization is carried out and Young's modulus is calculated at 15% and 30% strain as linear material behaviors are obtained up to this value. In addition, reference guidelines on how to perform ultrasound elastography [105] speak about values for tissue strain percentages among 0.1% and 2% for strain elastography in clinical *in-vivo* settings.

Furthermore, [106] shows that the tissues stiffness in elastographic images achieved in an *in-vivo* scenario is lower than the sample stiffness in an *ex-vivo* scenario.

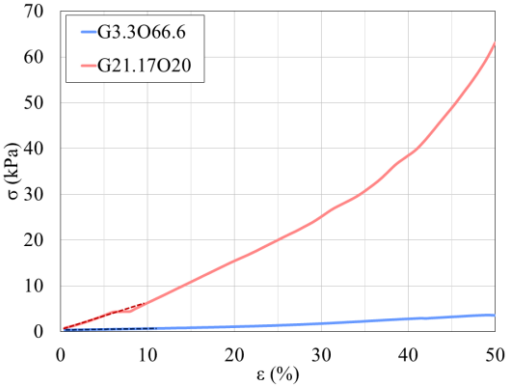

Figure 2. 9: Stress–strain curves for two phantoms (G21.17O20 and G3.3O66.6) measured with 0.2 N of preload and 1 mm/min of test speed.

Dashed lines indicate linear interpolation for the considered 0%–5% strain region.

2.4.2.2. Investigation of the impact of preload on mechanical properties

At first, the impact of preload on the mechanical behavior of the considered phantoms (from #1 to #11) has been evaluated. In particular, measurements have been performed to compute the mechanical properties of all the solidified mixtures at a test speed of 1 mm/min with preloads of 0.1 N, 0.2 N, and 0.4 N (experimental conditions PL01TS1, PL02TS1 and PL04TS1 in Table 2.3). The results are shown in Table 2.6 for all phantoms at 5% of strain. In addition, in Figure 2.10, the Young's modulus values at 5% of strain for phantoms mimicking low-density (gelatin percentage = 3.3% and 4.9%) and malignant tissues (gelatin percentage = 8%, 16% and 21.17%) are shown. From this figure, the increasing impact of the preload on the mechanical properties of phantoms with higher gelatin percentages can be noticed, in agreement with the literature [21], [72].

Table 2. 6: Young's moduli (kPa) of the produced phantoms for three different preloads (0.1 N, 0.2 N and 0.4 N) at a fixed test speed of 1 mm/min @ 5% of strain.

	Low-density		**Medium-density**		
	G3.3O66.6	**G4.9O66.6**	**G5O50**	**G7.35O50**	**G9.55O50**
PL01TS1	4.51±0.15	7.45±2.80	6.46±1.31	12.08±3.33	15.28±5.22
PL02TS1	3.86±1.24	9.61±4.53	5.73±1.99	6.34±0.93	19.57±1.11
PL04TS1	5.36±2.08	9.57±4.08	5.26±0.67	11.21±3.40	-
	High-density			**Malignant**	
	G6.6O33.3	**G9.8O33.3**	**G12.74O33.3**	**G8O20**	**G16O20**	**G21.17O20**
PL01TS1	8.46±2.17	14.83±8.46	27.51±4.00	10.35±3.36	17.84±10.81	11.44±5.46
PL02TS1	8.56±2.45	12.58±1.53	24.10±0.05	12.77±4.03	29.49±16.53	36.06±15.16
PL04TS1	9.85±3.02	15.56±3.58	-	12.51±0.91	28.51±10.26	52.46±17.57

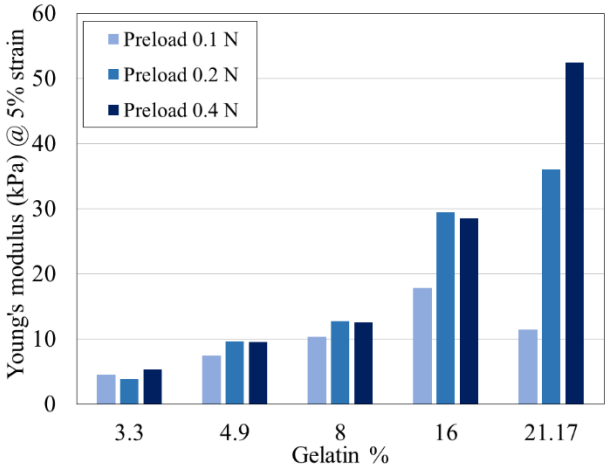

Figure 2. 10: Comparison between the Young's modulus at 5% of strain of phantoms mimicking low-density (gelatin percentage = 3.3%, 4.9%) and malignant human breast tissues (gelatin percentage = 8%, 16%, 21.17%) for three different preloads using a test speed of 1 mm/min.

2.4.2.3. Investigation of the impact of test speed on mechanical properties

The second investigated parameter, on the same group of phantoms, was the test speed. In particular, low- and high-test speeds were considered to assess the impact of this parameter on phantoms mechanical characteristics in a broad range of test speeds. Specifically, compression tests of all manufactured phantoms at a fixed preload (i.e. 0.2 N) have been performed with varying test speeds from 0.5 mm/min (quasi-static compression) to 2 mm/min, as well as compression tests of two phantoms mimicking low-density healthy and malignant tissues at a fixed preload (i.e. 0 N) with test speeds of 60 mm/min and 80 mm/min. These specific values of the test speed have been chosen to reproduce a similar scenario as in clinical ultrasound investigations (i.e., to resemble the compression of the probe against breast tissues in ultrasound elastography). For this last set of measurements, G4.9O66.6 and G21.17O20 were considered, as these represent the lower and upper category of mimicked tissue, in terms of density. In Table 2.7, the values of Young's moduli at 5% of strain under the experimental conditions of 0.2 N preload and test speeds of 0.5 mm/min, 1 mm/min and 2 mm/min (i.e. PL02TS05, PL02TS1 and PL02TS2) are shown. In addition, in Figure 2.11, a subset of the results presented in Table 2.7 is illustrated (i.e. the Young's modulus values at 5% of strain for phantoms mimicking low-density and malignant tissues). Similarly, in Figure 2.12, the Young's modulus values for G4.9O66.6 and for G21.17O20, under the experimental condition of 0 N preload and test speeds 60 mm/min and 80 mm/min, are shown at 5% of strain. Although comparing the values of Young's modulus for the same material at very different compression rates these are quite different (e.g. for G21.17O20, the Young's modulus at low compression rates—from 0.5 mm/min to 2 mm/min—is around 35 kPa, while for higher

speeds—60 mm/min and 80 mm/min—it is around 9 kPa), it should be noted that the preloads used for the two sets of measurements are different (for Figure 2.11, the preload was 0.2 N and for Figure 2.12 it was 0 N due to measurement setup issues), and as shown previously in Figure 2.10 this justifies the different values of Young's modulus obtained. Therefore, taking this into account, the obtained results show that the compression rate has no significant impact on the Young's modulus values of the phantoms. The only three cases where a more visible variation is observed are G7.35O50, G9.55O50 and G16O20. However, it is not possible to derive a correlation between them; therefore, they may be variations due to measurement errors. As an example, some troubles occurred with the control of the experimental setup using high speeds: for what concerns the use of these materials, it is critical to manage the adherence between the compression punch and the sample under test, as its shape and dimension are difficult to geometrically standardize and strongly related to conditions like temperature and composition. Only the mechanical behavior of the G16O20 for the test speed of 2 mm/min would deserve further investigations, since its mechanical properties seem to be related to the applied test speed. From these overall results, it is possible to conclude that the mechanical behavior does not appear to be rate dependent.

Table 2. 7: Young's moduli (kPa) of the produced phantoms for three different test speeds (0.5 mm/min, 1 mm/min and 2 mm/min) at a fixed preload of 0.2 N @ 5% of strain.

		Low density		**Medium density**		
	G3.3O66.6	**G4.9O66.6**		**G5O50**	**G7.35O50**	**G9.55O50**
PL02TS05	3.66±0.06	12.43±0.91		6.28±0.82	13.89±2.65	13.95±1.07
PL02TS1	4.64±2.43	8.87±3.17		4.82±1.06	8.60±3.69	24.17±1.59
PL02TS2	3.86±1.24	9.61±4.53		5.73±1.99	6.34±0.93	19.57±1.11
		High density			**Malignant**	
	G6.6O33.3	**G9.8O33.3**	**G12.74O33.3**	**G8O20**	**G16O20**	**G21.17O20**
PL02TS05	8.37±0.67	13.95±2.24	24.10±0.05	7.43±2.80	20.59±6.25	35.26±16.98
PL02TS1	8.00±2.27	12.84±1.76	24.04±7.79	8.75±2.79	47.03±20.53	32.46±27.34
PL02TS2	8.56±2.45	12.58±1.53	24.10±0.05	12.77±4.03	29.49±16.53	36.06±15.16

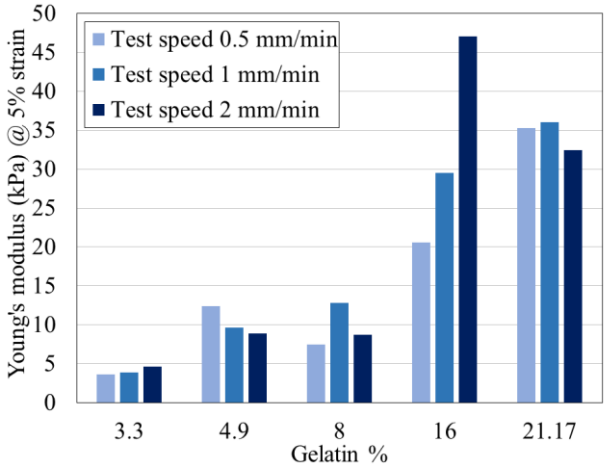

Figure 2. 11: Comparison between the Young's modulus at 5% strain of phantoms mimicking low-density (gelatin percentage 3.3% and 4.9%) and malignant human breast tissues (gelatin percentage 8%, 16% and 21.17%) for three different test speeds at a preload of 0.2 N.

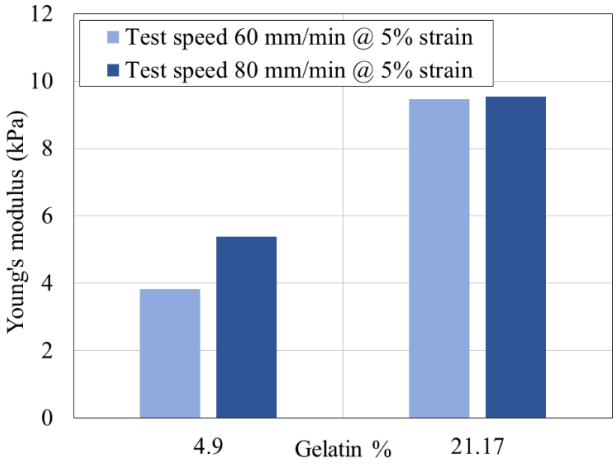

Figure 2. 12: Comparison between the Young's modulus at 5% strain of phantoms mimicking low-density (gelatin percentage = 4.9%) and malignant human breast tissues (gelatin percentage = 21.17%) for two high test speeds (60 mm/min and 80 mm/min) at a preload of 0 N.

2.4.2.4. Investigation on the influence of the solidifying agent on the mechanical properties

According to [21], a preload of 0.2 N and a test speed of 0.5 mm/min were chosen for mechanical measurements on the phantoms ranging from #12 to #17 to assess whether either the kind of solidifying agent (i.e., gelatin or agar) or the fat content percentage within the mixture could influence the mechanical properties of the tested materials. The stress-strain curves of each phantom were measured under these experimental conditions up to the sample breakage. In Figure 2.13, the comparison between the average

Young's modulus of all the produced mixtures, both with agar and with gelatin, are shown as a function of the percentage of oil at 5 % of strain. In [21], mixtures involving similar components (i.e., agar and gelatin) at the same strain level and under the same experimental conditions were characterized, and values higher than 80 kPa were achieved in both cases. As can be seen from this figure, phantoms using agar as solidifying agent are stiffer than those based on gelatin, even if their Young's modulus are still lower than those reported in the literature [21]. In addition, differently from gelatin-based phantoms, the increase of oil percentage (which is necessary to match the dielectric properties to those of *ex-vivo* tissues), as shown in Figure 2.13 in agar-based mixtures is responsible of a decrease of the phantom stiffness. At the current stage of this project, further research is required to approach the reference values from both a dielectric and a mechanical point of view for what concerns phantoms ranging from #12 to #17. However, these specific phantoms have been primarily developed to assess the influence of the type of solidifying agent combined with the varying oil percentage content.

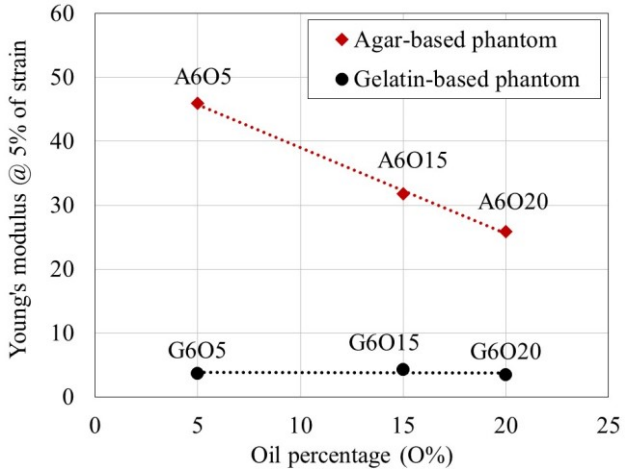

Figure 2. 13: Comparison between the average Young's moduli of the produced phantoms based on agar and gelatin, as a function of the oil volume percentage at 5% of strain. For all phantoms, the average Young's modulus measured on the four samples derived from each mixture is shown.

2.4.2.5. Mechanical contrast between healthy- and neoplastic-tissue-like phantoms

Mechanical contrast is represented by the ratio of the Young's modulus of two materials, it is a dimensionless quantity and expresses the relative difference in stiffness between two materials. In the literature, the mechanical behavior of *in-vivo* and *ex-vivo* samples is sometimes provided in terms of contrast (i.e. the ratio between the elastic modulus of two different materials) between healthy and tumor tissues [72], [94], [107], [108], [109]. This information can improve the sensitivity and specificity (related to the percentage of false positives and false negatives) of the

imaging technique, being sometimes even more important than the knowledge of the absolute value of the Young's modulus of each phantom or tissue. For this reason, among the phantoms from #1 to #11, the mechanical contrast has been computed between the tumor-like tissue-mimicking phantoms and two different categories of healthy-like phantoms (i.e. fat- and fibroglandular-like tissue-mimicking materials), for all the investigated experimental conditions. In the following tables, the mechanical contrasts at 5% of strain are shown. In particular, in Table 2.8, the mechanical contrast between the phantoms mimicking malignant tissues and the softest phantom (phantom #1, G3.3O66.6) is shown. In Table 2.9, the mechanical contrast between the phantoms mimicking malignant tissues and the one mimicking high-density tissues (G6.6O33.3) is shown. These tables show that the range of mechanical contrasts covered by our phantoms is wide. However, while the contrasts are too low when considering the ratio of G8O20 to G3.3O66.6, and indeed are not comparable with any value reported in the literature, they show higher values when considering tumor-like mixtures with higher percentages of gelatin (i.e. G16O20 and G21.17O20) and are more in line with those reported in other papers. In particular, under PL04TS1 and PL02TS05 experimental conditions, the G16O20/G3.3O66.6 ratio seems directly comparable with the mechanical contrast reported in [72]. In addition, when considering the mechanical contrasts between tumor- and healthy-tissue-like phantoms with major fibrous and glandular components, the obtained values are in line with those shown in [94]. In particular, the ratio G8O20/G6.6O33.3 is able to mimic the mechanical contrast between the papilloma and the fibro-glandular tissue under almost all experimental conditions. On top of that, PL02TS1 condition allows to obtain a mechanical contrast in line with that shown in [94] for invasive ductal carcinoma (IDC) and glandular tissue when the mixtures G16O20 and G6.6O33.3 are considered. However, it should be noted that for all the values reported in the literature, obtained from the characterization of *ex-vivo* samples, the experimental conditions are not specified, and only in some cases the level of strain is reported. Therefore, the previous considerations referring to comparisons with results in the literature are mostly qualitative, as an actual quantitative comparison with such values is not possible.

Table 2. 8: Mechanical contrasts between malignant- and low-density-tissue-like phantoms at a 5% strain.

	G8O20/G3.3O66.6	**G16O20/G3.3O66.6**	**G21.17O20/G3.3O66.6**
PL04TS2	2.35	7.59	7.35
PL02TS2	1.88	10.12	6.98
PL02TS1	3.30	7.62	9.32
PL04TS1	2.33	5.31	9.77

PL02TS05	2.02	5.61	9.61
PL01TS1	2.33	3.87	2.53
PL01TS05	2.15	2.74	4.18

Table 2. 9: Mechanical contrasts between malignant- and high-density-tissue-like phantoms at a 5% strain.

	G8O20/G6.6O33.3	**G16O20/G6.6O33.3**	**G21.17O20/G6.6O33.3**
PL04TS2	1.22	3.94	3.81
PL02TS2	1.09	5.87	4.05
PL02TS1	1.49	3.44	4.21
PL04TS1	1.27	2.89	5.32
PL02TS05	0.88	2.45	4.21
PL01TS1	1.24	2.06	1.35
PL01TS05	1.26	1.61	2.45

2.4.3. Acoustic properties of the produced phantoms

After assessing the dielectric and mechanical properties of the proposed TMMs, their acoustic properties were measured. As already mentioned, only two phantoms were found suitable to represent the acoustic properties of the human healthy and diseased breast tissues. Thus, at least 10 samples for each of the two considered phantoms (i.e., #2 and #18) underwent acoustic characterization.

In practical terms, at first, the speed of sound and the attenuation coefficient at 7 MHz have been estimated, close to the central frequency of many previous studies in the context of phantoms characterization using ultrasound [14], [15], [74], [75]. The result of this analysis is provided in Table 2.10. Then, a further search on the trend of attenuation along with frequency (in the range of 5-10 MHz) was conducted. In Figure 2.14, the results of this study are provided: as expected, the attenuation in the produced TMMs has been found to have an almost linear increase with the frequency. Thus, the two TMMs were good in reproducing the properties of the corresponding breast tissues also from an acoustic point of view.

Also the speed of sound has been analyzed by varying the frequency between 5 and 10 MHz with a 1 MHz step size. As expected, even from existing results in the literature [78], no significant influence of the frequency has been observed on the measured speeds.

Table 2. 10: Acoustic properties of the tested phantoms. Reference values can be found in **[14]**.

		Material			
		G4.9O66.6 Fat TMM		A6K0.6O20 Tumor TMM	
		Measured	Reference	Measured	Reference
Acoustic properties	c_{ph} (m/s)	1481 ± 4.68	1479 ± 32	1508 ± 26.7	1550 ± 35
	α (dB*cm^{-1}*MHz^{-1}) @ 7 MHz	0.7 ± 0.23	0.6 ± 0.1	0.99 ± 0.38	1.0 ± 0.2

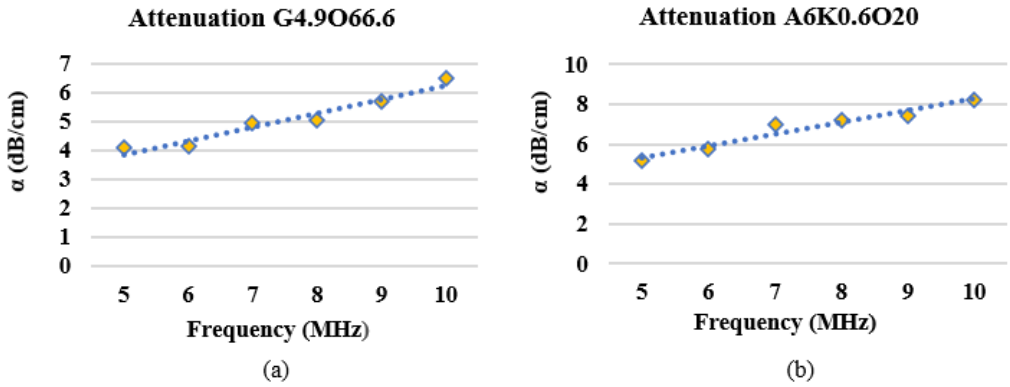

Figure 2. 14: Attenuation as a function of the frequency of the tested TMMs.

2.5. Investigation of the time-stability of the produced phantoms' properties

One of the most important aspects for a long-lasting mixture that mimics breast tissues is the stability of its dielectric and mechanical properties, in order to ensure reliable testing of the multi-modal imaging system prototype over time. Although a study on the preservation of dielectric properties has already been conducted [110], the preservation of mechanical properties, to date, has not been explored in the scientific literature.

In this study, two phantoms were considered: phantom #1 - G3.3O66.6 (as a candidate for representing the healthy low-density breast tissues) – and phantom #18 - A6K0.6O20 (as a tumor-like tissue-mimicking phantom) -, and the preservation of both the dielectric and mechanical properties of these phantoms was studied. In a previous study [110] the authors have shown that the storage in sunflower seed oil is the best method for preserving the dielectric properties of gelatin-based phantoms compared to deionized water and air. Preservation in deionized water tends to yield consistently higher values over time due to the mixture absorption of water. Conversely, the mixture left in the air shows a constant decrease in dielectric permittivity values due to water evaporation from the mixture. Preservation in sunflower

seed oil is the best method as it keeps the dielectric properties of the mixture relatively stable over time. For this reason, sunflower seed oil was also chosen as the preservation method in this study.

The two phantoms were produced using the recipes outlined in Table 2.2 and the procedure described previously. They were completely immersed in oil and stored in a refrigerator inside an airtight container. Both their dielectric and mechanical properties have been investigated over ten days after the production. The dielectric characterization has been carried out following the procedure explained previously in this Chapter, in the same frequency range of 0.5-40 GHz. Three measurements have been performed within the same sample every day. As shown in Figure 2.15 the measurements of the real part of the dielectric properties of the G3.3O66.6 phantom show good stability over time, with minimal variations compared to the reference value. Similarly, for the A6K0.6O20 phantom (Figure 2.16), the real part of the dielectric properties remains stable over time. Similar considerations can be done for the reported imaginary part of the dielectric properties, where both phantoms demonstrate good stability over time, with no significant variations. This proves that sunflower seed oil is an effective method for preserving dielectric properties, as it ensures their stability over time.

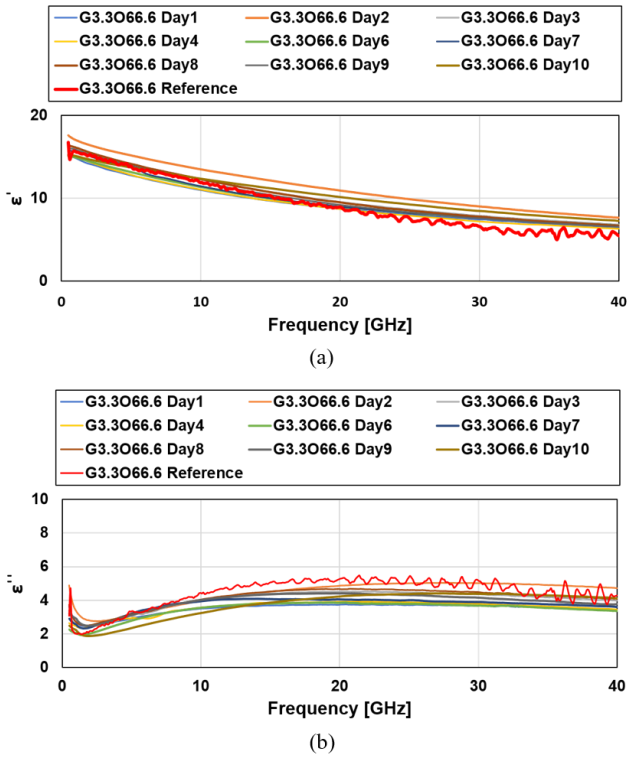

Figure 2. 15: Dielectric properties (real (a) and imaginary (b) part of dielectric permittivity) of phantom G3.3O66.6 stored in sunflower seed oil over ten days.

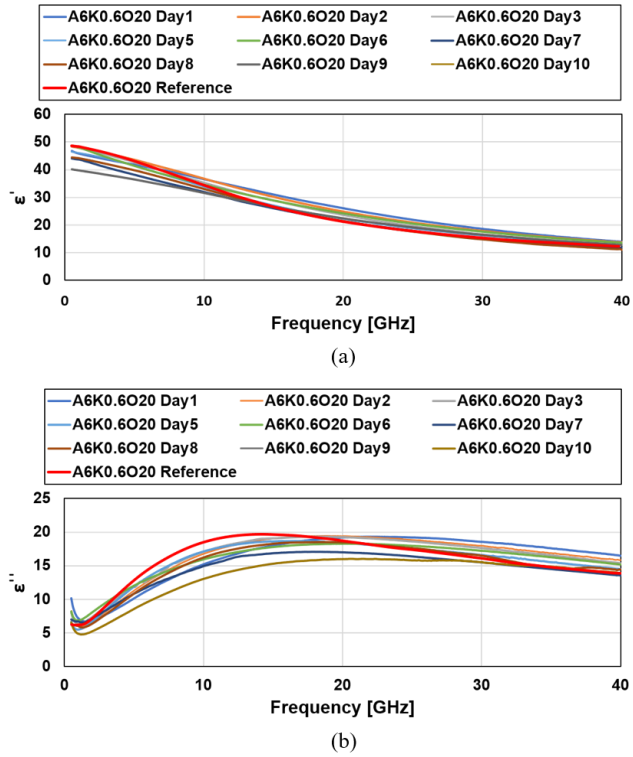

Figure 2. 16: Dielectric properties (real (a) and imaginary (b) part of dielectric permittivity) of phantom A6K0.6O20 stored in sunflower seed oil over ten days.

The mechanical properties have been studied as well, following the same experimental conditions described in the previous sections of this Chapter. The preload was set at 0.2 N and the test speed at 0.5 mm/min (PL02TS05). The mechanical properties have been calculated on three samples per day. Here, for consistency with the previous results, the Young's modulus at 5% of the strain is showed (Figure 2.17). It is worth noticing that in both cases, the values of the Young's modulus are very close to the reference value (red line – corresponding to the measurement conducted at the first day) and they remain approximately constant over time.

The mechanical contrast was calculated as the ratio of the Young's modulus of the two materials, which expresses the relative difference in stiffness between two materials. By calculating the contrast at 5% strain between the A6K0.6O20 phantom, and the G3.3O66 phantom, it was found to be around 8, confirming the phantom's ability to mimic the mechanical properties of breast tissues.

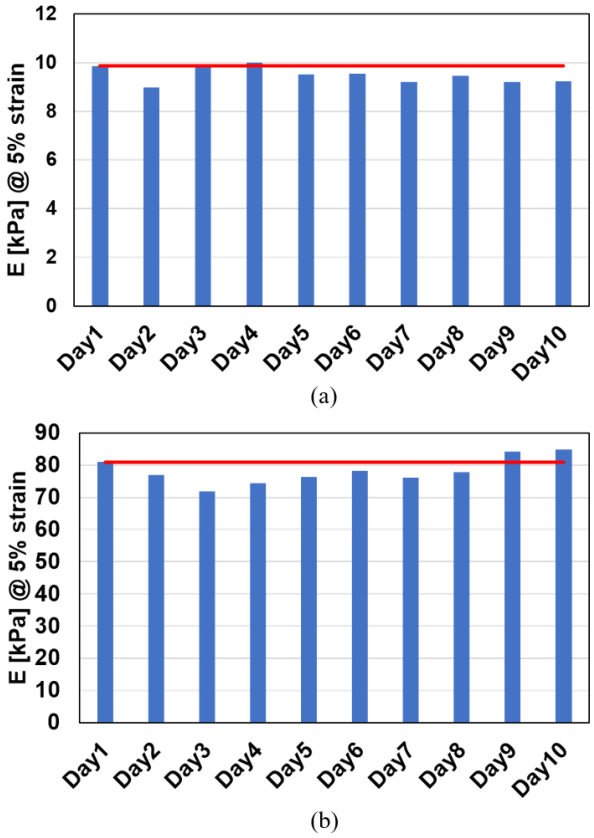

Figure 2. 17: Comparison between the Young's modulus of phantoms G3.3O66.6 (a) and A6K0.6O20 (b) stored in sunflower seed oil over ten days. The red lines represent the reference value of the Young's modulus of the tested phantoms in Day1 (i.e., 9.87 kPa and 80.8 kPa for the healthy and the tumor phantom, respectively).

2.6. Development of heterogeneous multi-layer breast phantoms

As a final step, different realistic heterogeneous phantoms have been produced, to prove the feasibility of incorporating multiple materials into hand-made 3D models. Thus, a sophisticated approach to create breast phantoms with multiple layers is proposed, maintaining the actual tissue properties and breast shape.

The first attempt for the realization of such phantoms implied a healthy fat background (G3.3O66.6) with a tumor-like inclusion (G21.17O20). The procedure to obtain the mixtures was the same described in [8] and adopted over the projects regarding the present thesis. The model has been designed as conformal and the tumor-like inclusion was thought to be oval, with an approximately 2 cm length. To obtain such a model the mixtures were prepared individually. Particularly, the oval inclusion was prepared and allowed to solidify at first, using a dedicated mold. Thus, it was placed within

a cup-shaped mold where the background phantom mixture was poured at a temperature of 45 °C, while keeping the inclusion through a home-made holder. The complete phantom was then placed in the freezer for 30 minutes. A photo of the resulting phantom is presented in Figure 2.18(a), and a cross section of it in which the inclusion is visible is shown in Figure 2.18 (b). The food dye added to the mixtures is only meant to make the inclusion visible, without altering the properties of the phantom. This has been demonstrated by producing and characterizing samples of different colors obtained from the same mixtures (Figure 2.19 (a)). The achieved dielectric properties showed that the addition of the food dye to the G3.3O66.6 mixture did not alter significantly its dielectric properties (Figure 2.19 (b) and (c)).

The phantom was then sectioned in order to separate the background from the inclusion, and four cylindrical samples per phantom were derived, all with 28 mm diameter and 10 mm height. As an example, the samples were characterized under the experimental conditions denoted by PL02TS1 and PL04TS1, i.e. preload = 0.2 N and 0.4 N and test speed = 1 mm/min. The average mechanical properties, in terms of Young's modulus calculated at 5% of the strain, measured on these specimens were found to be 3.16 and 4.02 kPa for the fat-like samples and 34.02 and 49.48 kPa for the tumor-like samples in PL02TS1 and PL04TS1 conditions respectively. From these results it is possible to appreciate the good agreement with Tables 2.6 and 2.7, and thus the repeatability of the mechanical measurements even when larger quantities of the ingredients are used to generate greater phantoms.

Figure 2. 18: Photo of the complete phantom with an inclusion.

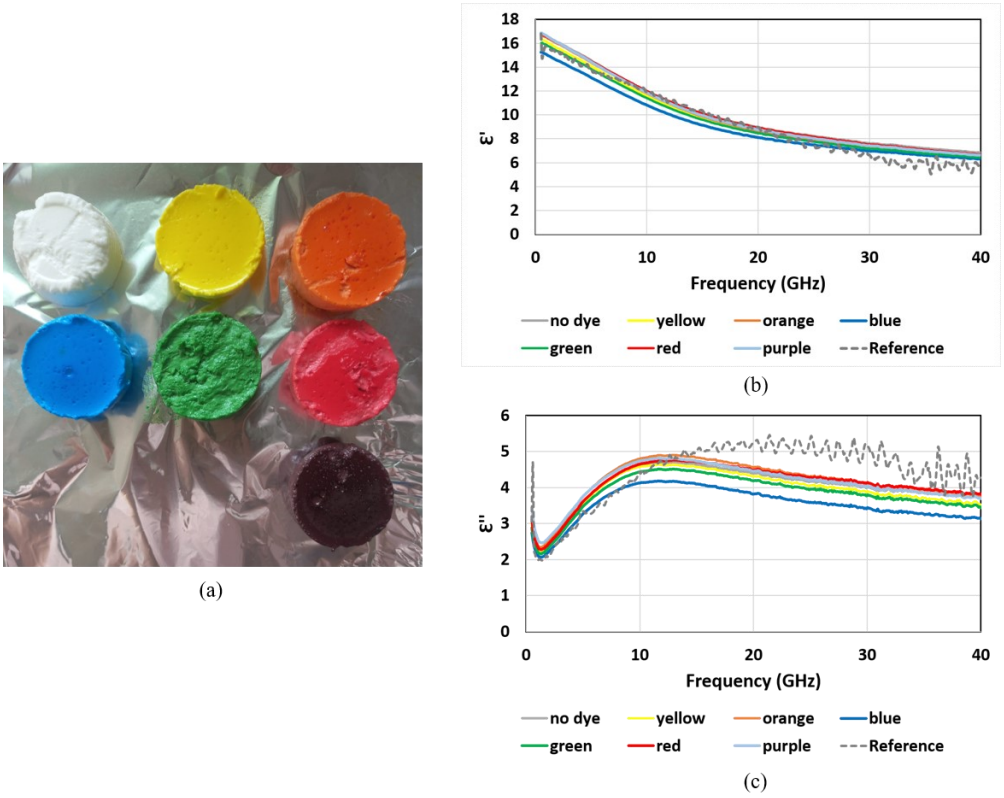

Figure 2. 19: G3.3O66.6 samples colored according to different food dye (a). Dielectric properties or the different samples (real (b) and imaginary (c) part of dielectric permittivity).

Another activity, instead, has been focusing on the design and characterization of various materials mimicking the properties of the breast tissues and the development of different complex breast phantoms with multiple layers of material for a possible use in microwave-based breast tumor detection systems [111], [112]. Various recipes have been considered to construct the phantoms in this framework, since the human breast consists of various layers (i.e., glandular, adipose, connective tissues) with different dielectric properties. In particular, multi-layer phantoms with either planar of hemispherical configuration have been developed, involving both healthy- (i.e., G5O50 and G66.6O33.3) and tumor-like (i.e., G8O20) tissue-mimicking materials. The planar configuration has been realized at first to demonstrate the feasibility of creating such phantoms through the proposed process. After the individual mixtures were prepared, the complete phantoms have been obtained following the approach described in [8] and above. In phantoms with tumor inclusion between the two layers, before pouring the second layer, a shape of the desired size was removed from the solid, cold, layer and the mixture with the desired dielectric properties was poured into it. In this case, before pouring the top layer, the entire base (first layer + inclusion) was placed in the freezer for an additional 10 minutes. After this

time had elapsed, the mixture corresponding to the second layer (again at a temperature of 45 °C) was poured over the solid and cold first phantom layer. The resulting phantom was again covered with film and allowed to solidify at room temperature for about 2 hours.

In Figure 2.20 (a)-(d) several photos of multi-layer phantoms are shown, in both planar and hemispherical configurations, with and without the inclusion, respectively. In particular, in Figure 2.20 (a) and (b), the bottom layer is composed by G5O50, the inclusion is G8O20, and the top layer is composed by water and gelatin. In Figure 2.20 (c) and (d), the bottom layer is composed by G6.6O33.3, and the top layer is composed by G8O20.

As can be seen, this procedure enabled the preparation of layered phantoms to be used, for example, in imaging tests in realistic scenarios.

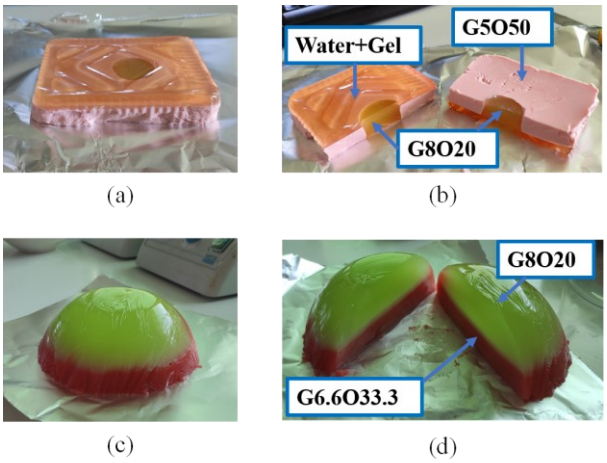

Figure 2. 20: Photo of multi-layer phantom in linear, (a)-(b), and conformal, (c)-(d), configuration. In (a) and (b), the bottom layer is G5O50, mimicking healthy tissue. The top layer is water and gelatin, while the inclusion mimicking neoplastic tissue is composed by G8O20. In (c) and (d), the bottom layer is composed by G6.6O33.3, mimicking healthy tissue, while the top layer is composed by G8O20, mimicking neoplastic one.

Moreover, to assess whether the proposed procedure affected the dielectric properties of the phantom, the phantom was sliced and the dielectric properties of individual parts were measured after it had completely solidified and reached room temperature, around 20 °C. These measurements were then compared with those presented in [8]. As an example, in Figure 2.21 (a) and (b), a comparison is presented between the dielectric properties of the G6.6O33.3 phantom produced in this study and those of the same phantom detailed in [8], in which no cooling stages were employed during production, for both the real and imaginary parts of dielectric permittivity. These graphs demonstrate that the multi-step procedure for preparing heterogeneous phantoms does not alter the dielectric properties of the mixtures, despite the presence of ripples at high frequencies in the reference

curve, which limits the quantification of the similarity between the two phantoms.

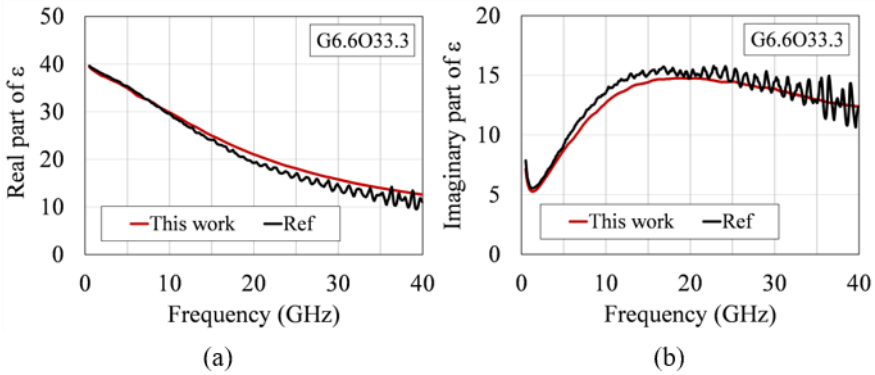

Figure 2. 21: Comparison of dielectric properties between the G6.6O33.3 mixture produced in this work, after the entire phantom preparation process, and the same mixture presented in **[8]** for (a) real, and (b) imaginary parts of dielectric permittivity.

Finally, a more realistic multi-layer model has been developed. For this reason, container molds were designed using a low-cost 3D printer (BQ model Prusa i3 Hephestos) and standard PLA filament. Three molds, depicted in Figure 2.22 (a), fit seamlessly within each other, enabling the creation of breast phantoms with two layers (skin and mammary gland) or three layers (skin, fat, and mammary gland). The previously detailed low-, medium-, and high-density mixtures (i.e., G33.3O66.6, G5O50 and G66.6O33.3, respectively) serve to emulate fat, skin, and mammary gland, respectively.

The process for creating both two-layer and three-layer breast models is as follows: initially, the material simulating the outer layer of the breast skin is carefully introduced between the two largest molds. Cling film is applied before this step to facilitate the removal of the inner mold and preserve the integrity of the material layer. The skin-mimicking material is introduced at an initial temperature of 45 °C. After filling the space corresponding to the skin layer, the model is refrigerated for 10 hours to allow controlled solidification.

Following this interval, the innermost mold is removed, revealing the skin-mimicking material (Figure 2.22 (c)). It is then allowed to temper, enabling the introduction of the subsequent compound into the prepared gap. Crafted at 45 °C, the second compound undergoes gradual cooling to approximately 28 °C, aligning with the temperature of the preceding layer. This process ensures a seamless integration with the previously deposited material, maintaining a precise boundary. In the case of the two-layer phantom, this second compound represents mammary gland uniformly occupying the entire remaining space (Figure 2.22 (d)). For the three-layer phantom, the second compound represents fatty tissue, filling the space between the first layer and the smallest mold, positioned for this purpose

within the developing phantom. After depositing the second material, the phantom is returned to refrigeration for an additional 10 hours. To complete the three-layer breast phantom, the smallest mold is removed, and the third material (mammary gland) is deposited using the same procedure as employed for the previous layers, resulting in the configuration depicted in Figure 2.22 (e).

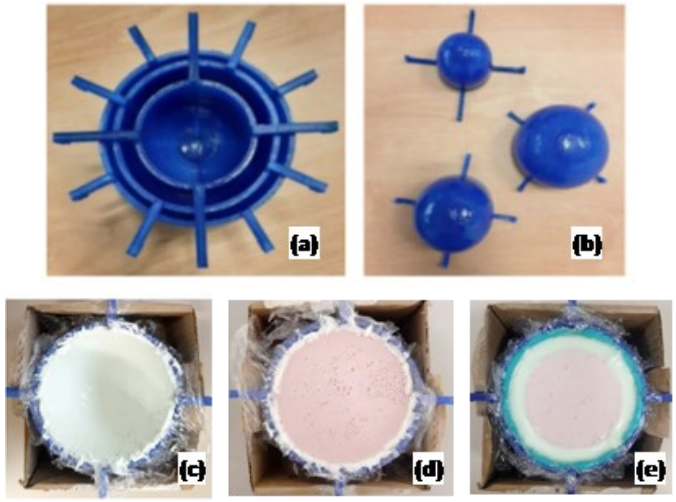

Figure 2. 22: (a) Molds designed for the different layers. (b) Molds placed separately upside down. (c) First layer solidified. (d) Liquid second layer poured onto the first layer for the two-layer phantom. (e) Liquid third layer poured onto the second layer for the three-layer phantom.

As illustrated in Figure 2.23 (a), the two-layer breast phantom is presented using an inert dye to differentiate materials based on their dielectric properties. In this configuration, as a first attemp, a 5 mm-thick layer emulates the skin (indicated in white), while the remainder of the phantom represents mammary gland tissue, distinguished by its pink coloration. Figure 2.23 (b) provides a longitudinal cross-section of the two-layer breast phantom, emphasizing the precise separation between the different material layers.

In Figure 2.23 (c), the three-layer breast phantom is presented. In this case, the skin layer, 5 mm in thickness, is visually denoted by green dye, while the fat layer, having 10 mm depth, is represented in its natural color. The remaining volume of the phantom has been filled with mammary gland tissue-like material, characterized by its pink hue. Figure 2.23 (d) offers a cross-sectional view of the phantom, clearly revealing the stratified layers and their well-defined interfaces and bonds. It's worth noting that in Figure 2.23 (a) and (c), some irregularities within the mammary gland layer can be observed, attributed to the insertion and removal of tumor models during various measurement sessions aimed at optimizing the phantom's utility. This drawback should be considered when dealing with this kind of tissue-mimicking mixtures. To address this limitation, other materials may be

investigated (i.e., semi-solid, more mechanically resistant materials) for the production of these multi-layers breast conformal phantoms.

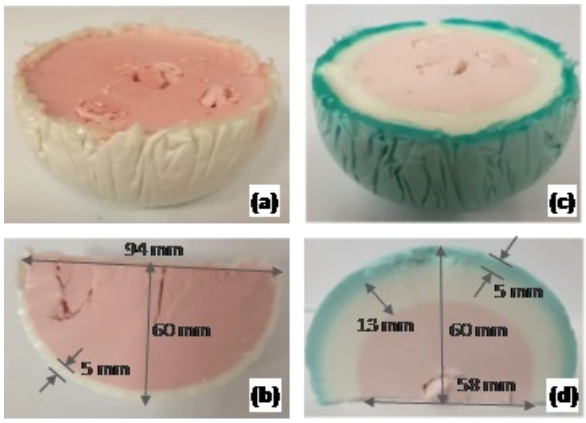

Figure 2. 23: Two-layer phantom: (a) upright demolded breast phantom, (b) cross-section of the breast phantom. Three-layer model: (c) demolded breast phantom, viewed from above; (d) cross-section of the breast phantom. Key layer dimensions are depicted too.

2.7. Discussion and conclusion

The previous sections have shown the results of the dielectric, mechanical and acoustic characterization of a series of phantoms based on deionized water, sunflower oil, dishwashing liquid, gelatin or agar and waste-oil hardener. The considered recipes to obtain the proposed materials were derived from those previously proposed in [8] and the percentage of gelatin was increased, at first, to mimic the mechanical properties of breast tissues, always paying close attention to the dielectric properties of the mixtures. Specifically, the dielectric properties were measured up to 14 GHz and fitted with the Cole–Cole model in order to predict their properties up to 50 GHz. The dielectric permittivity curves were compared to those of human *ex-vivo* breast tissues [70] showing a good agreement, even when the percentage of gelatin was increased to mimic the mechanical properties of healthy and neoplastic tissues. However, if on one hand the methods to obtain reliable dielectric measurements are now consolidated, on the other hand there are still uncertainties for the mechanical characterization. Analyzing the literature related to the mechanical characterization of biological samples, the absence of univocal measurement guidelines is clear, with the consequent significant variability in the results produced. In particular, among the most common techniques for the mechanical characterization of materials (i.e. unconfined, confined and indentation compression), it seems that the most popular method used for this kind of semi-solid samples is the unconfined compression, which was thus employed also in this work. Here, an analysis on the impact of the two most critical parameters in this type of measurements, i.e. the preload and test speed, has been conducted, by

performing mechanical measurements under different experimental conditions (preload = 0.1 N, 0.2 N, 0.4 N; test speed = 0.5 mm/min, 1 mm/min, 2 mm/ min). The analysis focused on the strain range 0%–5%, as this is one of the most widely used values in the literature (when explicitly indicated), and it also represents a region where the stress–strain curve for this type of phantoms shows a linear trend, making it possible to determine the corresponding Young's modulus value. In particular, it has been shown that the preload has a major impact when considering phantoms with a high percentage of gelatin, while it has approximately no impact for phantoms mimicking soft tissues (i.e. with a low percentage of gelatin). This result is in line with the literature [21], [72], although the absolute values of the elastic modulus are different due to different measurement conditions (which are often unspecified). Regarding the test speed, the results show that the dependence of the mechanical properties of the produced phantoms on this parameter is not significant, both for slow compression speeds in the range from 0.5 mm/min to 2 mm/min and for high compression speeds, as 60 mm/min and 80 mm/min. A comparison between the Young's modulus of the phantoms of this thesis and those published in literature was possible only with [21], because this was the only work in which almost the same experimental setup, as well as some of the experimental conditions, were used. The comparison with [21] was also feasible due to the similarity of the materials involved in the phantoms. The results show that the mechanical properties of phantoms mimicking adipose tissues (G4.9O66.6) agree with [21] when the same experimental conditions are considered. On the other hand, the achieved Young's modulus of tumor-like tissue phantoms are lower than those proposed in [21], also when the G21.17O20 mixture is considered, demonstrating that a variation of the gelatin percentage only is not enough in this case, and that a modified mixture recipe would be necessary. For this reason, some new materials have been introduced modifying the amount and the kind of solidifying agent within the mixtures, specifically to mimic the mechanical properties of malignant breast tissues. The results of this activity show that, from a dielectric point of view, mixtures with higher oil percentages are able to mimic the dielectric properties of malignant breast tissues in all the investigated bandwidth, regardless of the employed solidifying agent (i.e., gelatin or agar); while, from a mechanical point of view, agar allows to produce stiffer phantoms than gelatin. However, the stiffness of the agar-based phantoms decreases as the oil percentage increases, making it necessary to minimize the amount of oil in the mixture in order to obtain Young's moduli values similar to those reported in the literature for malignant phantoms. Nevertheless, this would lead to phantoms no longer able to mimic the dielectric properties of human neoplastic tissues.

Within this project, the mechanical contrast between malignant and healthy tissues has been explored as well. In particular, the ratio between the Young's moduli of neoplastic- and healthy-tissue-like phantoms under all the considered experimental conditions has been estimated. The contrasts

between malignant- and adipose- tissue-like phantoms, as well as between malignant- and fibroglandular-tissue-like phantoms have been reported. Indeed, these two cases were selected because they both represent borderline cases and the two most interesting scenarios in a possible clinical setting (especially the contrast between malignant and fibro-glandular tissues). Despite the high dependence of mechanical properties from the experimental conditions, the results are in line with those reported in the literature, when both these ratios are considered [72], [94].

Moreover, a multi-modal characterization of two tissue-mimicking breast phantoms has been conducted within this research. A tumor phantom (A6K0.6O20) and a healthy fat one (G4.9O66.6) were produced and dielectrically, mechanically and acoustically tested. The phantoms recipes were originally supposed to involve the same solidifying agent (i.e., gelatin). However, in order to further increase the stiffness of the tumor TMM, gelatin was replaced with the agar powder. This substitution was possible as the type of the solidifying agent did not have a significant influence on the dielectric properties of the phantoms. This represents an advantage in using this kind of materials, as it is possible to tune their mechanical properties (i.e., the Young's modulus) controlling the dielectric ones. This work particularly focused on the acoustic characterization of phantoms as well. The two produced TMMs were found to be suitable for representing the corresponding real breast tissues from a multi-modal point of view. Next steps of this research may include the production and acoustic testing of a fibro-glandular tissue phantom. Moreover, it would also be useful to determine the ultrasound backscattering coefficient of the produced TMMs and to test the addition of new powders, like graphite or glass beads, to the recipes, to further tune the echogenicity and acoustic properties of the phantoms. In this framework, future analyses will investigate the properties of new TMMs and their performance in US B-mode, US elastography and mm-wave imaging. However, the multi-modal characterization carried out in this thesis demonstrated that a good compliance between the measured and expected properties can be obtained by employing such phantoms. Specifically, the average percentage difference between the developed materials against the healthy and diseased tissues of the human breast was found to be less than 20% for the dielectric characterization method and around 24% for the mechanical characterization method. The best performance was observed in the context of the acoustic characterization, where the average percentage difference between the reference and the measured properties was found to be less than 5%.

The durability in terms of preservation of the dielectric and mechanical properties of some of the produced phantoms has been evaluated as well, suggesting that, if properly stored in sunflower seed oil, this kind of mixtures ensures the stability of both the properties of interest. The preservation of the acoustic properties has not been tested yet, mostly because of practical issues related to the fact that the acoustic measurements are normally performed in water causing deterioration of the samples.

The last part of the study proved the possibility to construct multi-layer linear and hemispherical breast phantoms using tissue-mimicking handmade gelatin-based materials for microwave imaging. This achievement underscores the potential of these sophisticated phantoms in enhancing, training, or refining microwave imaging systems. The research aligns with current trends in radar-based microwave breast imaging systems.

Chapter 3

Investigation on a radar approach for image reconstruction at microwave/millimeter-wave frequencies

3.1. Introduction

Microwave and millimeter-wave imaging for breast cancer detection, as previously mentioned, have the significant advantages of employing non-ionizing radiation and requiring relatively low-cost equipment [40], [62], [113], [114], [115], [116]. In addition, this kind of systems is meant to be operator independent. The main principle of such imaging technologies relies on the dielectric contrast between healthy and diseased tissues, which allows to discriminate between healthy and damaged tissues [68], [117], [118].

As already investigated by previous works, the potential resolution of the system is one of the most important advantages of microwave imaging technologies. In this context, the use of millimeter waves represents an advantageous trade-off regarding the issues of resolution and penetration depth. Using higher frequencies results in better image resolutions since the ability to detect objects is directly proportional to the wavelength (shorter wavelengths allow for the detection of smaller objects), even though at the cost of reduced penetration capability within tissues due to more pronounced attenuation and dispersion phenomena through the investigated medium. Moreover, breast in healthy conditions is mostly composed by fat, which has a low relative permittivity. The changes of the dielectric properties of the

material encountered by an electromagnetic wave determine a variation of the speed of the wave, which is reduced by a factor depending on the refractive index of the medium. This helps in reducing the wavelength and improving resolution.

Radar-based and tomography are the two main approaches adopted in this context. Nonetheless, all the proposed systems, to date, do not exceed operational frequencies of about 15 GHz [42]. As a result, they often suffer from poor resolution, which may lead to challenging image interpretation from physicians [40], [41].

Thus, the main aim of this Chapter is to examine the possibility to develop a microwave/mm-waves radar-based imaging system working up to 40 GHz. The radar imaging technique originated from military applications and ground-penetrating radar (GPR) and was proposed for breast cancer detection in the late 1990s. It employs the well-established radar principle, in which low-power short pulses are transmitted and received at various locations by an array of antennas. The time delay between the transmitted and received pulses, as well as the shape of the received signal, provide information about the presence and the position of the scatterer. The processed signals from different locations of the antenna array elements are combined to create a 2D or 3D image that shows the position of a highly reflective object, indicating malignant tissue [29].

The concept of using mm-wave frequencies has recently been investigated, focusing on potential radar imaging applications for breasts with high fat content. This requires working on the dielectric characterization of breast tissues, creating breast phantoms suitable for mm-wave operations, and validating the working principle of the device through simulations and preliminary setups [7], [8], [11], [15], [68], [69].

It has been demonstrated that penetration of a few centimeters is possible while ensuring reasonable safety margins, specifically concerning tissue heating of the investigated biological tissues. The safety limits related to the exposure to electromagnetic fields are defined by the ICNIRP (International Commission on Non-Ionizing Radiation Protection) and are divided into two classes: the former concerns *basic restrictions* involving directions on quantities related to biological effects, such as specific absorption rate (SAR), current density and power density [119]. The latter relates to *reference levels* including quantities derived or extrapolated from relevant basic restrictions given in the first part. Among these quantities there are the electric field strength, magnetic field strength and magnetic flux density.

Normally, SAR and current density parameters are not provided in the mm-wave frequency range because they are not relevant at these frequencies. The main biological effect regarding the interaction between the mm-waves and the human body was found to be the thermal one. Moreover, at such high frequencies, absorbed power density becomes the dominant measurement. Thus, taking into account the temperature variations is of paramount importance beyond the directions provided by the ICNIRP guidelines. As an example, in [41] a full-wave model has been developed and tested to analyze

the variations occurring among the most relevant dosimetric quantities within the breast tissues. It has been observed that considering an antenna-to-skin distance of 15 mm and a transmitting power of 100 mW, the highest SAR values are observed in the skin area, but a sharp drop of this quantity occurs within the other breast tissues. This leads to the conclusion that within breast tissues, no significant safety risks are expected for the patients. One main practical drawback relies in the fact that having most SAR under EM exposure in the skin layer, not penetrating into the tissue, may complicate the imaging scenario when imaging deeper tissues.

The proposed system for breast imaging is based on a multi-static radar architecture. The development of the device presented in this Chapter relies on a similar system which has been characterized and validated previously in [41], [42]. In [42], the authors developed a system consisting of M antennas capable of transmitting and receiving signals in the microwave domain. Specifically, when one antenna is used for transmission, the other M-1 are used for receiving the reflected signal. This acquisition procedure is repeated M times, using each antenna as the transmitter. The number of transmission-reception combinations, then, is M(M-1), and the coherent summation of these signals results in an improvement of the power of the received signal by a factor of $(M(M-1))^2$ [41]. For what concerns the signal-to-noise ratio (SNR), the following considerations can be done. The noise, assumed to be white, is integrated M(M-1) times, thus improving the SNR by a factor F=M(M-1) (considering an ideal case). This study represents one of the first experimental tests of an innovative mm-wave imaging system for early-stage breast cancer detection, where the validation has been done using similar phantoms (i.e., gelatin- and agar-based) to those developed in the present thesis and presented in Chapter 2.

The objective of the present Chapter, indeed, is that of realizing a novel improved imaging setup extending the possible applications against the one described in [41], [42]. In particular, one of the aims of this work is that of exploring the potential and the limitations of a radar system that uses microwaves and millimeter waves for biomedical applications. Firstly, an analysis of the system is reported using three types of antennas, allowing for the possibility to investigate the scenarios of interest in three different frequency bands: a couple of either X-band antennas (8.2 GHz – 12 GHz), Ku-band antennas (12 GHz – 18 GHz), and K/Ka-band antennas (18 GHz – 40 GHz) have been employed for the definition of a standard for acquisition purposes. Both the hardware characteristics and the system acquisition parameters have been investigated in order to establish a signal and image acquisition protocol.

The former involve the investigation of antenna characteristics, cross-talk phenomena, background noise and the impact of the machine's frame on the acquired signals and the evaluation of the performance of the system depending on the use of anechoic material. The latter, instead, include the choice of the acquisition frequency band, number of points of the Fourier

transform of the signals and the analysis of the impact of the Intermediate Frequency (IF).

Once the main characteristics of the system have been investigated, some analyses regarding the ability of the proposed device to detect a target have been conducted. During this phase the signal propagation between a transmitting and a receiving antenna across the system has been studied from a time-domain point of view. This investigation demonstrated that the received signal carried effective information about the position of the target.

After the evaluation of the above-mentioned points, the proposed imaging prototype has been tested in reconstructing images in both a simulated and an experimental environment encompassing numerical and physical tissue-mimicking phantoms, respectively, having various dimensions and composition. To perform the experimental acquisitions, in order to get the reconstructed images, some changes within the system have been implemented. Particularly, the system was equipped with two micro-step actuators where the two antennas were fixed. This configuration allows for the controlled displacement of the two antennas creating a synthetic linear array of 24 antennas (for K/Ka-band measurements). The Delay and Sum (DAS) imaging algorithm, as well as the Filtered-Delay Multiply and Sum (F-DMAS), which previously proved to offer better performance in ultrasound imaging [120], have been employed to reconstruct images from the collected electromagnetic signals. The employed tissue-mimicking breast phantoms used in this framework refer to those developed and characterized in Chapter 2.

3.2. Development of an experimental setup for microwave/millimeter-wave imaging: a proof of concept

3.2.1. Overview on the novel hardware device

The imaging measurements performed through the experimental setup described in [42] yielded promising results, as discussed in the previous section. Nonetheless the hardware structure of the system had some issues, especially in terms of stability of the structure. The frame was unstable, and even small vibrations caused by the movement of the antennas via motors could affect the quality of the measurements.

The first step towards the realization of the new system was the renewal of the machine's frame, using more solid and stable aluminum rods. This resulted in an improved outcome, as shown in Figure 3.1. The new frame provided greater system stability. Moreover, the realized structure has larger dimensions, allowing for the investigation of a wider space. The frame measures 75x75x75 cm^3.

Another novelty introduced against the previous setup, as already mentioned, concerns the type of antennas. Previously, PNR180 antennas were used, covering the K-band and Ka-band with a working frequency range of 18-40 GHz. In the new system, besides the PNR180 antennas, two other types of antennas could be housed and tested: X-band antennas covering 8.2-12 GHz frequencies and Ku-band antennas covering the 12-18 GHz range. This allowed to have a comprehensive overview of a frequency range that nearly covers the entire 8.2-40 GHz band.

The proposed experimental setup for radar-based image acquisitions was initially composed as follows:

- a two-port VNA (Keysight ENA Network Analyzer E5080B), working in the frequency range from 100 kHz to 44 GHz, to generate the signals and record the scattering parameters for each transmitting/receiving configuration;
- two flexible coaxial cables with high performance, to connect the VNA to the two antennas;
- a couple of waveguide antennas (i.e., either covering X-band, Ku-band, or K/Ka-band (PNR180)) for the signal acquisition, fixed together on the above aluminum rod of the frame at a distance depending on their physical dimensions;
- two micro-step actuators (Zaber T-LSM200A) used to hold the antennas and allow their movement in the intended positions for the generation of a synthetic linear array (used for imaging purposes);
- the above-mentioned aluminum frame covered in its inner side by anechoic panels.

Specifically, different geometric configurations of the anechoic panels have been studied in this framework, in order to assess whether they could improve the quality of the collected signals by suppressing external unwanted interferences.

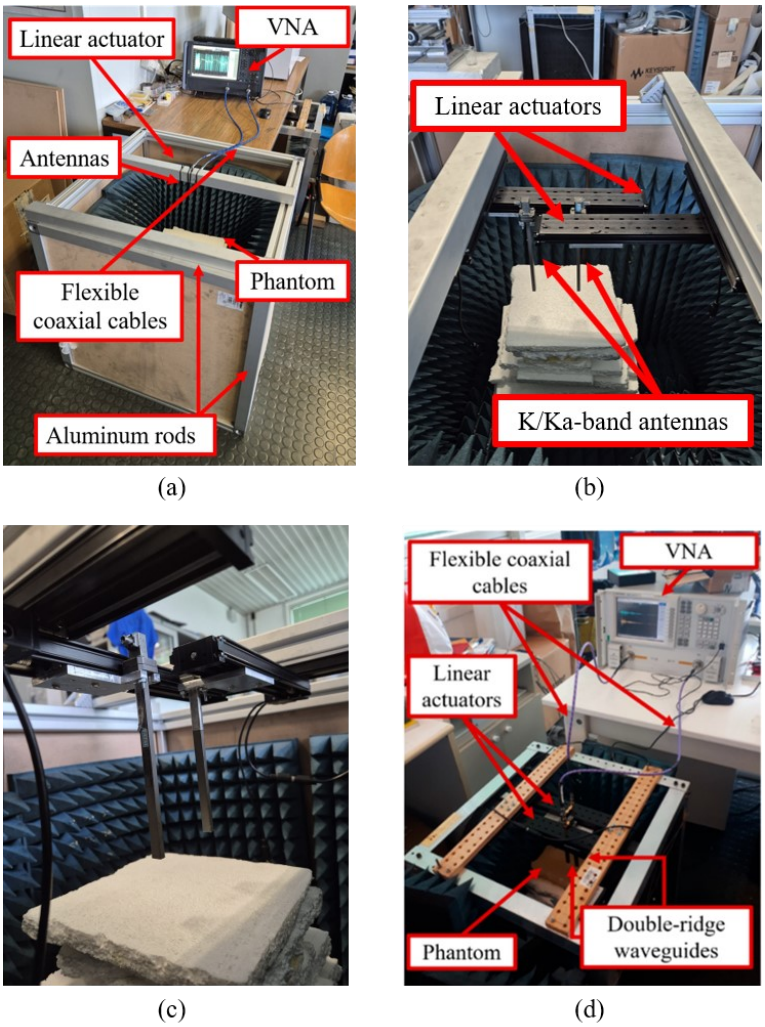

Figure 3. 1: Developed system for radar-based microwave and millimeter wave image acquisitions (a) (details on the linear actuators and the antennas are provided in (b) and (c)), improved version of the system proposed in **[42]** (d).

3.2.2. System characterization: processing of the acquired data and definition of a protocol for signal acquisition

The first step to test the aforementioned system consisted of evaluating its performance in terms of the acquisition of radar signals. To do this, signals were collected by using a single couple of antennas, working at three different frequency bandwidths. The antennas were fixed together on the top rod of the described device, as close as their physical dimensions allowed (Figure 3.2). The measurements described in this section, thus, did not required the two linear actuators to move the antennas, as no synthetic array was required at the very first stages of the analysis of the system. After setting the acquisition parameters, measurements were saved and analyzed, in order to study the propagation of radar signals over the novel system. Particularly, the output data collected by the VNA are given as a text file

containing a scattering matrix reporting the values in terms of magnitude (dB) and phase (deg) of the acquired S_{21} transmission parameter. They were subsequently processed using MATLAB to obtain the system response in the time domain through Fourier transform processing. Some considerations about the optimization of the acquisition and processing parameters implied in the proposed measurement procedure will follow.

Acquisition frequency band Both the calibration of the system and the acquisitions of the signals have been carried out on a wide frequency band ranging from 10 MHz to 44 GHz. This has been done to cover all the operational frequency bands (i.e., X-band, Ku-band, K/Ka-band,) of the different couples of antennas employed in this analysis. Specifically, the calibration has been performed automatically through the *e-cal* (i.e., N4693D Series 2-ports Microwave ECal module, Keysight). This has been done for practical reasons due to the equipment where the propagation of the EM waves through coaxial cables might cause measurement errors. Thus, the calibration has been performed up to the antenna apertures. It has been demonstrated that a calibration within selected frequencies according to the operational ranges of the three different types of antennas does not significantly improve the quality of the acquired signals. Moreover, as a matter of fact, calibrating the VNA in a specific narrower frequency band (i.e., 12-18 GHz, when using Ku-band antennas), results in an expansion of the time axis which may fail the sampling theorem. This may partially represent a problem, which can be controlled by modifying the number of acquired points.

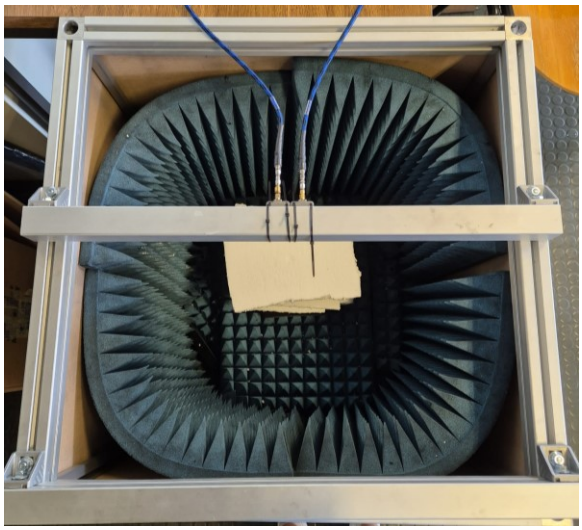

Figure 3. 2: Experimental setup for radar-based signal acquisition equipped with a couple of Ku-band antennas fixed together on the top aluminum rod.

Number of points of the Fourier transform To properly reconstruct the time-domain signals avoiding aliasing phenomena, an investigation aimed to

define an optimum value of the number of points of the Fourier transform has been conducted. Specifically, the number of acquired points within the 10 MHz-44 GHz frequency band for the Fourier transform has been set at 4001. At the same time, a zero-padding technique has been used to thicken the time-domain response. Zeros have been added up to 88 GHz in the frequency domain signal, twice the maximum operating frequency of the VNA. This allows for achieving a time step (t_s) of nearly 0.01 ns which ensures a correct and reliable representation of the system's complete response in the time domain, with all the three different acquisition frequency bands. These considerations have been done even in order to satisfy the sampling theorem:

$$f_{max} = \frac{f_S}{2} \tag{3.1}$$

Indeed, a t_s of 0.01 ns results in a sampling frequency f_S of 100 GHz which ensures a maximum visible frequency f_{max} of 50 GHz, covering more than the set acquisition bandwidth.

No significant improvements have been achieved by increasing the number of the acquired points. A comparison between the time-domain trends of acquisitions carried out through all the antennas (X-band, Ku-band, K/Ka-band) with both 4001 and 8001 points in the frequency domain has been conducted. However, these analyses proved that the additional information is not significant, as the behavior of the responses is nearly identical. Therefore, 4001 points has been set as a standard for the acquisition points parameters since, even in the more critical case of the PNR180 (i.e., K/Ka-band), there are no benefits from increasing the frequency resolution of the sampled signals. Instead, it would only result in a heavier computational load for signal processing.

Choice of the IF bandwidth Another investigation on how to improve the acquired signals has been performed by changing the IF (Intermediate Frequency) VNA parameter. The IF is the frequency where the measured signal is shifted within the VNA for processing. Particularly, the analysis concerns the bandwidth of the IF. Indeed, a high IF bandwidth allows for faster signal acquisition times but at the cost of increased sensitivity to noise. The problem caused by the noise could be fixed by averaging the acquired signals. This means acquiring the system response *n* times (with *n* = number of signals) and averaging the *n* signals before the actual acquisition. This approach aims to eliminate all time-varying factors within the signals while preserving the time-invariant components that characterize the system. However, this results in longer scanning times because the signal must be acquired *n* times for each acquisition. Hence, a general reduction in noise in the signal as the IF decreases and the number of averages increases is expected.

In this framework, six different combinations of IF values (i.e. IF = 1 kHz, 100 kHz) and number of averages on the signals (i.e., #averaging = 0, 10, 100) have been performed within acquisitions through all the antennas to evaluate which one would have improved the quality of the collected signals. The tests

were conducted using all three types of antennas in the configuration of short-circuited cables. As an example, Figure 3.3 shows the frequency-domain trends of the acquired measurements in Ku-band, where the effects of changing IF and the number of averages is particularly noticeable at the out-of-band portions of the spectrum. For example for frequencies below 7-8 GHz, where the cut-off of the waveguides dominates (thus no signal is collected), the noise floor ranges from about -80 dB to -140 dB.

Since performing averages and lowering the IF bandwidth parameter to 1 kHz unnecessarily lengthens acquisition times, the initial condition of IF at 100 kHz and without using averages was chosen as a standard for the acquisitions. The total time required for a single acquisition, thus, was found to be equal to 69.79 ms.

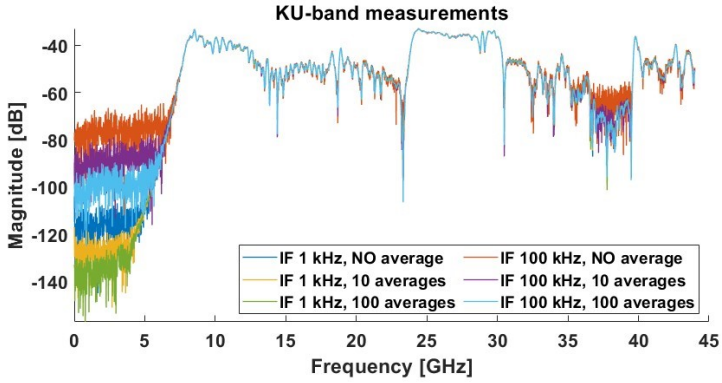

Figure 3. 3: Comparison between measurements in Ku-band by varying the acquisition parameters of IF (i.e., 1 kHz or 100 kHz) and #averaging (0 (NO average), 10 or 100).

Once the MATLAB routine robustness had been checked along with the selection of the parameters for signal acquisition and processing, the actual tests on the new hardware system started. The final aim of this whole investigation was to define a complete protocol for radar-based signals acquisition in a perspective to accurately employ the system even in terms of image acquisition and reconstruction. The realized device was evaluated in several aspects: first, measurements were made to assess whether the aluminum frame had an impact on the signals collected by the three different couples of antennas. Subsequently, tests were made to evaluate the influence of the anechoic material in reducing the background noise. Moreover, the evaluation of the contribution of the crosstalk phenomenon between antennas, as well as an analysis on the power of the involved signals is provided.

Influence of the aluminum frame on the collected signals To check the impact of the aluminum frame, two types of measurements were compared: measurements conducted with the antennas in the central position of the frame and measurements with the antennas in an angular position near the aluminum rods. These measurements were made for all three antennas (X-,

Ku- and K/Ka-band) keeping the acquisition parameters chosen in the previous section. Below in Figure 3.4 the comparative measurements for the various types of antennas are reported.

The whole analysis is focused on the performance of the transfer functions in the time span of 0-20 ns, which is the time span that mostly affects the distances involved in our study. This time range corresponds to a propagation distance of nearly 6 m, which is sufficient to study the system given its physical dimensions (i.e., 75x75x75 cm^3).

Indeed, it can be seen that there are differences between the central position and the angle of the frame for all three types of antennas. The general trend is however preserved; this suggests that the frame can have a certain impact on the signals, whose significance depends upon the specific application, and on the accuracy of the intended results.

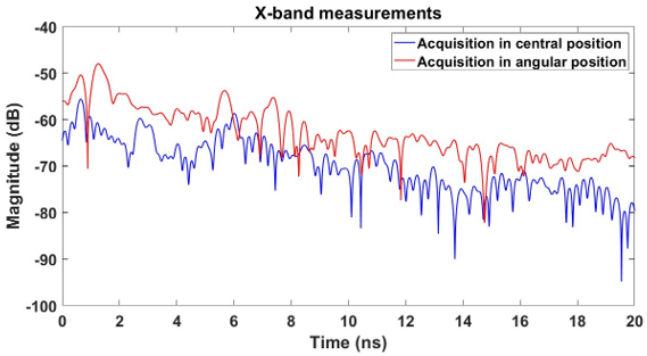

(a)

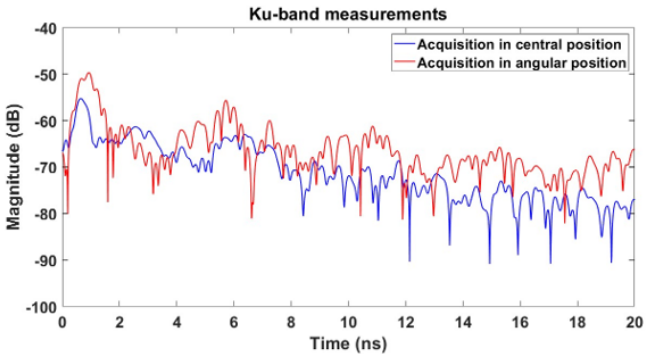

(b)

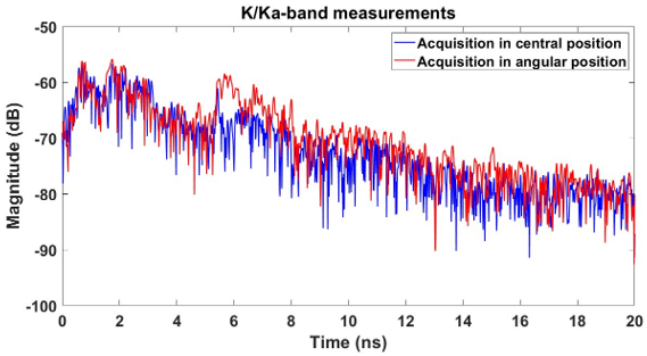

(c)

Figure 3. 4: Comparison between acquisitions at three different frequency bands ((a) X-band, (b) Ku-band, (c) K/Ka-band) performed from different position within the system: resulting transfer functions collected from antennas in central position (blue trace) and in angular position, in proximity of the aluminum rods (red trace).

Influence of the anechoic panels on the collected signals Subsequently, the influence of the anechoic panels was evaluated. To this purpose, signals acquisitions were carried out including the anechoic panels within the system. Specifically, the anechoic layer has been arranged in two different configurations – i.e., flat and circular as shown in Figure 3.5. The tests have been done for all three types of antennas in both the aforementioned spatial positions.

The plots presented in Figure 3.6 illustrate the time-domain transfer functions and their combined difference with and without the anechoic panels in place. As an example, only results in Ku-band are presented. The obtained traces have similar trends in all configurations. Nonetheless, a difference of almost 10 dB in the presence or absence of the anechoic can be observed. At the same time, it has been noticed that the two different configurations of flat and circular anechoic material do not differ significantly. The presence of the anechoic panels was therefore considered necessary and the circular configuration, which had slightly better performance, was chosen as a standard for acquisitions.

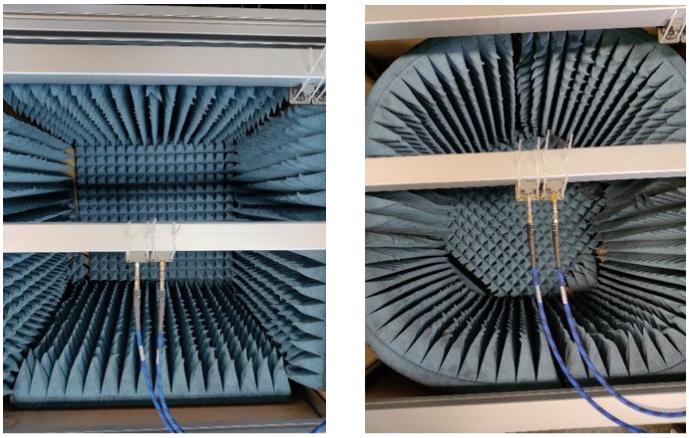

(a) (b)

Figure 3. 5: Experimental setup for signal acquisition with anechoic panels in flat (a) and circular (b) configurations.

Crosstalk signal evaluation Finally, the crosstalk signal between the two antennas used during the measurements has been evaluated. Crosstalk refers to the unwanted transfer of signals between different channels. This phenomenon is a common issue in various types of communication systems. Particularly, in this case, it occurs due to the signal propagating from the

transmitting to the receiving antenna which causes interference and disturbances and may reduce the quality of the overall useful signal. This can lead to errors and decreased performance within the imaging system.

To quantify the effect of the crosstalk, preliminary measurements have been conducted, initially, without any target object in place. This has been done to avoid the target influencing the propagation of the involved signals within the acquisition and highlighting the only contribution of interest (i.e., the mutual coupling between the antennas).

Figure 3.7 shows the time-domain signal of an acquisition performed through the Ku-band antennas. As can be noticed, the strongest peak of the trace can be found at 0.647 ns – which corresponds to a distance of about 19 cm. This represents the trip conducted by the signal between the two antennas including the path across the whole circuitry and waveguides. This kind of measurement is fundamental when performing imaging tests. Indeed, the crosstalk signal is always acquired to quantify its effect and to calibrate the data from imaging acquisitions. Particularly, by subtracting the measurement carried out with and without the target in place, it is possible to remove this unwanted component from the signals to be imaged. Further discussion on this point will follow in Section 3.3.3.

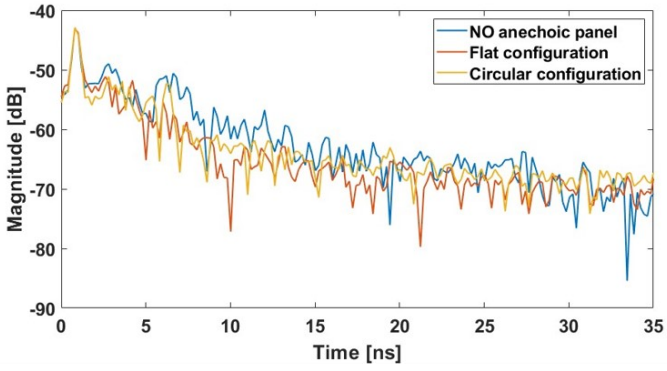

(a)

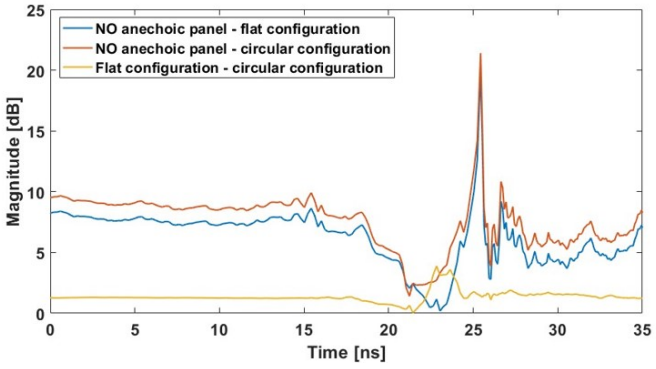

(b)

Figure 3. 6: Comparison between the transfer functions of acquisitions in Ku-band with and without anechoic panels (a); differences between each pair of traces in the previous panel (b).

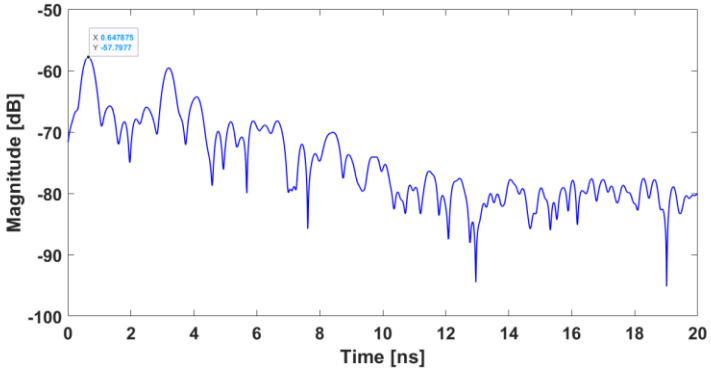

Figure 3. 7: Transfer function from Ku-band acquisition in air. The strongest peak refers to the crosstalk between the two antennas.

3.2.3. Target detection measurements

After setting the parameters for signal acquisition and processing, various tests have been conducted, aimed at detecting a specific target by varying the distance from the antennas. The purpose of these tests was to determine the maximum distance (if any) where the target is no longer detectable, which helps to set utilization limits for the new setup.

For this investigation, the designated target was initially a metallic plate which was placed at different distances (d), ranging from 20.5 cm to 60.9 cm (d_{max}), from the antenna apertures (Figure 3.8). A metallic target represents a good standard for detection with electromagnetic waves due to its high reflectivity and conductivity. Metals reflect a significant portion of the incident electromagnetic energy, creating strong and distinguishable signals. This high reflectivity enhances the contrast between the metallic target and its surroundings, making it easier to be identified and located.

Measurements were made through antennas operating in the Ku-band under consistent conditions for all tests, with the antennas in central position against the aluminum frame and in a circular anechoic configuration as explained before.

From the time-domain traces of these tests, two prominent peaks are expected: the first would be related to the aforementioned crosstalk phenomenon and the second to reflections from the plate. Analyzing these peaks allows for the observation of two different aspects: the stability of the first peak, which should remain constant over time and for all the performed measurements, and a reduction in the power of the second peak, located at a temporal position based on the distance of the target.

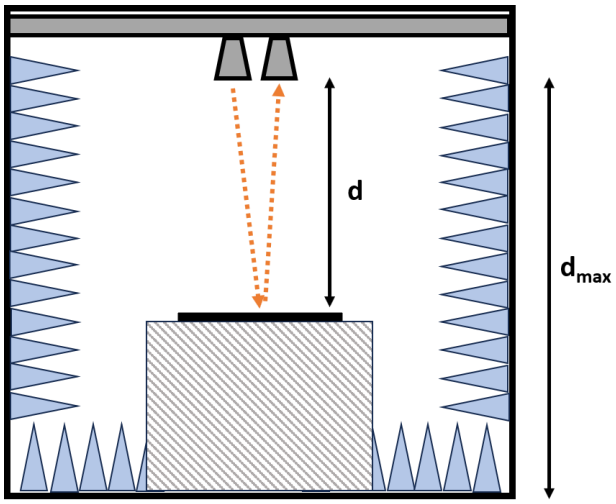

Figure 3. 8: Schema of the experimental setup for target detection.

The peak detection process was performed automatically using a specific function in MATLAB, which identifies local maxima based on user-defined parameters. Figure 3.9 shows an example of the time-domain signals with the target positioned at 20.5 cm (a) at a 60.9 cm (b), respectively (i.e., the minimum and the maximum distances considered for this target detection analysis). The labelled peaks correspond to the abovementioned crosstalk and the reflected echo from the metallic plate. The reported distances refer to the time of flight of the signal in the round trip from the cable aperture to the reflection point (including waveguides and transitions). As can be seen from the figure, the detected peaks related to the crosstalk between antennas occur at almost the same time instant, allowing for the conclusion that this phenomenon is time-invariant and independent from the distance of the target.

For what concerns the strongest peaks, which are supposed to be the ones related to the metallic plate reflections, it can be observed that they are not placed at the expected distance. For this reason, a calibration procedure seemed necessary, comparing the expected and the measured distances.

The expected distances of the target were measured with a laser rangefinder at the antenna apertures. In Figure 3.10 a comparison between the detected and the expected peak distances are presented. This representation suggests that, in addition to the mathematical calculation of the distance based on the wave time of flight, another element must be considered. Indeed, during each of these target detection tests, the signal also propagates a few centimeters inside the antenna itself before leaving the antenna aperture and propagating through air.

Therefore, the actual measured distances were calculated based on the measured wave's time of flight (t_{peak}) with a contribution given by a certain offset (d_{offset}) using the formula:

$$d_{target} = \frac{t_{peak}}{2} * c - d_{offset} \tag{3.2}$$

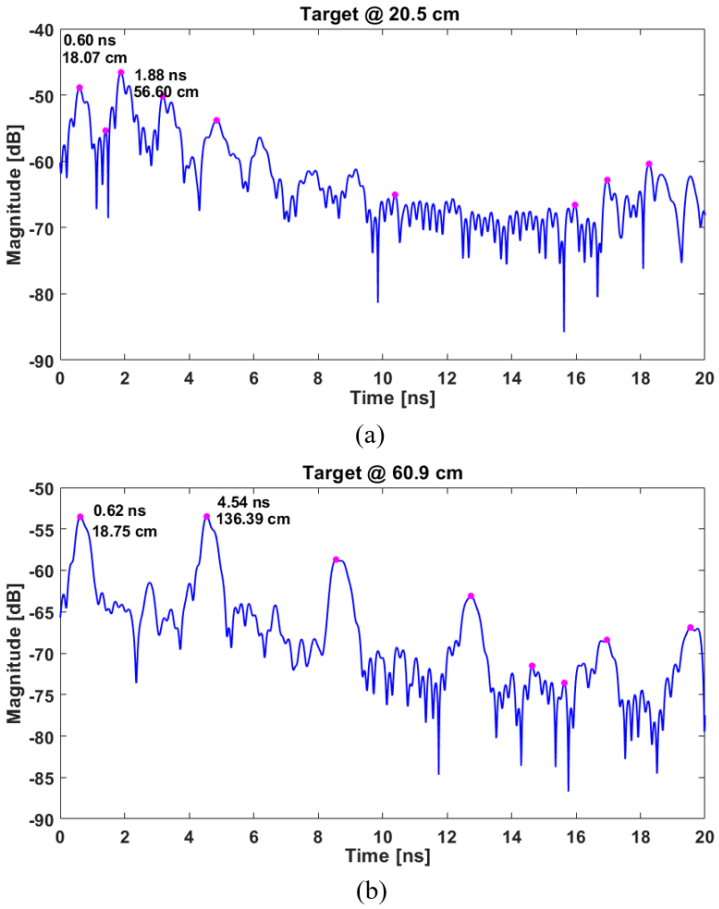

Figure 3. 9: Transfer function from Ku-band acquisitions with the target positioned at 20.5 cm (a) and 60.9 cm (b) far from the antenna apertures.

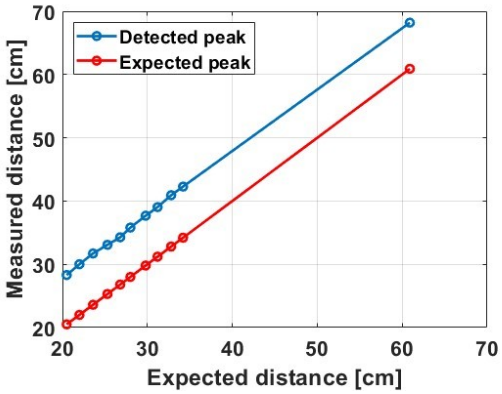

Figure 3. 10: Comparison between the expected and detected peak distances.

The offset distance has been calculated by placing the antennas (in this case, the Ku-band ones) face-to-face and identifying the peak indicating the signal reflection. This measurement revealed a peak at 0.511 ns, which corresponds to

a distance of about 7.67 cm. This last value has been considered as d_{offset} and was subtracted to the detected peak distance, resulting in an alignment between the measured and the expected distances, as shown in Figure 3.11. This correction reveals that the radar system and the developed MATLAB routine can precisely detect the target in space using the scanning parameters defined in the previous sections.

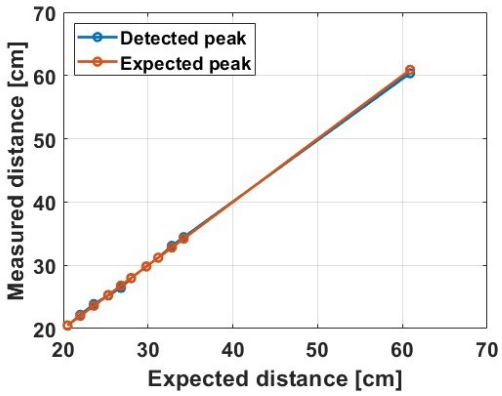

Figure 3. 11: Comparison between the expected and detected peak distances after the calibration given by the offset distance.

After identifying and adjusting the detected distances based on the varying position of the metallic target, a procedure was conducted to calculate the return power of each signal. Specifically, every peak of interest went through a windowing process, in which a portion of the time-domain trace was selected where the signal falls below the threshold of 10 dB relative to the peak power. After selecting the window corresponding to the peak of interest, a zero-padding procedure was performed. This results in a time-domain signal containing only the information related to the echo from the target. Thus, a Fourier transform of the obtained signal was computed. This operation yields the desired power information in the frequency domain. Finally, the power of this signal at 15 GHz was selected, to provide a punctual representation of the power related to each signal. Overall, the performed tests, conducted by varying the distance of the metallic plate from the antenna apertures, can be summarized in Figure 3.12 (a), where the punctual value of the power of each signal is reported, as well as the value of the background noise, measured in the same experimental conditions. As can be noticed from the graph, a general decreasing trend of the power is obtained. This was expected since the electromagnetic wave can be partially absorbed or scattered by the surrounding environment, further reducing the power of the signal that returns to the receiving antenna.

This effect is expected to be more pronounced at higher frequencies. Indeed, a further analysis has been conducted where the same procedure calculating the return power with the target positioned at d_{max} was repeated for all types of antennas. Figure 3.12 (b) shows the general trends in the frequency domain of the windowed signals corresponding to the acquisitions with the target at d_{max}. The figure shows that even in the worst-case scenario (via high-frequency acquisition in K/Ka-band with the target located as far as possible from the

antennas) the power margin against the background noise is still sufficient to identify the target.

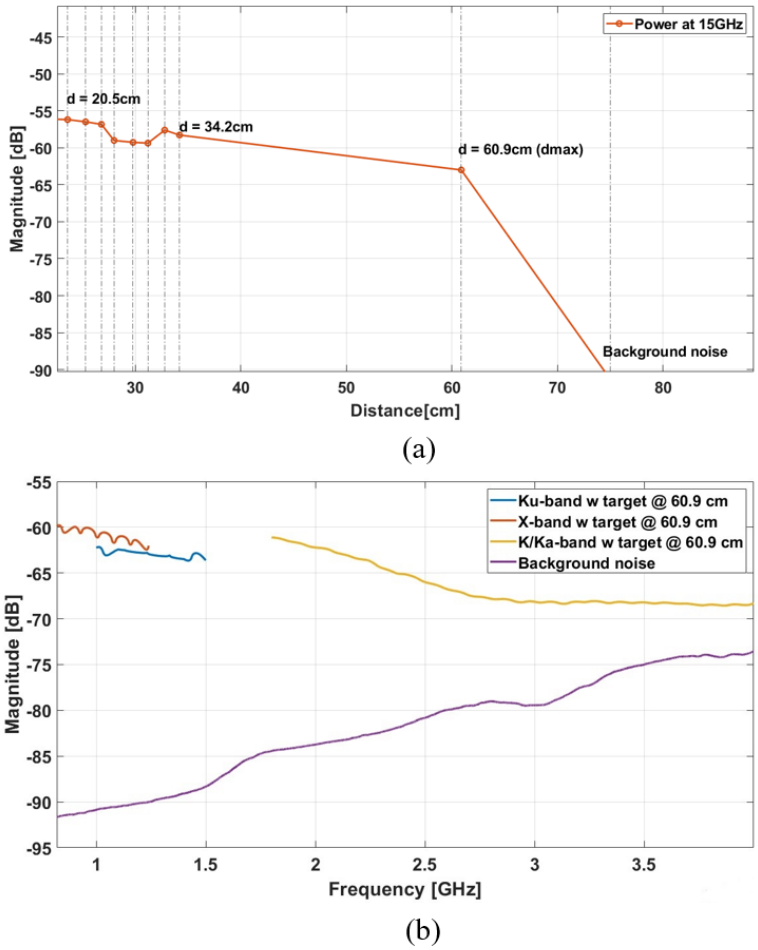

Figure 3. 12: Punctual values of the return power of the peaks corresponding to the target positioned at varying distance, for Ku-band acquisition (a). Comparison between the trends of the return power when the target is positioned at d_{max} across the different frequency bands acquisitions (b). All these results refer to acquisitions performed with IF set at 100 KHz.

After conducting measurements involving the metallic plate as a target, further investigations have been performed using some preliminary phantoms. In particular, homogeneous healthy-like phantoms (i.e., G3.3O66.6) of different thicknesses (i.e., 1, 1.5, 2, 2.5 and 3 cm) were used to validate the designed protocol. To conduct these tests, a slice of phantom was positioned above the metallic plate, in such a way the first interface encountered by the signal was at d = 22 cm far away from the antenna apertures, regardless of the thickness of the phantom.

In this case, one more prominent peak, for a total of three peaks, is expected in the time-domain trace of the acquisitions. This measurement configuration, including phantoms of various thickness determines the presence of one more interface. Thus, the signal will show the crosstalk peak,

the peak related to the first encountered interface (air-phantom) at around d = 22 cm and the peak related to the second interface (phantom-metallic plate). The position of this last peak will depend upon the thickness of the phantom. As a graphical example of the time-domain trace obtained from such measurements, Figure 3.13 is reported. This acquisition, specifically, involved a phantom with 1.5 cm thickness. Firstly, it is worth noticing the stability of the peak related to the crosstalk between antennas, which again occur around almost 18 cm, showing consistency with the previous results with and without any target. Moreover, as can be seen from the picture, again, the displayed distances are not as expected. For this reason, the same correction of data has been performed following Equation (3.2). Regarding the measurement shown in Figure 3.13, this resulted in locating the first interface (air-phantom) at around 22 cm, while the second one is positioned at almost 27 cm. The spatial distance between these two peaks is about 5 cm, which is about three times the actual thickness of the phantom. This was expected, since it is known that the speed of propagation of the EM wave through a medium which resembles the human fat is less than the speed of light (c) [42]. Specifically, the speed of propagation through a different medium than air (v) can be calculated as follows:

$$v = c/\sqrt{\varepsilon_r} \tag{3.3}$$

where ε_r indicates the dielectric permittivity of the considered medium at a certain frequency. This results in increasing the time of flight through the actual phantom and it is clearly visible on the time-domain trace. In particular, $\varepsilon_{G3.3o66.6}$ at 15 GHz is 10.13, determining a speed of propagation of 9.425*10^7 m/s, which is 3.18 times smaller than the speed of light c.

A further analysis concerning the return power of the peaks related to the two interfaces has been conducted as well. In particular, the difference between the power of the peaks was calculated while increasing the thickness of the phantoms. The results of this investigation are depicted in Figure 3.14, where a trend of increasing power difference can be noticed. This is expected firstly due to the Lambert-Beer law. Moreover, this analysis proves that by increasing the thickness of the phantom under test, more power suffers from absorption effects. Specifically, the dielectric properties of the fat-like phantom determine its ability to absorb electromagnetic wave energy. As the wave passes through the medium, some of its energy is converted into heat or other forms of internal energy within the material, thus reducing the power of the reflected wave. Thus, this analysis can help in setting the upper limit of the thickness of the phantom inserted within the system, which allows to stay within the power budgets of the graphs presented previously.

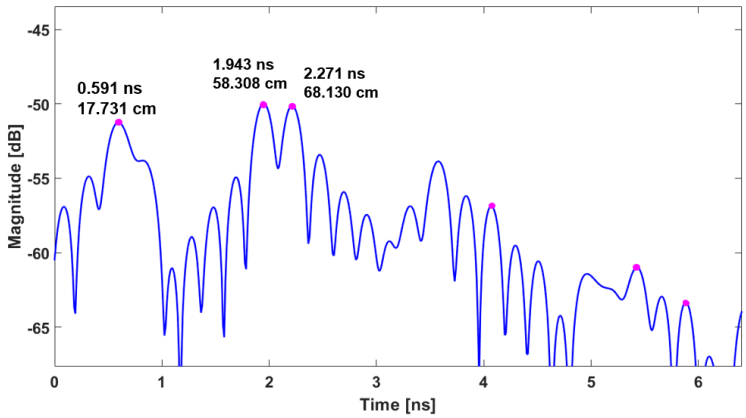

Figure 3. 13: Example of a time-domain trace from acquisition in Ku-band with a phantom of 1.5 cm thickness.

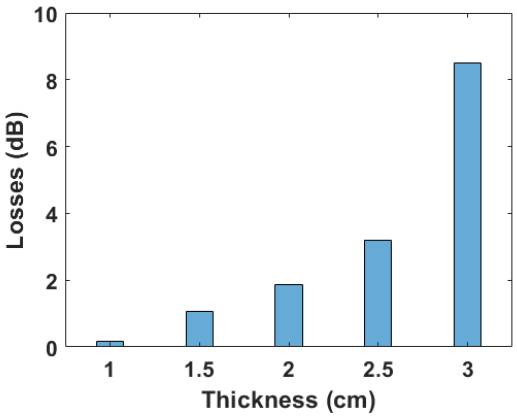

Figure 3. 14: Increasing trend of the power losses depending on the thickness of the phantom under test.

3.3. Image reconstructions through *Delay and Sum* (DAS) and *Filtered-Delay Multiply and Sum* (F-DMAS) algorithms

3.3.1. Background on DAS and F-DMAS algorithms and design of the imaging scenario

Over the past decades, in the context of early breast cancer detection, multiple microwave imaging techniques have been developed [32]. As already explained, both microwave tomography [32], [121] and ultra-wideband radar-based method have been explored achieving promising results [31], [33], [34], [122], [123], [124], [125]. In this section, one of the most common confocal radar imaging techniques will be explored, which

employs the Delay and Sum (DAS) beamforming method. This method, which has the advantages of a simple implementation and real-time imaging capability [126], has been firstly introduced by [31], [122], [123] and relies on the improvement of signal reception from a specific direction by aligning the phases of signals received by an array of sensors. It is known from the literature that the most common frequency band of such application ranges between 1 and 10 GHz. The aim of this work was to apply such algorithm to obtain 2D image reconstructions even at higher frequencies, up to the millimeter-wave range using a novel microwave imaging system as described previously.

The DAS beamformer algorithm is described through the following equation:

$$y_{DAS}(t) = \sum_{i=1}^{N} x_i(t - \delta_i) \tag{3.4}$$

where $y_{DAS}(t)$ is the output of the beamformer, t is the time index, N is the number of the elements within the considered array and $x_i(t)$ and δ_i are the detected signal and the corresponding time delay.

Even though the DAS beamforming algorithm represents the one of the most common technique in medical imaging (particularly in ultrasound imaging), it suffers from poor spatial resolution and limited off/axis interference rejection [127]. For this reason, several more advanced beamforming algorithms have been presented earlier [3]. These reconstruction algorithms include Delay Multiply and Sum (DMAS), Improved Delay and Sum (IDAS), Coherence factor-based DAS (CF-DAS). In this thesis, the Filtered-Delay Multiply and Sum (F-DMAS) beamforming algorithm has been adopted as well, since, within the literature, it proved its ability in enhancing resolution, dynamic range and the overall quality of the reconstructed images in ultrasound imaging [120] and in mm-wave imaging [41], at the cost of requiring longer computational time [3]. This method consists, firstly, in time-shifting the received signals, as in DAS approach. Once the RF signals are re-aligned, they are multiplied in all the possible pair combinations among them. Thus, further processing operations, including square root of the absolute values of the multiplied couples, are applied and finally the resulting signals are band-pass filtered to pass the second-harmonic component only [127].

In this thesis, in order to achieve 2D image reconstructions through DAS/F-DMAS methods of both numerical and experimental acquisitions, an analysis on the optimization of the scenarios has been conducted. From a numerical point of view, acquisitions were performed within the three different frequency bands introduced previously (X-band (employing 10 antennas), Ku-band (employing 14 antennas), K/Ka-band (employing 28 antennas)). The experimental measurements, instead, involved only K/Ka-band acquisitions following the same procedure proposed in [42]. Thus, 24 antennas were employed, which were positioned along a linear array with a shift of λ/2 (i.e., 5 mm, half wavelength in air at 30 GHz).

The considered 2D field of view to be imaged has been designed to cover a lateral distance along the X axis (where the antenna array is placed) of 135 mm while the depth (Z axis) has been set to investigate 100 mm below the antenna apertures.

The DAS and F-DMAS algorithms have been implemented in MATLAB and several investigations on the optimum value of each reconstruction parameter have been conducted. The next sections present the choice of such parameters as well as the results in terms of both synthetic and experimental data.

3.3.2. Numerical investigations

3.3.2.1. Optimization of image acquisition parameters

Numerical analyses represent a crucial step to develop and optimize the performance of imaging algorithms at the first stages. This analysis aimed at defining a protocol for the acquisition, elaboration and presentation of the simulated data. For this purpose, investigations on the scan parameters for reconstruction through the DAS and F-DMAS algorithms have been performed. Some considerations about the choice of the involved parameters will follow.

Gaussian pulse shape The first step of this process involved the definition of the pulse which was meant to be transmitted by the antennas. Within the literature, several formulations have been presented, including the standard Gaussian pulse, the differential one as well as the n^{th} derivative of the pulse function [112], [128], [129], [130]. The choice of the kind of pulse determines the quality of the final image, since this signal is supposed to be multiplied by each term of the scattering matrix either in the case it is obtained by simulation or measurement. This allows to calculate the radiofrequency (RF) signals received by each antenna of the considered array. For this analysis, a differential Gaussian pulse with a sine-type modulation (displayed in the equation below) has been adopted, since it revealed more precise signals and image reconstructions:

$$s_{\mathrm{TX}}(t) = \sin\big(2\pi f_0(t-4\sigma)\big)\cdot \exp\left[-\frac{(t-4\sigma)^2}{\sigma^2}\right] \qquad (3.5)$$

where f_0 indicates the central frequency depending on the frequency band of the implied antennas (i.e., X-band (f_0 = 10 GHz), Ku-band (f_0 = 15 GHz), K/Ka-band (f_0 = 29 GHz)) and σ represents the pulse width and its choice is outlined below.

Pulse width The pulse width σ, expressed in seconds, basically represents the standard deviation of the Gaussian distribution across time. However, the choice of this parameter, in the literature, is rarely justified clearly. While a relationship with the employed bandwidth is straightforward, the precise

formulation is often left to be determined. Nonetheless, in [128], the authors introduced a formulation of the parameter that come with the merit of being based on the physical postulates introduced by Heisenberg and reformulated by Gabor in 1945. The relation explains the connection between the pulse width, and the bandwidth of the system (BW):

$$\sigma = \frac{1}{4\pi} \cdot \frac{1}{BW} \tag{3.6}$$

Thus, taking advantage of this simple, and unambiguous, formulation, the pulse width has been chosen adaptively based on the employed bandwidth.

3.3.2.2. Synthetic image reconstruction

The 2D field of view for visualization has been discretized in a grid of 1000 x 1000 pixels. For each of the pixels, the corresponding time delay, based on its coordinates (x, z), has been computed. Specifically, the traveling delay (τ) and path (r) of the EM wave from a transmitting antenna to a certain point within the 2D field of view and back to the receiving antenna were estimated as follows:

$$\tau_{i,j}(x,z) = v^{-1}\left(r_i(x,z) + r_j(x,z)\right) \tag{3.7}$$

$$r_i(x,z) = \sqrt{(x-x_i)^2 + (z-z_i)^2}$$

$$r_j(x,z) = \sqrt{\left(x-x_j\right)^2 + \left(z-z_j\right)^2}$$

where (x_i, z_i) and (x_j, z_j) are the coordinates of the transmitting and receiving antennas respectively, while v is the speed of propagation of the wave in the adopted medium. The final DAS image is then obtained by applying the following equation:

$$I(x,z) = \sum_{i=1}^{M} \sum_{j=1}^{M} s_{RX\,i,j}(\tau_{i,j}(x,z)) \tag{3.8}$$

where $s_{RX\,i,j}$ represents the signal transmitted by the i-th antenna and received by the j-th antenna. Such signal is obtained by multiplying the scattering matrix (S_{21}) in the frequency domain after performing the Fourier transform to the transmitted signal as follows:

$$s_{RX\,i,j}(f) = F\{s_{TX}(t)\} \cdot S_{21\,ij}(f) \tag{3.9}$$

$$s_{RX\,i,j}(t) = F^{-1}\{s_{RX}(f)\} \tag{3.10}$$

Subsequently, the envelope detection of I is calculated through the Hilbert transform. Thus, the obtained image is presented after squaring and normalization.

For what concerns the elaboration of the signals within the F-DMAS algorithm, the process involves non-linear operations on the received

signals. The procedure adopted in this thesis has been inspired from [120]. Particularly, the square root is applied to the absolute value of the delayed signals, while preserving their sign as displayed below:

$$s^*_{n,k}(t) = sign\left(s_{n,k}(t)\right) \cdot \sqrt{|s_{n,k}(t)|} \tag{3.11}$$

where $s_{n,k}$ indicates the received delayed signal for the k-th image line collected from the n-th element of the antenna array. Thus, the obtained signals are multiplied in couples as follows:

$$I_{F-DMAS}(t) = \sum_{n=1}^{N-1} \sum_{m=n+1}^{N} s^*_{n,k}(t) \cdot s^*_{m,k}(t) \tag{3.12}$$

where N is the total number of antennas in the array. Finally, the obtained signals are summed and band-pass (BP) filtered on the second harmonic in order to remove the DC components given by the non-linearity of the combinatorial coupling.

3.3.2.3. Results

After performing the optimization on the scan parameters, some preliminary numerical tests have been conducted. Specifically, reconstructions have been achieved for all the three considered frequency bands, employing a different number of antennas which were place at a distance depending on their wavelength, as explained in Section 3.3.1.
The scattering matrices were designed *ad-hoc* with MATLAB and different scenarios have been considered. The conducted tests are summarized in Table 3.1. At first, simulated tests were conducted with a point target in air (Test1, Test2, Test3). Subsequently, a second medium has been introduced to make the scenario more complex and realistic, by introducing an interface between two media and embedding the target in the new one (Test4, Test5, Test6). This new medium is meant to reproduce the properties of a human breast fat tissue. The dielectric properties in terms of real and imaginary part of relative dielectric permittivity which were assigned to the new numerical phantom are 3.67 and 0.13, respectively. The results of these tests are displayed in Figure 3.15.

Table 3. 1: Summary of the conducted tests. $d_{interface}$ represents the distance from the line of antennas to the interface between air and numerical phantom, while d_{target} is the distance from the line of antennas to the point target. x_{target} instead is the lateral displacement of the target from the center of the antenna array.

	Medium	**$d_{interface}$ (cm)**	**d_{target} (cm)**	**x_{target} (cm)**	**Band (#antennas)**
Test1	Air	-	5	2	X (10)
Test2	Air	-	4	2	Ku (14)
Test3	Air	-	4	2	K/Ka (28)
Test4	Air + phantom	3.5	5	2	X (10)
Test5	Air + phantom	3.5	5	2	Ku (14)
Test6	Air + phantom	1	4	2	K/Ka (28)

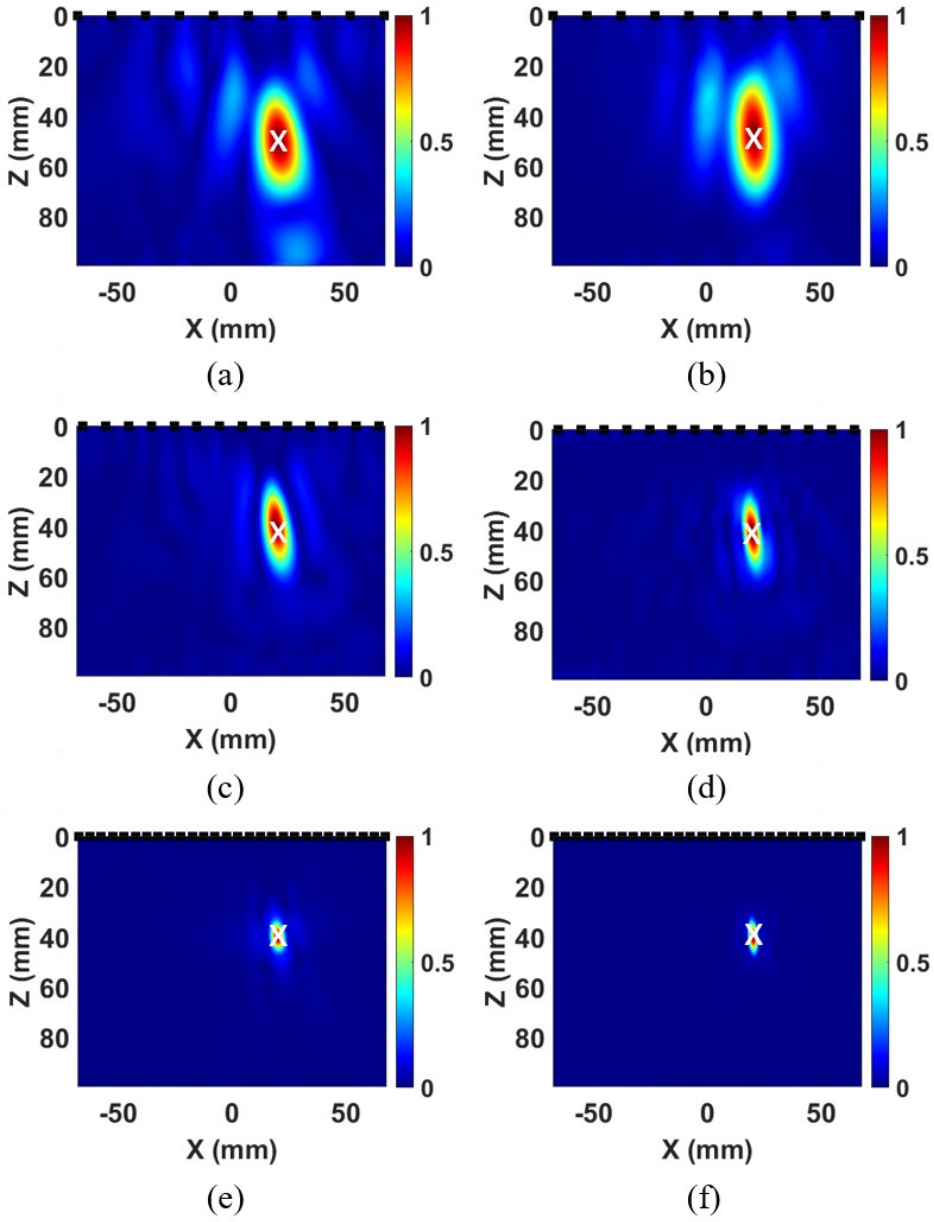

Figure 3. 15: Reconstructed images for Test1 (a), (b), Test2 (c), (d), Test3 (e), (f), with a point target in air, through DAS (left) and F-DMAS (right). The white crosses indicate the expected location of the target.

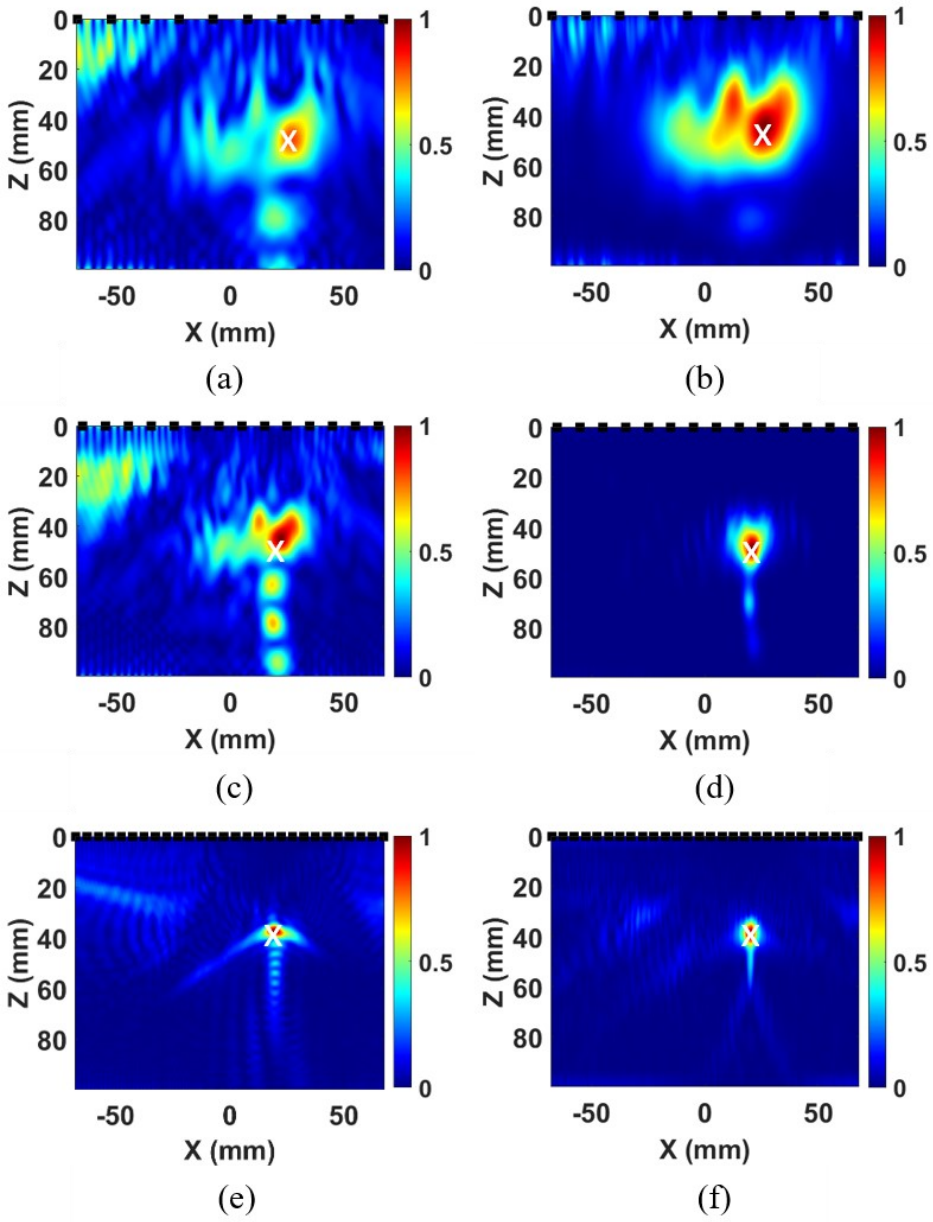

Figure 3. 16: Reconstructed images for Test4 (a), (b), Test5 (c), (d), Test6 (e), (f), with a point target embedded in a fat-like numerical phantom, through DAS (left) and F-DMAS (right). The white crosses indicate the expected location of the target.

As can be noticed from Figure 3.15, both the DAS and F-DMAS algorithms demonstrated to perform well when the numerical point target is immersed in air, showing an improvement of the contrast and sidelobes suppression, as well as a better definition of the detected target, especially when employing K/Ka-band antennas. This was expected due to both the greater central frequency and the wider frequency band of these antennas. Moreover, an enhancement of the resulting images can be observed comparing, within the same test, the DMAS and the F-DMAS reconstructions, especially in terms of artifacts suppressions. As mentioned earlier, the F-DMAS method includes the computation of backscattered signals spatial correlation within the beamforming procedure and

then employs the second harmonic-frequency component of the beamformed signal. Indeed, this results in a better detection of fine image details (i.e., the point target). A better contrast in the resulting images can be appreciated as well, between the scattering target and the uniform air background.

Similar considerations can be done for Figure 3.16, where the point target is embedded in a fat-like phantom. In this case, both the algorithms require an initial guess for the speed of propagation which can't be set equal to c due to the presence of a medium with different characteristics from air. For this reason, this quantity has been set equal to the weighted average of the speeds of the media encountered along the path from the antenna aperture to the target. The speed of propagation of the EM wave through the phantom is determined according to Equation (3.3), based on its dielectric permittivity depending on the frequency.

Even in this case, for Test4, Test5 and Test6 it is worth noticing the fact that the overall quality of the reconstructed images improves when increasing the central frequency and the bandwidth of the simulation. Moreover, the use of F-DMAS clearly determines an effective suppression of sidelobes and artifacts, leading to clearer distinction between different objects. An analysis has been conducted as well to evaluate the beam patterns, to assess whether the F-DMAS beamformer offered a better lateral resolution compared to DAS. For this reason, the amplitude of the image transversal sections corresponding to the image line where the target was positioned has been investigated (Figure 3.17).

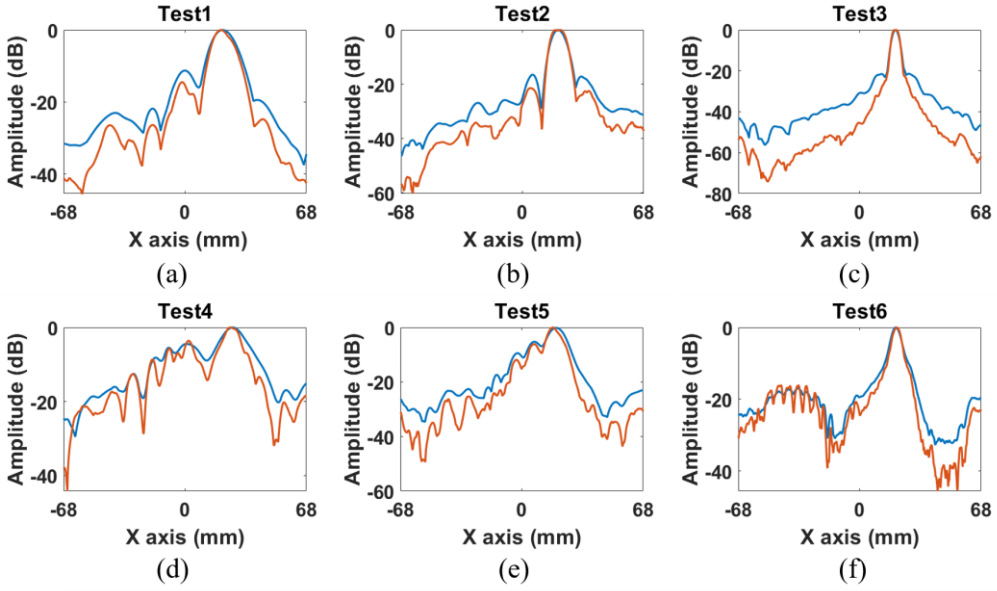

Figure 3. 17: Amplitude of the image section corresponding to depth where the target is positioned ($z = d_{target}$). Images above (a, b and c) are related to the tests conducted in air, while those below (d, e and f) are related to the tests involving a phantom. Blue curves refer to DAS, while the red ones represent F-DMAS.

From a qualitative point of view, Figure 3.17 allows to observe that F-DMAS (i.e., red traces) clearly succeeded in the improvement of lateral resolution: in

every case the main lobe is narrower and the sidelobes are partially suppressed. Moreover, Table 3.2 offers a quantitative insight on the lateral mainlobe width of the numerical tests at -6 dB (i.e., lateral resolution) and at -12 dB. As can be noticed from the values reported in the table, F-DMAS in all the considered cases shows a better lateral resolution at -6 dB of the beam patterns, resulting in an average improvement of 13%, both when the reconstructed target is in air (Test1, Test2 and Test3) and when it is embedded in a numerical fat-like phantom (Test4, Test5 and Test6). The same considerations can be done for what concerns the mainlobe width along the lateral direction measured at -12 dB, where F-DMAS offers an average improvement of nearly 15%. In one of the cases (i.e., Test4) the value of this measurement couldn't be defined, due to the presence of high sidelobes in the DAS traces even at the -6 dB level (as reported in Figure 3.17 (d)).

Table 3. 2: Evaluation of lateral mainlobe width of the two beamforming algorithms at -6 dB and -12 dB.

	Beamforming method	**Mainlobe width (mm)**	
		-6 dB	**-12 dB**
Test1	**DAS**	12.8	18.0
	F-DMAS	11.3	15.4
Test2	**DAS**	7.9	10.3
	F-DMAS	7.9	10.1
Test3	**DAS**	3.8	5.3
	F-DMAS	3.7	5.0
Test4	**DAS**	15.4	-
	F-DMAS	10.5	17.8
Test5	**DAS**	10.1	26.1
	F-DMAS	8.2	18.2
Test6	**DAS**	6.3	12.5
	F-DMAS	5.4	10.2

Additionally, it is worth noticing that the interface between air and phantom is not clearly reconstructed in all the cases, as expected using a speed different from c (the path from the antennas to the interface and back is entirely on air, thus when the reconstruction uses a speed different from c, because of the need of correctly imaging the portion within the phantom, the scattering from the interface is not properly focused in the DAS or F-DMAS routines). Finally, for Test4 and Test5 a displacement of the reconstructed target is observed. The position of the target suffers from an error of 2 mm and 4 mm along the Z axis, respectively for Test4 and Test5, with respect to the expected location. Such inaccuracies are expected, as the two-media propagation is prone to small

misalignments that can be traced back to the Snell's Law, whose compensation is out of the scope of the current implementation of DAS or F-DMAS routines.

3.3.3. Application in an experimental scenario

After the numerical evaluation described in the previous section, some experimental investigations have been performed within the proposed imaging system. To do this, as already explained, two linear actuators were mounted on the top rods of the aluminum frame. A synthetic linear array of 24 antennas has been employed, which was achieved by shifting automatically the two antennas along a fixed path defined by the actuators. This approach allowed for the acquisition of a scattering matrix for 2D image reconstruction. The experimental measurements have been carried out at millimeter wave frequencies (i.e., in the 18-40 GHz frequency range, in K/Ka-band). Before processing the collected signals for image reconstruction through DAS and F-DMAS, a proper calibration of the data is needed. This step is required since, in this experimental configuration, as mentioned earlier, the close proximity of the radiators creates significant mutual coupling (i.e., crosstalk), which hides the contribution of the weak but useful signals reflected by the illuminated field of view. The crosstalk signal can be easily removed by subtracting the measurement taken without the target (i.e., studying the propagation of the signals in air) from the one carried out with the target. This process allows for the successful removal of both antenna coupling and multiple reflections from the experimental environment. Additionally, since both amplitude and phase information are used in DAS/F-DMAS to reconstruct the final image, it is crucial to accurately calibrate the phase of the received signals. The phase can be affected by various factors, such as propagation through waveguides, transitions, and spurious backscattering. To address this issue, a known calibration target, typically a metallic plate, is adopted (as already done in the previous sections to characterize the operational limits of the imaging system). This plate represents a good standard since its backscattering matrix is analytically known, and its phase delay is directly related to its distance from the antennas.

The complete calibration process has been performed through the following steps, according to [42], [131]: a first measurement (M_{plate}) is taken with the metallic plate in place within the system at a known distance in front of the antenna array, and the corresponding scattering matrix is calibrated by subtracting the crosstalk (i.e., measurement with the plate minus measurement without the plate (M_{air})). The delay matrix corresponding to an ideal metallic plate at the same distance is then analytically calculated ($M_{analytics}$); the elements of this matrix are complex numbers defined by $e^{-j2\pi f\tau}$, where f is the frequency, and τ is the time delay. The calibration of the entire imaging system, including cables, transitions, and antennas, is achieved by means of the ratio of these two matrices.

Finally, the measurement acquired with the desired target to be imaged (M_{target}), after crosstalk calibration, is multiplied by this correction matrix, and the result is used in the image reconstruction process. The complete calibration procedure (M_{obj}) is summarized by the following formula:

$$M_{obj} = M_{analytics} * (M_{target} - M_{air})/(M_{plate} - M_{air}) \quad (3.13)$$

The obtained calibrated signals were fed to both the DAS an F-DMAS beamforming algorithms whose transmission parameters have been previously optimized (i.e., standard Gaussian pulse type, adaptive pulse width depending on the bandwidth according to (3.6), sine modulation type). Preliminary acquisitions have been performed on a low-losses phantom made by polysorbate (ε' = 3.65 and ε'' = 0.085 at 30 GHz). A metallic inclusion with 4 mm radius has been embedded into the phantom. The first interface (i.e., air-phantom) was placed at 5 cm from the antenna apertures ($d_{interface}$) and the distance between the first interface and the target was 2.3 cm, resulting in a target positioned at 7.3 cm (d_{target}) far from the antenna apertures. The target was aligned to the center of the array (x_{target} = 0 cm). The imaging scenario is shown in Figure 3.18.

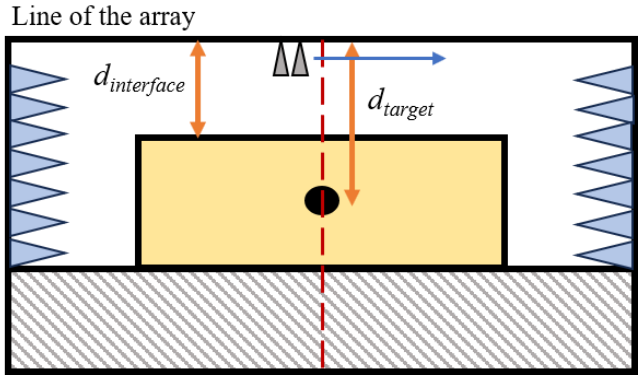

Figure 3. 18: Schema of the experimental scenario with phantom in place.

The results of this experimental imaging test are reported in Figure 3.19. Also in this case, the initial guess of the speed of propagation has been chosen as the weighted average between the speeds of propagation of the media involved in the scenario, resulting in errors in positioning the interface between air and phantom. As can be noticed from the obtained reconstructions, the metallic target is revealed and located. To better visualize the reconstructed target, the following figure shows only the experimental scenario beyond the first encountered interface between air and the polysorbate phantom. The reconstructed image via DAS suffers from an error of nearly 2 mm in positioning the target. Moreover, the reconstructed target presents discontinuities maybe due to phenomena of destructive interference. As already highlighted for the numerical tests in the previous section, instead, the F-DMAS beamforming method proved better

performance in terms of amplitude of the reconstructed signals and resolution of the overall image (Figure 3.19 (b)). From this figure, it can be noticed that the target is well reconstructed: compared to DAS, F-DMAS proved to succeed in recovering the shape and the actual dimension of the target.

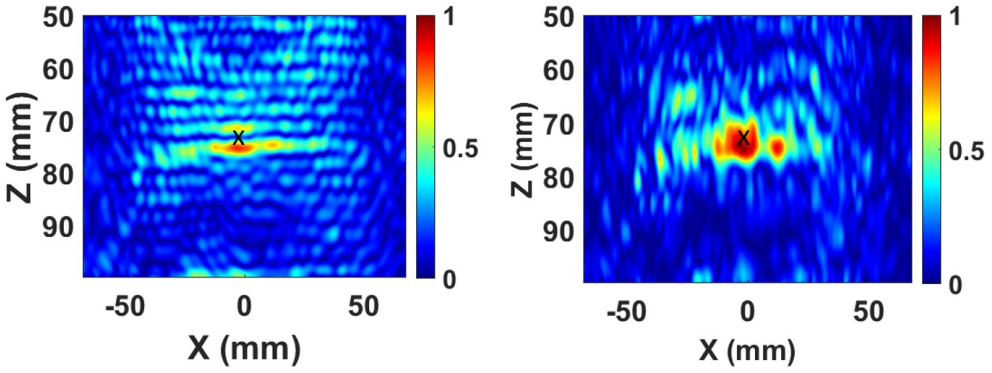

Figure 3. 19: Experimental reconstructions of the scenario through DAS (a) and F-DMAS (b) algorithms. The black crosses indicate the expected location of the target.

3.4. Discussion and conclusion

This Chapter has provided an in-depth analysis on the feasibility of a novel microwave/millimeter-wave imaging system for early breast cancer detection. The proposed system introduced the main novelty of offering an operational frequency range covering a large part of the electromagnetic spectrum, from 8 to 40 GHz. Several aspects regarding both the hardware realization and the software functionalities have been investigated and optimized, in a perspective to study the signals propagating within the system as well as to reconstruct diagnostic images from the acquired data. Particularly, the first part of this study focused on the design of a proper signal acquisition protocol. The study of the system has been conducted in three different frequency bands (X-band, Ku-band and K/Ka-band). To do such analyses, the system has been equipped with a single couple of antennas which were placed on the top of it. For each of the acquisitions, the scattering matrix has been collected and analyzed. The preliminary results of this investigation allowed to set the acquisition and calibration frequency band in a broad frequency range from 10 MHz to 44 GHz (i.e., the whole operating frequency of the VNA) since the conducted tests demonstrated that a specific limited calibration band for each of all the three investigated bands for acquisitions did not show improved performance. Thus, a single calibration for a complete measurements session, encompassing the three couples of antennas, is possible reaching reliable results in terms of acquired radar traces. Consequently, the optimum number of acquired points for each trace

has been analyzed proving that 4001 points are enough to satisfy the sampling theorem for all the frequency bands of interest, at the same time providing sufficiently detailed radar signals. This operation allowed to achieve a time step of 0.01 ns, ensuring a reliable representation of the system in the time domain for all the frequency bands of interest.

The optimum value of the Intermediate Frequency (IF) has been investigated as well, which has been set at 100 kHz as a trade-off between the acquisition time and the sensitivity to the noise, whose effects are mostly visible out of the operating frequency bands.

The hardware investigations concerned mostly the influence on the acquired signals given by the aluminum structure and the anechoic panels arrangement. The optimum setting for acquisition, ensuring accurate collection of radar signals, was found to be with the antennas located in central position against the aluminum frame and the anechoic panels in circular configuration. All the proposed analyses at the three different frequency bands have been conducted in such scenario.

After characterizing these aspects of the system, the crosstalk evaluation has been performed. Analyzing such signal is crucial both for what concerns signals collection and image reconstruction. Particularly, the crosstalk refers to unwanted interference and disturbance given by the signal propagating between the transmitting and the receiving antennas, whose effects may hide more important components of the collected radar signals. In this thesis, the crosstalk evaluation has been conducted by performing measurements without any target in place, in such a way to highlight the reflection phenomena of interest without the influence of any other scattering sources. Thus, quantifying this aspect of the system is mandatory even for imaging purposes. Indeed, image data need to be calibrated by subtracting the crosstalk from the acquisition performed with the object to be imaged (i.e., in this case, phantom) in place.

The limitations related to the visibility of a target (i.e., metallic plate and fat-like phantom) within the proposed microwave/millimeter-wave imaging system were then analyzed. Multiple measurements have been conducted by varying the distance of a metallic plate from the antenna apertures, showing that the system is effective in revealing the presence of such target up to the maximum achievable distance given by the physical dimensions of the system. These measurements, moreover, showed consistency in terms of detected crosstalk component. Indeed, this analysis proved the time independence of the crosstalk phenomenon, which is correctly quantified regardless of the distance of the target. Additionally, the proposed system showed its ability to accurately identify the target, even in the worst-case scenario (i.e., with the target placed as far as possible from the antenna apertures according to the dimensions of the system) preserving nearly 15 dB power margin against the background noise at 30 GHz.

Further analyses have been performed to investigate the effect of the insertion of phantoms of different thickness within the system. The study tested homogeneous fat-like phantoms (i.e., G3.3O66.6) with thickness

ranging from 1 to 3 cm to validate the measurement protocol. Phantoms were placed at a fixed distance from the antennas, above a metallic plate, and the peaks of the radar traces were analyzed. While the location of the peaks related to the crosstalk and the first encountered interface (i.e., air-phantom) remained constant among different acquisitions, the position of the peak related to the second interface (i.e., phantom-metallic plate) varied with phantom thickness due to the slower speed of electromagnetic waves through the phantom material, which mimics human fat.

An analysis of the power differences between the peaks showed that as phantom thickness increased, losses occurred and more energy was absorbed by the material. This helps in determining the maximum phantom thickness that can be used while remaining within power limits.

The second part of this work focused on the testing of the proposed imaging prototype in reconstructing images for diagnostic purposes in both simulated and experimental environments, using phantoms of different sizes and compositions. Experimental acquisitions required the equipment of the system with two micro-step linear actuators enabling controlled movement of the antennas and creating a synthetic linear array of 24 antennas for K/Ka-band acquisitions. The Delay and Sum (DAS) and the Filtered-Delay Multiply and Sum (F-DMAS), imaging algorithms have been employed to process and reconstruct the collected simulated and experimental signals. Some parameters of the transmitted signal have been optimized to obtain images as accurately as possible. In particular, the standard type of Gaussian pulse with sine-type modulation has been chosen. The pulse width has been set adaptively according to the employed frequency band adopted for each analysis, depending on the bandwidth of the three frequency bands of interest.

The numerical results showed that the DAS and F-DMAS imaging algorithms performed well when reconstructing images of a point target immersed in air, with better resolution using K/Ka-band antennas due to their higher frequency and wider bandwidth. F-DMAS improved image quality, in all the considered cases, by suppressing artifacts and enhancing fine details. Similar results were observed when the point target was embedded in a fat-like phantom, even though an initial speed of propagation estimate was required. In particular, the initial guess of the speed of propagation has been set equal to the weighted average of the media included in each scenario.

The experimental investigations, instead, have been conducted over the K/Ka-band since the initial objective of the whole work was to design a system working in the millimeter-wave frequencies. A fat-like phantom made by polysorbate with an embedded metallic target has been employed. The final reconstructions both via DAS and F-DMAS showed good performance in reconstructing the considered scenario even though an error of 2 mm at most has been observed in locating the target for DAS. The same considerations on the performance of the adopted imaging algorithms can be done as for the numerical reconstructions, with F-DMAS showing improved

recovering of shape and dimension of the target and slightly better image quality especially in terms of resolution and artifacts removal.

Further developments of the proposed work in this Chapter include firstly the experimental testing of the system in reconstructing images even at microwave frequencies (i.e., in X- and Ku-band). Such tests should pave the way to further analyses involving even phantoms with more complex geometry (multi-layered and/or conformal), as the ones presented in Chapter 2.

Moreover, other imaging approaches for the reconstruction of the acquired signals in both numerical and experimental scenarios can be adopted, both in terms of beamforming algorithms for radar-based imaging and different approaches like tomography.

Chapter 4

Optimization of a tomographic imaging algorithm for bone health monitoring

4.1. Introduction

In this Chapter, a different microwave imaging approach will be introduced and discussed. Specifically, this part of the work refers to a collaboration with the Translational Medical Device Lab, at the University of Galway, in Ireland. So far, the thesis focused on the development and testing of breast phantoms for microwave/millimeter-wave radar-based imaging. As explained previously, radar imaging allows for the detection of a specific target (i.e., in the case of this thesis, breast masses) based on the dielectric contrast among the investigated media. Microwave tomography (MWT), instead, can provide even quantitative information about the object of interest, which is of paramount importance in medical diagnostic. Particularly, MWT is able to produce two- and three-dimensional (2D and 3D) images where the value of each pixel is determined by the retrieved dielectric properties of the object of interest [3], [29]. To do this, each antenna of the system architecture transmits a continuous wave (CW), which can be a single- or multi-frequency electromagnetic signal. Due to the differences between the dielectric properties of the different media encountered along the path, scattering phenomena occur and the reflected electromagnetic fields are measured by the receiving antennas. The images of the resulting dielectric properties are then reconstructed using the recorded signals as input for specialized imaging algorithms. This technique allows for the detection of a designated target and the estimation of its position, but also for the quantitative recovery of its properties.

As reported previously, when performing early breast cancer detection, the main aim is that of assessing the presence of tumors. At the early stages of this pathology, clinicians are interested in distinguishing, by conducting screening campaigns, healthy and diseased conditions. This means differentiating clinical cases with and without the presence of a tumor. Only later more sophisticated clinical investigations (such as US imaging or MRI) will be carried out on patients.

In this framework, MWT systems have several disadvantages compared to radar-based technologies, being computationally more expensive and limited in resolution. On the other hand, different pathologies affecting different anatomical locations of the human body, may require different approaches. Indeed, MWT has emerged as a promising diagnostic imaging technique for different clinical applications, being already explored, beyond breast cancer detection [42], [61], [62], [63], [65], [132], [133], in brain stroke diagnosis [53], [54], [55], cardiac imaging [56] and bone health assessment. Studies have demonstrated a significant dielectric contrast between healthy and diseased human trabecular bones, which suggests that MWT has the potential to detect changes associated with bone disorders [134]. This Chapter, indeed, will analyze the employment of a MWT imaging algorithm for the reconstruction of 2D images of heterogeneous anthropomorphic bone phantoms in both numerical and experimental scenarios. Particularly, the calcaneus bone has been considered for the whole project, since its anatomic peripheral location within the human body makes it suitable for MWI application, in a perspective to do such investigation on real patients.

Recent studies have explored the possibility of using MWI in monitoring bone health by investigating the dielectric contrast between normal and diseased human bone tissues [57], [58], [134]. Indeed, in [60] the authors reported an average percentage difference between the dielectric properties of the skin and trabecular bone of 70%, while the average percentage difference between the properties of trabecular bone and cortical bone is 48%, in the frequency range of 0.5–5 GHz.

Among the bone diseases, osteoporosis and osteoarthritis are two common conditions that significantly impact the skeletal system and overall bone health. Osteoporosis, characterized by low bone mass and deterioration of bone tissue, is a major contributor to fractures, especially among the elderly [135]. It is reported that every year almost 8.9 million fractures occur due to osteoporosis worldwide [25]. Conversely, osteoarthritis, a degenerative joint disease, primarily affects the cartilage that cushions the ends of bones in joints [134]. Both pathologies often lead to changes in the microarchitecture of the human trabecular bones.

Actually, in current clinical practice, Dual-energy X-ray Absorptiometry (DXA) is commonly used to monitor the health of human bones, which allows for direct quantitative measurement of bone mineral density (BMD) [57]. However, this method poses long-term risks for patients due to exposure to ionizing radiation. Moreover, this technology does not infer

precise information about the quality of the investigated bone, in terms of structural features and composition [25]. Additionally, Quantitative Computed Tomography, while less used compared to DXA, is limited in its use due to equipment and testing costs [6]. While these traditional clinical approaches provide high-resolution images for bone health assessment, MWT offers distinct advantages, including the use of non-ionizing radiations, portability, and cost-effectiveness, making it a viable contender for bone health monitoring [6], [57]. Among those, it has been shown to resolve various bone structures such as cortical and trabecular bone tissues to a resolution that allows for detecting contrast between diseased and healthy bones. Moreover, another good advantage of microwave bone imaging is that of the independence of motion artifacts from patients' breathing or heartbeat, which is only a minor limitation given the peripheral location of the target organ within the human body.

Studies have reported that the variation in the degree of mineralization of the bones affects their dielectric properties [57], [134], [136]. In this context, the development of a novel device based on MWT, which requires precisely quantifying the dielectric properties of the bone tissues, may help in the diagnosis of the above-mentioned pathologies.

MWT, as a specialized approach of MWI, allows for the estimation of the spatial distribution of the dielectric properties of the human biological tissues (i.e., the relative permittivity (ε_r) and conductivity (σ_s (S/m))). This involves solving the inverse scattering problem by analyzing measured scattered EM field data [22]. The EM inverse scattering problem is essentially ill-posed and non-linear and to address this challenge, various EM inverse scattering methods including conjugate gradient techniques [45], [46] and Gauss-Newton (GN) optimization algorithms [47], [48] have been developed.

A well-known conventional technique using a forward solver, i.e., the Distorted Born Iterative Method (DBIM), was instead considered in this project. This method is based on the approximation of the non-linear inverse scattering problem with an underdetermined set of linear equations [137]. In particular, it is an extended version of the Born and Rytov approximation, which fails in reconstructing a 2D scene in the presence of high contrast between the objects involved in the imaging scenario [50]. This technique does not involve the update of the Green's function at each iteration [138], [139], which could introduce a limitation since the considered scene is meant to deal with biological scenarios where the investigated properties are unpredictable and the dielectric contrast might be high. Within the DBIM method, instead, Green's function is updated at every algorithm iteration. The set of linear equations was solved by using an Iterative Method with Adaptive Thresholding for Compressed Sensing (IMATCS) during each DBIM iteration. Additionally, as the IMATCS algorithm might become unstable due to its inherent approximation, the L_2-regularization strategy proposed by [137] was employed. Indeed, the algorithm employed in [50] was revealed to be successful in reconstructing a simplistic phantom. In

particular, in [50], a numerical two-layer bone phantom with a circular shape has been adopted, which does not represent a realistic anthropomorphic scenario.

Previous studies have considered bone as a homogenous single tissue, neglecting the difference between cortical and trabecular bone properties [57], [59]. As a matter of fact, within the literature, there is a limited number of works concerning the dielectric properties characterization of the human trabecular bone [140]. The few available studies have reported insufficient data on *in-vivo* human properties. In [57], the authors investigated the *in-vivo* dielectric properties of the human bones of two patients with leg injuries in the frequency range of 900-1700 MHz. Another work has reported the *in-vitro* dielectric properties of porcine bone samples at 1100 MHz [136]. Moreover, in the same study, good reconstructions of bone phantoms have been reported at 1 GHz. Even in the present work, the numerical reconstructions of the proposed calcaneus phantoms were achieved at this frequency, since it represents a good trade-off between the penetration depth and the image resolution [29], [60], [141].

On the other hand, a small number of attempts to reproduce numerical phantoms with realistic structures have been reported, especially in the field of breast and bone microwave tomography [142], [143], [144], [145], [146]. In [142], three anatomically realistic phantoms of the human leg have been employed, where the models were generated from magnetic resonance imaging (MRI) images. This feasibility study aimed to optimize the use of an MWT algorithm by investigating the influence of certain parameters (i.e., the kind of matching medium, the number of antennas and the thickness of the various biological layers) on the numerical reconstructions.

Since in a realistic clinical scenario, the object to be imaged (i.e., the human calcaneus and the bones overall) is layered and not geometrically regular, this work, for the first time, aims to reconstruct the dielectric properties of more realistic (anthropomorphic) phantoms, including both numerical and experimental models, through the DBIM/IMATCS algorithm previously proposed in [50]. In the present study, the phantoms were designed as multi-layered calcaneus-shaped structures. The geometry of such phantoms has been derived from MRI images. Thus, the proposed phantoms reproduce in shape and dimension the actual human calcaneus, mimicking a realistic clinical scenario.

The first investigation included a numerical analysis where the algorithm was tested in two different scenarios: the former adopted a circular antenna configuration, as in [50], with 16 equally-spaced antennas placed around the phantom; in the second scenario, instead, 24 antennas were placed around the phantom along a calcaneus-shaped array. After assessing the potential of the imaging algorithm in reconstructing two-layer (i.e., cortical + trabecular layer) healthy and diseased phantoms, a further analysis has been performed by including a thin layer of skin surrounding the numerical anthropomorphic phantom, reaching good reconstructions of the target properties even in a

more complex scenario [147]. As mentioned before, the reconstructions were achieved at 1 GHz.

Subsequently, the same imaging method has been employed for reconstructing 3D experimental multi-layer phantoms, for the first time having a conformal shape and compatible dimension with the human calcaneus. Different liquid and solid tissue-mimicking materials (TMMs) have been developed for this purpose, aiming at reproducing the properties of healthy, osteoporotic and osteoarthritic bone. The adopted imaging prototype involved nine microstrip antennas which were supposed to be put in contact with the model without any matching medium. Even a layer of fat tissue-like phantom has been considered in the proposed model, making the scenario as realistic as possible. In this case, the reconstruction frequency was set to nearly 3 GHz depending on the kind of phantom, since the involved antennas were designed to resonate at that frequency [25], [61].

The main contributions of this project are the following. Firstly, novel multi-layered calcaneus-shaped structures have been numerically designed and experimentally developed, specifically catered to represent the calcaneus in a clinical imaging scenario. This design considers the complex anatomical features of the calcaneus, incorporating different layers mimicking the dielectric properties of the human bone tissues. Secondly, the whole investigation evaluates the effectiveness of DBIM in reconstructing such realistic asymmetrical structures, both from a numerical and an experimental point of view.

The findings of the proposed analyses have shown that this method is even suitable for the reconstruction of a complex scenario, with an irregular geometry phantom and an irregular antenna array. As outlined in the next sections, the proposed phantoms and imaging algorithms demonstrated to be successful in reproducing various realistic scenarios where it was possible to distinguish the mimicked medical conditions of the bone (healthy, osteoporotic or osteoarthritic) based on the reconstructed dielectric properties.

4.2. Overview of the proposed method

4.2.1. DBIM approach

As mentioned before, MWT technologies involve solving an inverse scattering problem to retrieve an image showing the dielectric profiles of the scenario under test. This EM inverse scattering problem, however, is inherently ill-posed (i.e., there are fewer measurements compared to unknowns) and non-linear. The non-linearity arises from the heterogeneity of the target [48] and necessitates non-linear methods for estimating the dielectric properties using the scattered field within the desired frequency range.

A graphical description of the imaging scenario is given in Figure 4.1. The imaging domain volume (V) is illuminated by an EM field from a known EM source. This approach aims to reconstruct the unknown complex dielectric permittivity of the object to be imaged (Ω) starting from measurements related to one or more observation points outside V.

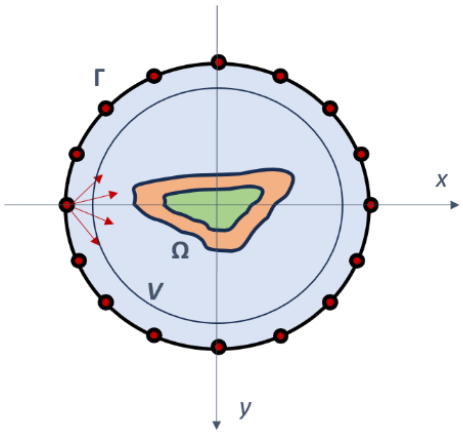

Figure 4. 1: MWI Scenario. Γ represents the array with the EM sources (here the circular configuration is shown), V is the imaging domain volume while Ω is the object to be imaged.

In this work, the DBIM approximation has been employed to linearize the EM scattering wave equation by replacing the total EM field (i.e., E_{total}) with the known incident field (i.e., E_{inc}), which is estimated at each iteration of the algorithm in the presence of a known background. The computation of the Green's function (i.e., $G_{background}$) is required too, which can be recovered by a forward solution. The EM scattered field (i.e., E_{scat}) at measurement point r and angular frequency ω can be expressed as:

$$E_{scat}(r,\omega) = E_{total}(r,\omega) - E_{inc}(r,\omega) \quad (4.1)$$

$$= \omega^2 \mu \int_V G_{background}(r,r',\omega)\, C_f(r',\omega) E_{total}(r',\omega) dr' \quad (4.2)$$

where V represents the volume and C_f is the contrast function. The EM scattered equations obtained from this computation are then inverted to get an approximate solution of the contrast between the target region and the current estimation of the background profile (inverse solution) [50]. The main principle of the DBIM method relies on updating the background dielectric profile by alternating forward and inverse solutions until reaching convergence [48].

4.2.2. IMATCS algorithm

In EM inverse scattering problems, accurately manipulating the measurements matrix is crucial for recovering the underlying signals. However, this process is not straightforward [137]. A matrix transformation is required at each DBIM iteration for the unknown complex permittivity vector to make it sparse. The IMATCS algorithm is employed to find the inverse solution. As a thresholding approach, it is based on a-priori information, which could be unavailable in many medical applications. Therefore, it relies on adaptive thresholding, where the threshold value is decreased exponentially at each DBIM iteration [25]. The IMATCS algorithm solves the contrast function based on a set of measurements, as displayed below:

$$y = Ax \tag{4.3}$$

where y is the residual measurement data vector, A is the measurement matrix (with dimensions m × n (m < n),), which relies on E_{inc} and $G_{background}$ from (4.1)-(4.2) and it is updated at each DBIM iteration, and x is the unknown dielectric contrast function. The problem displayed in (4) is then solved as follows:

$$\min_x ||y - Ax||_2^2 + \xi||x||_0 \tag{4.4}$$

where the solution, applying the adaptive IMATCS method, can be expressed as:

$$x_{j+1} = T_0 e^{-ti}(x_j + \xi A^*(y - Ax_j)) \tag{4.5}$$

where A^* is the conjugate transpose of A, ξ refers to the convergence of the method, T_0 is the initial threshold value, x_j is the unknown vector, t is the threshold step size and j is the iteration number. The initial value of the algorithm displayed in (4.5) is null (i.e., $x_0 = 0$). The following values of x_j are retrieved after an optimal number of IMATCS iterations. This method allows for the recovery of the unknown x_j without a-priori information about the signal.

However, the relationships among the measured and the unknown data are non-linear and approximated as linear in this specific application, which may result in instability and divergence of the IMATCS algorithm [50]. To ensure a more stable recovery of the contrast function during each iteration of IMATCS, an L_2-regularized L_0-minimization approach is adopted, as suggested in a previous study [31]. Thus, the problem shown in (4.4) can be expressed as:

$$\min_x ||y - Ax||_2^2 + \xi_1||x||_0 + \xi_2||x||_2^2 \tag{4.6}$$

where the solution is given by:

$$x_{j+1} = (1 + \xi_2)^{-1} T_0 e^{-ti}\left(x_j + \xi_1 A^*\left(y - Ax_j\right)\right) \tag{4.7}$$

This kind of minimization/regularization approach is strongly influenced by the choice of the threshold value which may not lead to convergence. Nonetheless, it ensures a more stable and robust recovery of the unknown variables x_j.

4.2.3. Parameters selection

As previously stated, selecting appropriate regularization parameters is crucial to achieving the optimal solution for the unknown contrast function. At this stage, it is fundamental to properly set the ξ_1 and ξ_2 convergence parameters, as well as the initial threshold value T_0, the threshold step size t and the maximum number of iterations of the IMATCS algorithm. In particular, since ξ_1 should satisfy the following condition:

$$0 < \xi_1 < {}^{2}/_{\Upsilon_{max}(AA^*)} \tag{4.8}$$

where $\Upsilon_{max}(AA^*)$ represents the maximum of the eigenvalues of the product AA^*, it has been chosen as:

$$\xi_1 = 1.9/\Upsilon_{max}(AA^*) \tag{4.9}$$

The other convergence parameter ξ_2 has been set equal to 0.005 for the reconstruction of all the numerical phantoms. The value of the initial threshold T_0, instead, was chosen empirically for each of the simulations depending on the dielectric properties of the employed phantom, the physical antenna configuration (i.e., circular or calcaneus-shaped array) and the kind of investigation (i.e., numerical or experimental). The overall value has been set ranging from 125-150 depending on the quality of the single reconstruction, for the numerical reconstructions. In experimental context, instead, the value of the optimum threshold was found to be 20-25 at most. The threshold step size t was set at 0.01, while the number of IMATCS iterations was set at 5 since this value has proved to be a good trade-off between the computational time and the performance of the overall algorithm.

4.2.4. Evaluation of the performance

To quantify the performance of the algorithm, two different metrics were computed. The first one, the Normalized Root Mean Square Error (NRMSE), is defined as:

$$NRMSE = ||\varepsilon_r(f) - \varepsilon_r^*(f)||_{L^2}^2 / ||\varepsilon_r(f)||_{L^2}^2 \tag{4.10}$$

where $\varepsilon_r(f)$ is the complex permittivity profile of reference bone dielectric properties, and $\varepsilon_r^*(f)$ is the complex permittivity profile of

reconstructed bone dielectric properties [46], [55], [143]. The other metric is the Structural Similarity Index (SSIM), which aims to estimate the structural similarity between the reconstructed and reference bone dielectric properties by comparing two images at a time, considering parameters including luminance and contrast [148]. These scalar metrics have been calculated separately for both the real and imaginary parts of the reference and reconstructed complex permittivity profiles of the phantoms.

4.3. Numerical bone phantoms investigation

4.3.1. Simulation testbed

The initial stage of the whole work involved developing and testing the proposed imaging method on numerical anthropomorphic calcaneus phantoms. Particularly, at first, a two-layer calcaneus-shaped model was developed and evaluated in a 2D imaging scenario. The outer layer of the model mimics the dielectric properties of the human cortical bone; the inner layer, instead, represents the human trabecular bone. Three different phantoms have been proposed; the outer layer was the same for all of them, while the inner layer was meant to mimic the properties of the normal healthy trabecular bone (phantom P1), the osteoporotic trabecular bone (phantom P2) and the osteoarthritic trabecular bone (phantom P3). In Table 4.1, the compositions of the phantoms are reported.

Table 4. 1: Numerical bone phantoms for simulations.

Phantom label	Outer layer	Inner layer
P1	Cortical bone	Normal trabecular bone
P2	Cortical bone	Osteoporotic trabecular bone
P3	Cortical bone	Osteoarthritic trabecular bone

The two-layer model was then transformed into a 2D EM model according to the single-pole Debye parameters for the two different tissues. The Debye model can be described as:

$$\varepsilon_r(\omega) = \varepsilon_\infty + \frac{\Delta\varepsilon}{1+j\omega\tau} + \frac{\sigma_s}{j\omega\varepsilon_0} \tag{4.11}$$

where ε_∞ is the permittivity value at the highest frequency considered, $\Delta\varepsilon$ is the difference between the permittivity value at the lowest and highest frequencies considered, σ_s is the conductivity and τ is the relaxation time constant (assumed to be spatially invariant with the value of 0.5 ps). Table 4.2 shows the parametric values of the Debye parameters for the considered tissues in the frequency range of 0.5-8.5 GHz [50].

The dielectric properties of normal cortical and trabecular bone tissue were obtained from [149] whereas, the Debye parameters for the

osteoporotic and osteoarthritic trabecular bones were set according to the dielectric properties reported in [134].

Imaging data were simulated using a Finite Difference Time Domain (FDTD) method with a resolution of 1 mm. As already proposed [46], [48], [136], [137], [143], the FDTD approach was used as a forward solver for the

Table 4. 2: Dielectric Properties of Bone Tissues.

Tissue	**Single-pole Debye Parameters**			**Dielectric properties @ 1 GHz**	
	ε_∞	$\Delta\varepsilon$	σ_s (S/m)	ε'	σ (S/m)
Cortical bone (CB)	8.75	4	0.01	12.39	0.0736
Normal trabecular bone (TB)	14	7	0.1	20.43	0.2125
Osteoporotic trabecular bone	16	3	0.12	18.73	0.1677
Osteoarthritic trabecular bone	24	5	0.1	28.55	0.1795

inversion procedure in this work. Phantoms were placed in a lossless non-dispersive matching medium ($\varepsilon_\infty = 2.848$, $\Delta\varepsilon = 1.104$, $\sigma_s = 0.005$ S/m). The same values have been assigned to the initial guess of the DBIM imaging algorithm. The simulated measurements were carried out through two different antenna configurations (i.e., circular and calcaneus-shaped array). Regarding the former (Figure 4.2 (a)), 16-point sources were equally spaced in a circular array around the two-layer phantoms. The latter, instead, involved 24-point sources, which were manually placed following the same shape as the bone model (Figure 4.2 (b)). The specific number of antennas used in both the array configurations (i.e., 16- and 24-point sources antennas respectively) have been chosen as a result of an investigation on the optimum configuration to image the proposed phantoms. We observed that these proposed configurations gave the best results in terms of qualitative reconstructions and quantitative performance metrics. The reconstructions in circular array configurations have been performed by using several antennas ranging from 9 to 16. For what concerns the calcaneus-shaped configuration, at least 18 antennas were needed to reconstruct the target, probably due to the more geometrically complex scenario. We finally chose 24 antennas even to compare our results with [142]. In both cases, the point sources sequentially illuminated the phantoms with a modulated wideband (i.e., 2 GHz) Gaussian pulse, with a central frequency of 1 GHz. Only one recorded EM signal for each transmit-receive antenna pair was considered for the reconstructions (i.e., N(N-1)/2 signals, where N stands for the number of point sources) for a total of 120 signals for the simulations related to the circular configuration and 276 signals for those related to the calcaneus-shaped configuration.

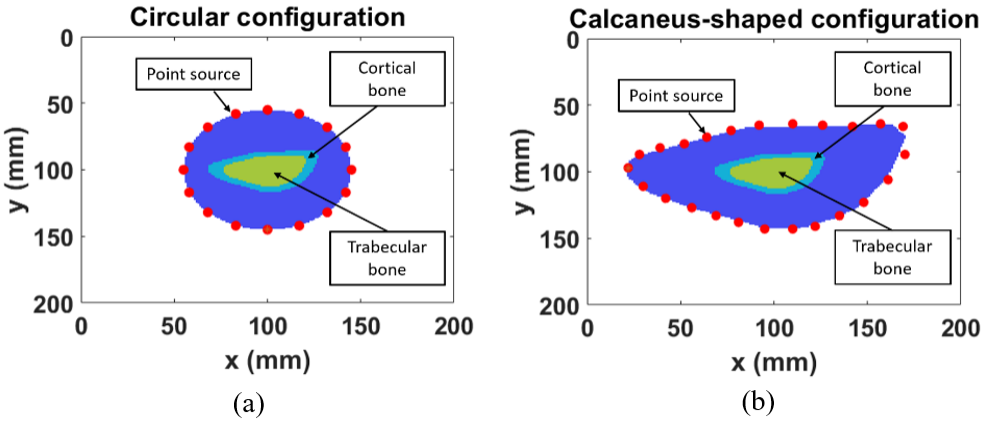

Figure 4. 2: Circular (a) and calcaneus-shaped (b) simulation testbeds.

4.3.2. Results and discussion

4.3.2.1. Numerical reconstruction of phantoms

This section presents the numerical results obtained by the L_2-IMATCS approach for bone dielectric properties' reconstruction using dielectrically informed numerical models. The reconstruction (along with the corresponding reference properties scenario) of phantoms P1 (Figure 4.3 and Figure 4.6), P2 (Figure 4.4 and Figure 4.7) and P3 (Figure 4.5 and Figure 4.8) through the described approach within the two different simulation testbeds (i.e., the circular and the calcaneus-shaped antenna configuration) are shown at 1 GHz. The choice of the frequency for image reconstruction was inspired by [60], where the authors investigated the optimum frequency band for bone imaging application considering calcaneus as the imaging scenario. The authors used a planar layered model of the calcaneus and demonstrated that the most appropriate frequency range for the bone imaging application is 0.6 - 1.9 GHz. Moreover, the authors demonstrated that the penetration depth of EM waves significantly reduced beyond 3 GHz, making it not feasible to distinguish the different tissues of the human calcaneus. Hence, frequencies less than 3 GHz should be considered when designing an MWI system for bone imaging applications [60]. This allows to obtain an overall penetration depth of nearly 5 cm, which is considered sufficient for this kind of application. The penetration depth is indeed inversely proportional to the dielectric permittivity of a biological tissues. The main issues, thus, are related to the penetration of the EM wave through skin and muscles, which have higher dielectric properties compared to the other tissues involved in the anatomical region of interest. Nonetheless, the external location within the body of the human calcaneus, its biological composition and dimension prove the feasibility of this analysis at microwave frequencies.

As previously described, the employed numerical phantoms have been designed as 2D calcaneus-shaped structures including two different layers. The dielectric properties of the cortical bone tissue have been assigned to the outer layer, while the inner layer was meant to mimic the trabecular bone tissue. The main difference among the three phantoms relies on the properties of the trabecular tissue, reproducing respectively a healthy (i.e., P1: normal trabecular bone) and a diseased scenario (i.e., P2: osteoporotic trabecular bone and P3: osteoarthritic trabecular bone). As shown in the figures, in each of the reconstructions, the target (i.e., the trabecular bone) is correctly positioned in the expected region (i.e., the red dotted line in the reconstructed images). Although the DBIM algorithm was allowed to perform 3 iterations, it was found to converge after one iteration. Therefore, the visual reconstruction results are reported for the first DBIM iteration.

As can be noticed from Figures 4.5 and 4.8, when dealing with phantom P3, the shape of the reconstructed object is conserved but the dimension is larger than the reference object. For what concerns the reconstructions of P1 and P2 the method seems to perform well both in terms of the reconstructed dielectric properties and geometric features.

This issue concerning the reconstruction of P3 could be related to the high value of the dielectric properties of the osteoarthritic trabecular bone. The best reconstructions were achieved for the P2 (i.e., osteoporotic) phantom. Indeed, the osteoporotic trabecular bone is the one with the lowest dielectric properties, suggesting that this approach works better in contexts with lower contrast between the properties of cortical and trabecular bones. However, the encountered limitation might be resolved by adaptively changing the threshold of the IMATCS algorithm and optimizing the parameters of the whole method.

The overall findings demonstrate that adopting an adaptive antenna configuration instead of a circular antenna array does not offer significant benefits as the DBIM with L_2-IMATCS algorithm can handle complex imaging scenarios regardless of the antenna configuration.

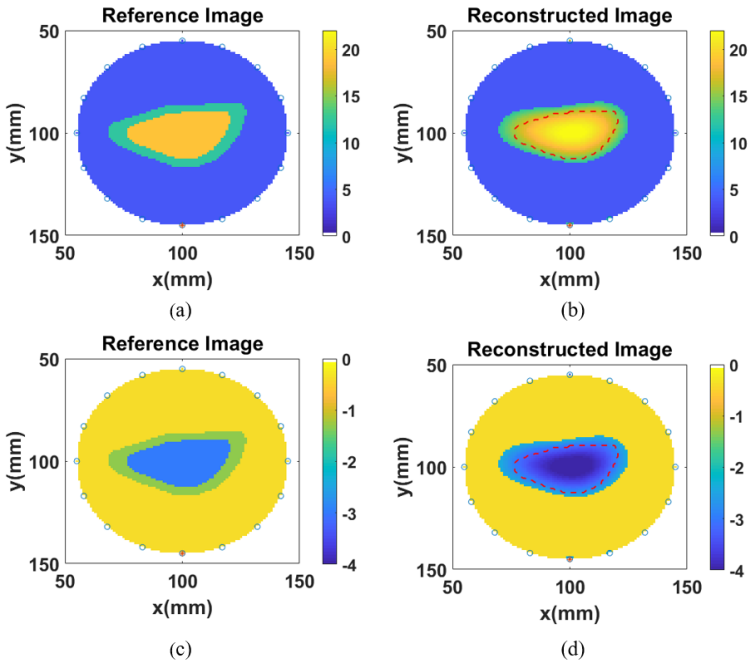

Figure 4. 3: Real and imaginary part ((a), (b) and (c), (d), respectively), of the complex dielectric permittivity of reference and reconstructed P1 (cortical + normal trabecular) bone phantom through the 16-antenna circular testbed. The dashed red curves in (b) and (d) represent the reference profiles.

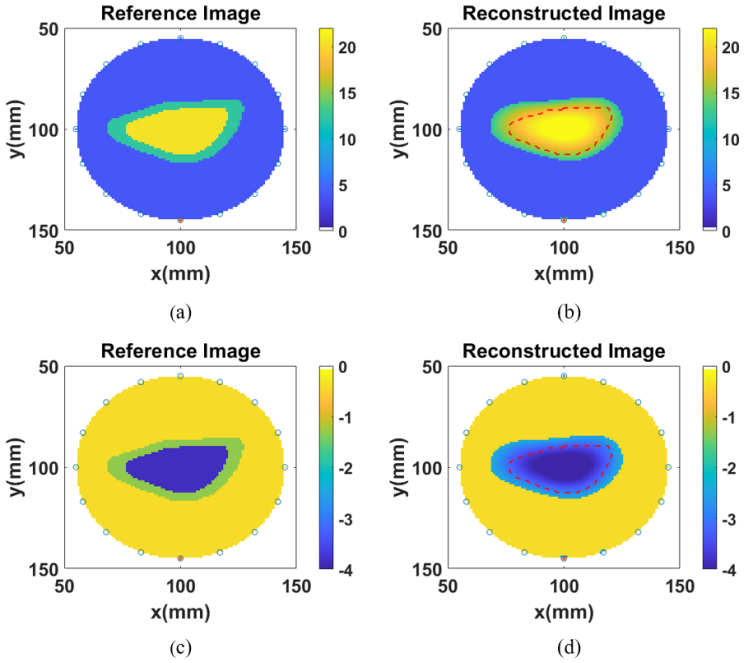

Figure 4. 4: Real and imaginary part ((a), (b) and (c), (d), respectively), of the complex dielectric permittivity of reference and reconstructed P2 (cortical + osteoporotic trabecular) bone phantom through the 16-antenna circular testbed. The dashed red curves in (b) and (d) represent the reference profiles.

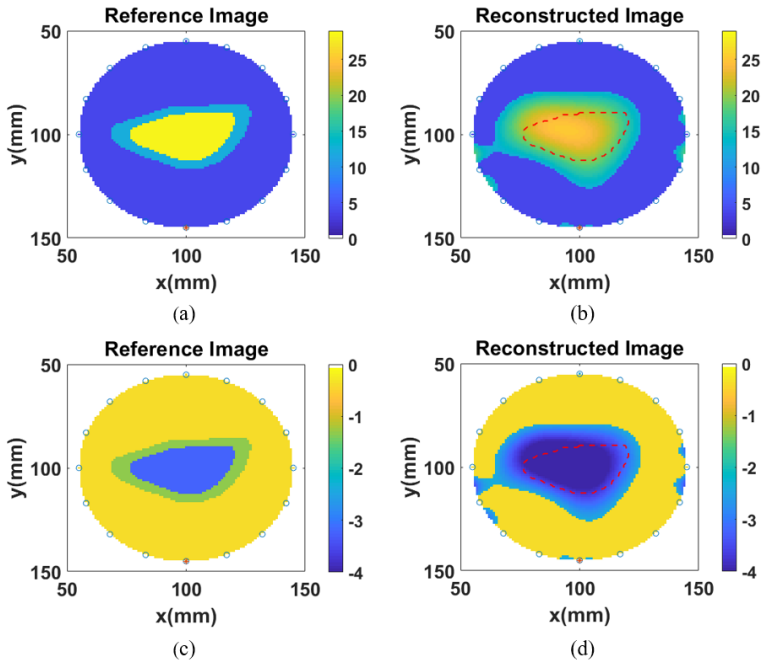

Figure 4. 5: Real and imaginary part ((a), (b) and (c), (d), respectively), of the complex dielectric permittivity of reference and reconstructed P3 (cortical + osteoarthritic trabecular) bone phantom through the 16-antenna circular testbed. The dashed red curves in (b) and (d) represent the reference profiles.

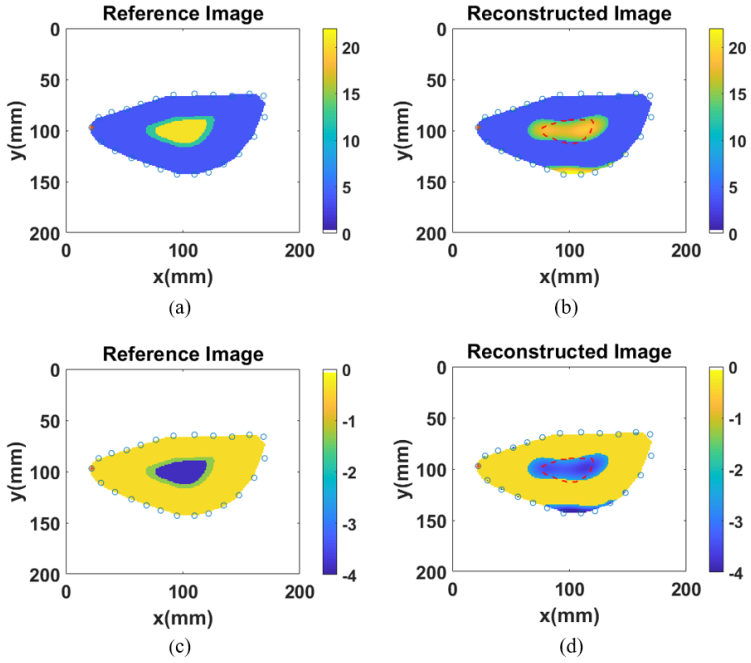

Figure 4. 6: The real and imaginary parts ((a), (b) and (c), (d), of the complex dielectric permittivity of reference and reconstructed P1 (cortical + normal trabecular) bone phantom through the 24-antenna calcaneus-shaped testbed. The dashed red curves in (b) and (d) represent the reference profiles.

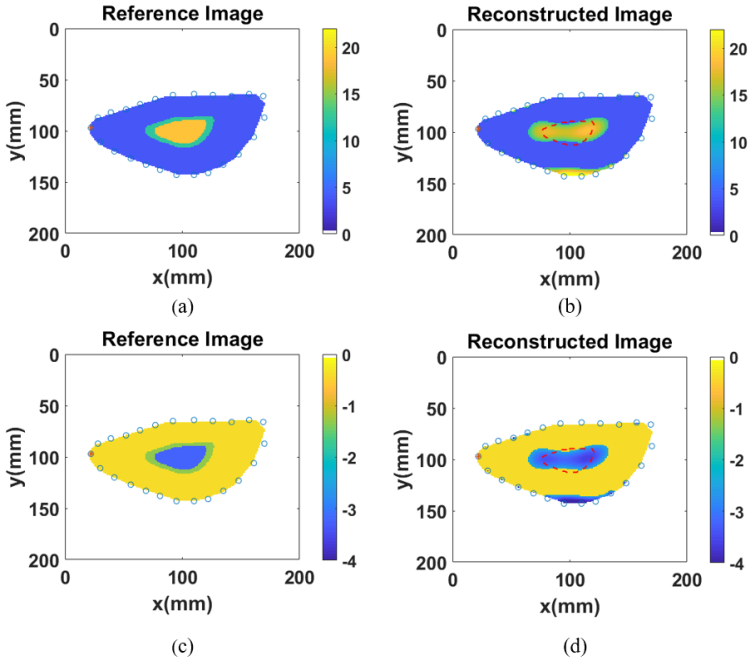

Figure 4. 7: The real and imaginary parts ((a), (b) and (c), (d), of the complex dielectric permittivity of reference and reconstructed P2 (cortical + osteoporotic trabecular) bone phantom through the 24-antenna calcaneus-shaped testbed. The dashed red curves in (b) and (d) represent the reference profiles.

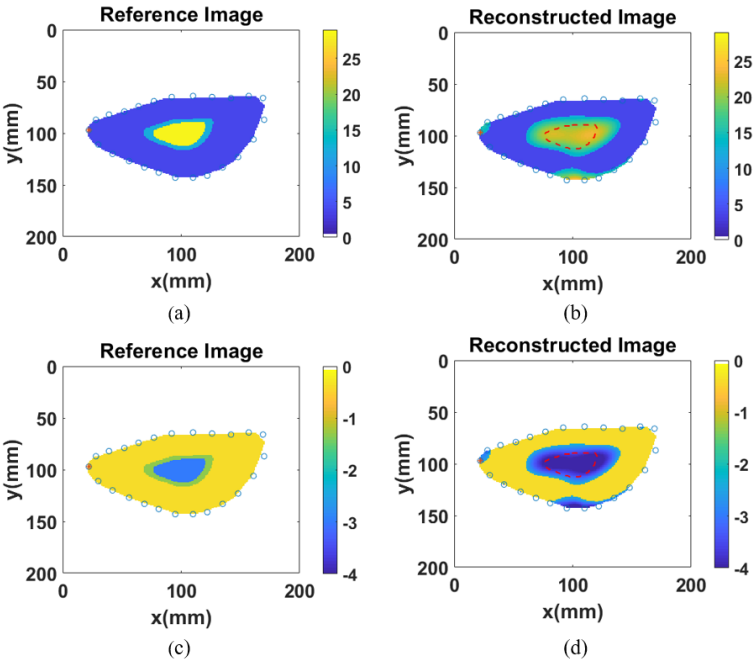

Figure 4. 8: The real and imaginary parts ((a), (b) and (c), (d), of the complex dielectric permittivity of reference and reconstructed P3 (cortical + osteoarthritic trabecular) bone phantom through the 24-antenna calcaneus-shaped testbed. The dashed red curves in (b) and (d) represent the reference profiles.

4.3.2.2. Quantitative metrics results

Two performance metrics (i.e., NRMSE and SSIM) have been calculated as previously described to assess the quantitative performance of the proposed DBIM/IMATCS imaging algorithm. Table 4.3 shows the results in terms of the mentioned metrics in a non-noisy environment. It is worth reporting that both these two metrics range from 0 to 1, indicating opposite results. The former refers to an error occurring between the reference and reconstructed images. Thus, NRMSE = 0 means 0% and NRMSE = 1 means 100% error over the pixels of the two images. Conversely, SSIM = 0 means 0% and SSIM = 1 means 100% similarity of the two images. The reported values suggest that the proposed method is suitable to properly reconstruct such complex-geometry scenarios with both the adopted antenna configurations, reaching comparable performance as in [50], where simpler versions of the phantoms proposed in this present work have been employed.

The NRMSE has been estimated by comparing the reference and reconstructed properties of the phantoms inside the whole imaging region V. This may explain the achieved values in terms of error, which are still acceptable considering the complex geometry of the phantoms. The SSIM, instead, has been calculated within the only trabecular target region. As can be noticed from Table 4.3, a slight decrease in the performance occurs in the cases related to the calcaneus-shaped antenna configuration, due to the complexity and the irregularity of the scenario.

Table 4. 3: NRMSE and SSIM between original and reconstructed phantoms without noise.

		Circular array			Calcaneus-shaped array		
		P1	**P2**	**P3**	**P1**	**P2**	**P3**
NRMSE	ε'	0.151	0.114	0.316	0.318	0.297	0.397
	ε''	0.313	0.357	0.497	0.376	0.286	0.402
SSIM	ε'	0.995	0.994	0.987	0.984	0.982	0.977
	ε''	0.998	0.998	0.997	0.994	0.993	0.991

4.3.2.3. Impact of SNR on the reconstructed properties

MWT is highly sensitive to both noise and artifacts due to the nature of the inverse problem to be solved. Noise from measurements and system imperfections can degrade image quality, while inverse problem artifacts and nonlinear effects can introduce significant artifacts. Effective management of these factors is crucial for achieving reliable and accurate reconstructions in MWT.

To make the conditions as realistic as possible, the measured data were corrupted by Additive Gaussian Noise (AWGN). Therefore, the performances in terms of NRMSE were also analyzed by varying the signal-to-noise ratio (SNR) from 20 dB to 60 dB, to cover a range of feasible values.

The results of this investigation are reported in Tables 4.4 and 4.5. The displayed NRMSE values suggest that the developed method performs well even in the case of low SNR values, where worse performance is expected. Thus, this analysis proved the robustness of the DBIM/IMATCS imaging algorithm in the presence of noise.

Table 4. 4: NRMSE between original and reconstructed bone phantoms for the real part of complex permittivity, by varying the noise level.

SNR (dB)	Circular array			Calcaneus-shaped array		
	P1	P2	P3	P1	P2	P3
20	0.172	0.145	0.359	0.363	0.300	0.370
30	0.153	0.112	0.405	0.345	0.298	0.367
40	0.149	0.122	0.372	0.377	0.328	0.394
50	0.176	0.121	0.392	0.317	0.297	0.371
60	0.160	0.126	0.399	0.331	0.297	0.372

Table 4. 5: NRMSE between original and reconstructed bone phantoms for the imaginary part of complex permittivity, by varying the noise level.

SNR (dB)	Circular array			Calcaneus-shaped array		
	P1	P2	P3	P1	P2	P3
20	0.314	0.386	0.409	0.399	0.277	0.406
30	0.320	0.361	0.332	0.396	0.276	0.430
40	0.315	0.399	0.386	0.417	0.339	0.427
50	0.348	0.397	0.378	0.380	0.277	0.396
60	0.335	0.409	0.362	0.378	0.276	0.398

4.3.2.4. Histogram analysis

Additionally, in this work, a histogram-based analysis was carried out. The distribution of the reconstructed real part of the complex permittivity value was computed among each pixel within the target region. As shown in Figure 4.9 and Figure 4.10, the reconstruction of P3 was the most challenging, especially for the calcaneus-shaped antenna configuration: the reference value for the osteoarthritic trabecular bone in terms of the real part of the complex permittivity is almost 29, where the properties of almost half (i.e., 49%) of the reconstructed pixels fall into values ranging between 20 and 22.

Nevertheless, the qualitative visual reconstruction of this phantom for both the simulation testbeds and the corresponding performance metrics shows promising results, especially in terms of SSIM. The reason for these slightly low values for P3, as already explained, can be related to the fact that osteoarthritic bone has higher dielectric properties compared to normal and osteoporotic ones. Therefore, due to the higher contrast between the cortical and the trabecular bone regions, the reconstruction is less accurate.

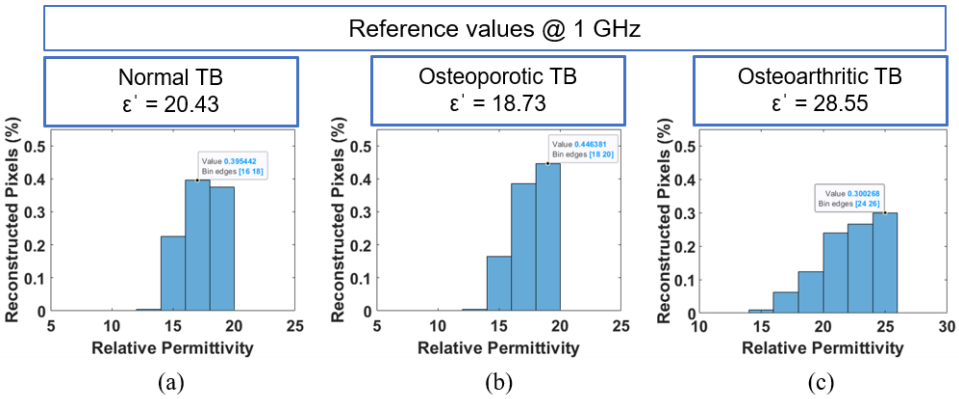

Figure 4. 9: Distribution of reconstructed real part of complex permittivity of (a) bone phantom P1, (b) bone phantom P2, (c) bone phantom P3 at 1 GHz for the circular array testbed.

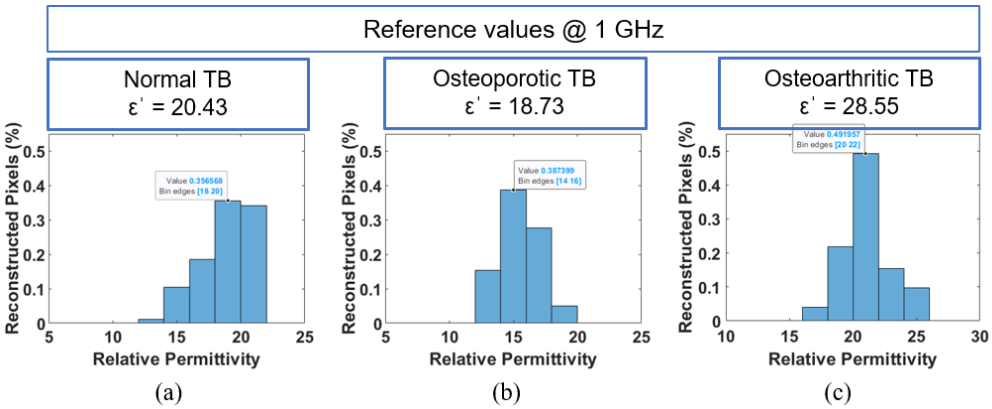

Figure 4. 10: Distribution of reconstructed real part of complex permittivity of (a) bone phantom P1, (b) bone phantom P2, (c) bone phantom P3 at 1 GHz for the calcaneus-shaped array testbed.

4.3.2.5. Robustness of the L_2-IMATCS algorithm

To evaluate the robustness of the proposed imaging algorithm, the peak values of the reference and the reconstructed numerical bone properties have been investigated. In Figure 4.11, the peak values comparing the reference and reconstructed values of the trabecular bone tissue across the two simulation testbeds are reported. In this analysis, the different physical configurations of the antennas have been considered, to assess whether they could have affected the obtained reconstructions. As can be noticed, regardless of the kind of scenario (i.e., normal, osteoporotic, osteoarthritic) and the antenna configuration, the peak values within the trabecular bone region related to the reconstructed imaginary part of the complex permittivity are higher than the reference.

The greatest percentage difference between the reference and reconstructed peak values, in terms of the real part of complex dielectric

permittivity, has been obtained within the reconstruction of P3, which was expected according to the previous results. A difference of 11.8% has been reported between the reference osteoarthritic trabecular tissue and the reconstructed one in the calcaneus-shaped antenna configuration. Nonetheless, the average percentage difference between the overall reference and reconstructed real part of the peak values of the phantoms is 6.41%, which suggests that the method can perform well varying either the simulation testbed or the kind of phantom. In Figure 4.12, both the relative percentage errors for the real and the imaginary part between the reference and reconstructed peak values are shown. As can be noticed in Figure 12 (b), for all the employed phantoms the error is lower when the calcaneus-shaped configuration is considered compared to the cases related to the circular configuration, proving the robustness of the proposed method even though in a more geometrically complex antenna configuration. The higher value of the error in terms of reconstructed peak values, particularly within the circular configuration, might be due to the set threshold, which was specifically tailored to produce good results in terms of the shape and dimension of the reconstructed scene rather than to reach the exact target value of the investigated region.

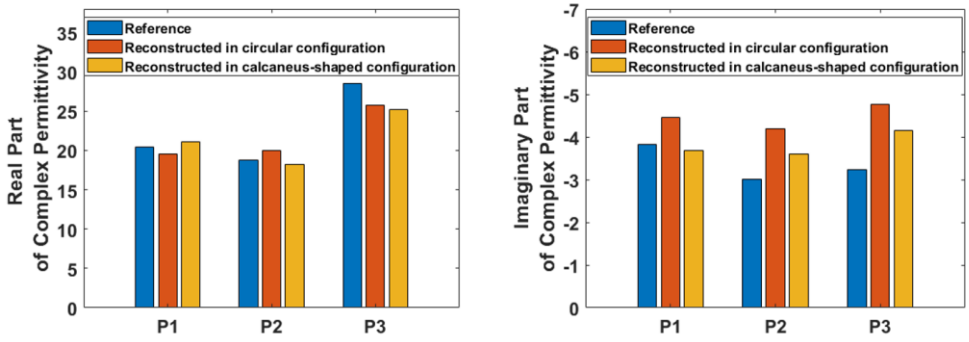

Figure 4. 11: Peak values of the (a) real and (b) imaginary part of complex permittivity of reference and reconstructed bone phantoms at 1 GHz.

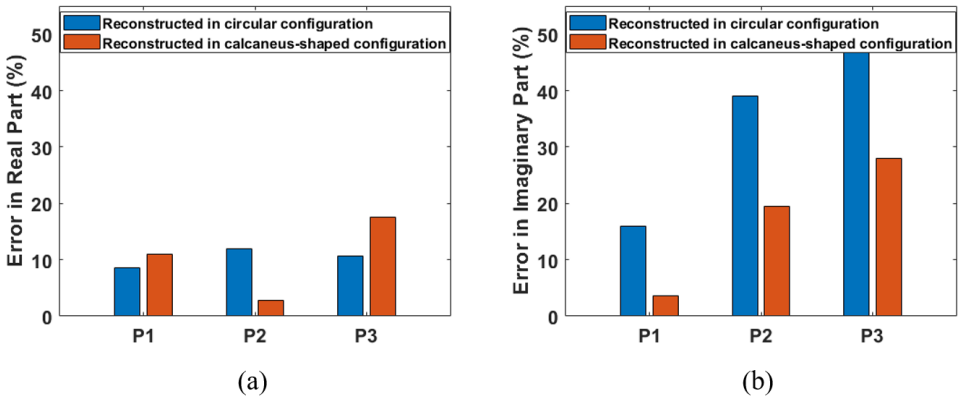

Figure 4. 12: Relative percentage error between peak values of the (a) real and (b) imaginary part of complex permittivity of reference and reconstructed bone phantoms at 1 GHz.

4.3.2.6. Investigation on the impact of the skin layer addition

In this analysis, the objective was to assess whether it could be possible to reconstruct a heterogeneous scenario involving even the presence of a thin skin layer. The numerical phantom adopted in this framework was designed as a three-layer calcaneus-shaped model for the 2D scenario evaluation, starting from phantom P1 (healthy conditions) of the previous sections. The two inner layers, as already explained, are meant to reproduce the two layers of human bones (i.e., the outer cortical bone layer and the inner trabecular bone layer). The outermost layer represents the human skin layer. Five different versions of this phantom were considered for the analysis by varying the thickness of the skin layer, even considering the case of a two-layered phantom without skin (i.e., P1 where thickness = 0 mm). Table 4.6 provides an overview of the employed numerical phantoms. The numerical three-layer structure was transformed into an electromagnetic model according to the single-pole Debye parameters of each layer, given by [25], [149]. The Debye parameters of the skin tissue for the frequency range of 0.5-8.5 GHz are as follows: $\varepsilon_\infty = 2.848$, $\Delta\varepsilon = 1.104$, $\sigma_s = 0.005$ S/m. Imaging data were collected through a circular array consisting of 16 equally spaced point source antennas with a 45 mm radius. An example of the considered 2D imaging scenario involving phantom P1_2 is shown in Figure 4.13.

Table 4. 6: Numerical bone phantoms for simulations.

Phantom Label	Layers Structure		
	Inner layer	**Outer layer**	**Skin thickness [mm]**
P1	Trabecular bone	Cortical bone	0 (no skin)
P1_1	Trabecular bone	Cortical bone	1
P1_2	Trabecular bone	Cortical bone	2
P1_3	Trabecular bone	Cortical bone	3
P1_4	Trabecular bone	Cortical bone	4

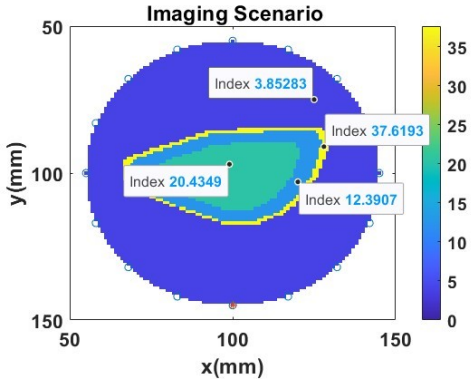

Figure 4. 13: Circular simulation testbed with phantom P1_2, coloured according to the corresponding real part of the complex permittivity.

Generally, human skin does not exceed 2 mm in thickness [150]. However, in some cases, it is worth considering the thickening of the skin layer, primarily due to clinical conditions such as edema [52]. Previous studies on microwave breast imaging have reported that the presence of the skin layer only has minor effect on the numerical reconstruction of the target inner tissues working within the microwave field [150], even though its properties are relatively high compared to those of the adjacent tissues [60], [151]. The main effect related to the presence of the skin is mostly visible from the furthest receiving antennas. A visual plot of the magnitude of the signals transmitted by a fixed antenna (i.e., antenna #1) as a function of the receiving antenna location is provided in Figure 4.14.

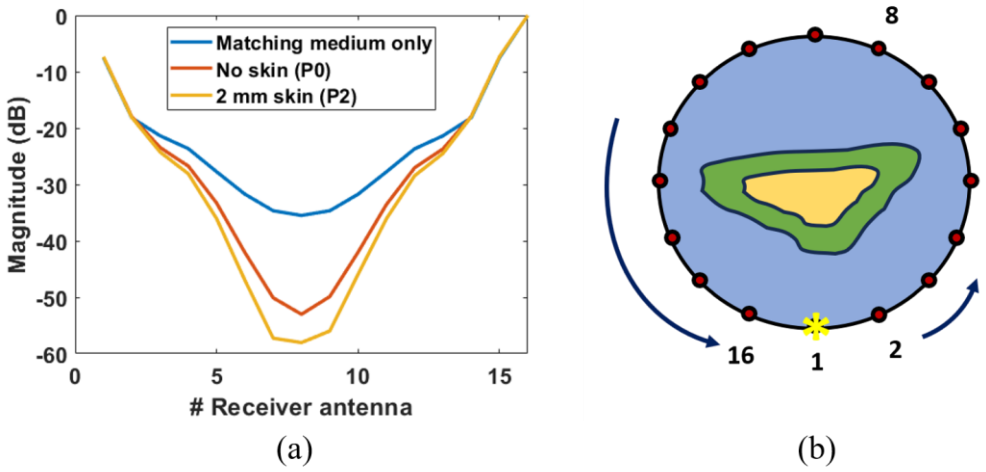

Figure 4. 14: Magnitude values depending on the receiving antenna locations in 2 mm skin and non-skin cases. Also the background noise of the model is provided (blue curve) (a). Schema of the antenna locations (b).

From this figure, it can be seen that the received signals - i.e., from the closest (i.e., antenna #2 and #15) to the furthest (i.e., antenna #8 and #9)

antennas - are slightly affected by the presence of the skin layer, considering the most realistic case scenario (i.e., phantom P1_2: 2 mm skin). The numerical reconstructions of the phantoms at 1 GHz are shown in Figure 4.15 below.

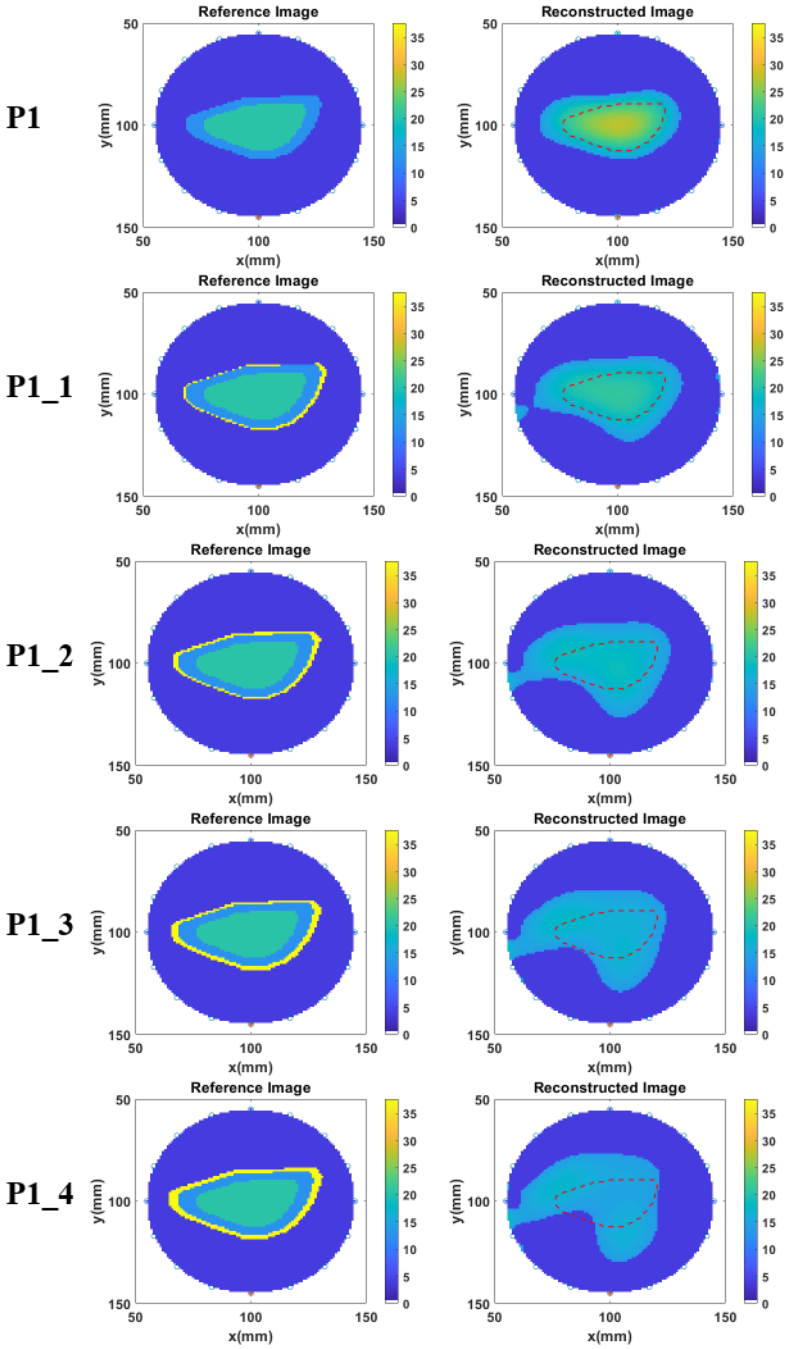

Figure 4. 15: Reference (left) and reconstructed (right) 2D real part of the dielectric complex profiles at 1 GHz of phantoms P1, P1_1, P1_2, P1_3, and P1_4. The red dotted line indicates trabecular bone region.

The reconstructed 2D images show good overall matching with the reference dielectric profiles of the three-layer bone phantoms, at least in the

region of interest (i.e., the trabecular bone region), even by varying the thickness of the skin layer. In the worst-case scenario (i.e., P1_4: 4 mm skin), the reconstructed region was not correctly positioned within the reference target region. In addition, when the skin thickness is increased, the method fails to reconstruct the expected shape of the bone. However, as already mentioned, in normal clinical conditions, the skin is typically 1-2 mm, indicating that the proposed combination of algorithms is suitable for bone health assessment under physiological conditions. The skin layer was not reconstructed for each phantom, in agreement with what was achieved in [150]. However, the inner tissue properties were reliably recovered. To quantitatively assess the results of the present study, two performance metrics were calculated (i.e., NRMSE and SSIM). The results are presented in Table 4.7. The tabulated values of the two metrics for the real and imaginary parts of the complex permittivity for each phantom suggest that a good reconstruction was achieved. Hence, the DBIM/IMATCS algorithm, which has already been studied in simpler scenarios, exhibited appreciable performance in the challenging case of a three-layered phantom involving the skin layer. As expected, in the case of thicker skin layers, the performance was slightly diminished. Thus, the algorithms succeeded in the recovery of the dielectric properties' values in the region of interest, failing to retrieve the reference shape and dimension of the numerical phantoms when increasing the skin thickness. For this reason, even in the worst-case scenario (i.e., P1_4), good values for both metrics were achieved.

Table 4. 7: NRMSE and SSIM between reference and reconstructed phantoms.

Phantom Label	NRMSE		SSIM	
	ε'	ε''	ε'	ε''
P1	0.151	0.313	0.995	0.998
P1_1	0.183	0.409	0.993	0.998
P1_2	0.193	0.393	0.985	0.989
P1_3	0.222	0.399	0.971	0.978
P1_4	0.262	0.415	0.911	0.946

4.4. Experimental bone phantoms investigation

This part of the study has been conducted to make a step towards a more realistic clinical condition. Indeed, it focuses on the MWT image reconstruction of experimental anthropomorphic calcaneus phantoms by using a specialized microwave bone imaging prototype. So far in this thesis, only numerical anthropomorphic phantoms have been considered to optimize and test the DBIM/IMATCS imaging method. A previous attempt

to apply the proposed method in an experimental environment has been done in [25], where the authors developed a simplistic two-layer experimental bone phantom, having a circular shape. Since the method revealed promising results in a numerical scenario employing conformal phantoms, as explained in the previous section, and in an experimental context involving a simpler phantom, here the aim was to make the scenario as realistic as possible by trying to reconstruct the dielectric profiles of realistic calcaneus-shaped phantoms. For this reason, six different experimental calcaneus-shaped multi-layer phantoms have been realized, which were composed of liquid and solid TMMs. The peripheral location of the calcaneus makes it suitable for MWI application, in a perspective to do such investigation on real patients. The proposed liquid TMMs (based on deionized water, salt and Triton-X 100) were firstly dielectrically characterized over the frequency range of 1 - 4 GHz, to assess whether they could reproduce the dielectric properties of the reference human bone tissues (i.e., skin, cortical bone, healthy and diseased trabecular bone). One of the main advantages in using these mixtures is that their electromagnetic parameters can be predicted based on the concentrations the ingredients. This is achieved using a binary fluid mixture model, such as Böttcher's formula [152], [153], which leverages the Debye models applicable to both Triton X-100 and saline water. Subsequently, the phantoms underwent imaging tests to validate the capability of the proposed imaging method in reconstructing each experimental scenario. The trabecular bone region, as already outlined, is the main target to detect since it is the most sensitive tissue to musculoskeletal conditions.

This work, indeed, introduces two main novelties. Firstly, multi-layer phantoms have been tested even considering the presence of the skin layer, for the first time made by using either liquid or solid TMMs. This layer is often neglected in works involving experimental phantoms, due to its challenging realization [150] and because its higher dielectric properties, compared to the other bone tissues, may cause distortions and strong reflections [26], [150], [154]. Moreover, as explained before conformal phantoms have been employed, with the same shape and dimensions as the human calcaneus.

Particularly, two different 3D models have been developed to mimic the human calcaneus - i.e., a 3D printed polylactic acid (PLA) mold and a carbon black anatomically realistic structure - and the performance in the reconstruction of their properties was retrieved and compared. Previous studies have found that the presence of 3D PLA layers may affect the measurements and cause strong electromagnetic (EM) reflections [152]. For this reason, a carbon black-based calcaneus phantom has been considered as well to realize a multi-layered experimental phantom. The cavities of the proposed model were meant to be filled by liquid materials, avoiding perturbance to the signals due to the presence of PLA structures and aiming at removing any unwanted artifact from the final images.

4.4.1. Liquid phantoms recipes and preparation

Five liquid TMMs have been developed to mimic the dielectric properties of different human bone tissues (including cortical bone (CB), healthy, osteoporotic, and osteoarthritic trabecular bone (TB), and skin tissue). The recipes to obtain these materials involved the use of three ingredients: deionized water, Triton-X 100 and salt (NaCl), as shown in Table 4.8. A solution of deionized water and salt is prepared at first. The right amount of Triton-X 100, according to the recipe, is then slowly poured into the same glass beaker. The whole solution is mixed until the disappearance of the air bubbles, for 3-4 minutes. The main advantages in dealing with this kind of liquid TMMs are that they are easy to produce, reusable, long-term stable, and suitable for both characterization and imaging purposes [152]. Once the mixtures were prepared, they were poured into plastic labelled containers and stored at 22°C.

One main drawback of Triton-X 100-based liquid phantoms is that when the quantity of Triton-X 100 reaches 40-50% within the mixture of deionized water and salt, the liquid TMM becomes very viscous and almost solid [16]. To avoid this issue, all the measurements involving osteoarthritic trabecular bone and skin TMMs were conducted shortly after developing the phantoms (1-2 hours).

Two different 3D multi-layered models have been considered to represent the realistic human calcaneus with its actual dimension. The former is a 3D-printed PLA mold (mold A), and the latter is a carbon black mold (mold B). For what concerns the mold A, the skin TMM is meant to be poured in the outermost layer, followed by the cortical and the trabecular bone TMMs. Mold B, instead, is represented by a carbon black-based structure, composed of carbon black, graphite, polyurethane and isopropanol. Detailed directions on the preparation of such materials are provided in [152]. In mold B, the layers themselves are carbon black solid TMMs, representing the dielectric properties of the skin and the cortical bone [152]. This second model, thus, allows for the realization of a complete phantom composed of four layers, including even the fat layer (between the skin and the cortical bone regions). This last one has been realized by using a 100% Triton-X liquid, as already developed in [22].

Figure 4.16 shows both the described molds used in this experimental study. It is worth noticing that the thickness of the skin layer is 1 mm, which represents a realistic human value. In this work, both a healthy and a diseased scenario have been investigated and a total of six phantoms have been realized by combining the different molds and the mixtures representing the trabecular bone (i.e., P1: mold A, healthy scenario; P2: mold A, osteoporotic scenario; P3: mold A, osteoarthritic scenario; P4: mold B, healthy scenario; P5: mold B, osteoporotic scenario; P6: mold B, osteoarthritic scenario) (Table 4.9).

Table 4. 8: Liquid TMMs recipes.

Mimicked tissue	Ingredients		
	Triton -X 100 (ml)	Deionized water (ml)	NaCl (g/l)
CB	77	23	0.8
Healthy TB	62	38	0.8
Osteoporotic TB	68	32	0.8
Osteoarthritic TB	50	50	2.4
Skin	40	60	5.2

CB = cortical bone, TB = trabecular bone.

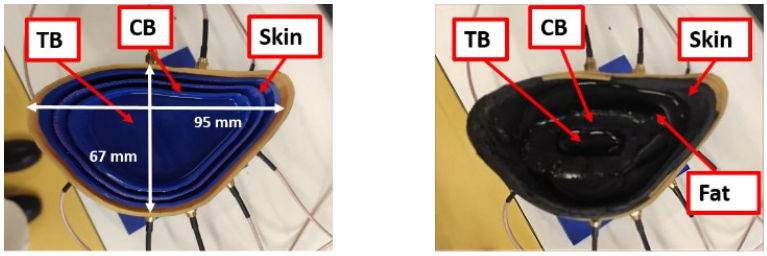

(a) (b)

Figure 4. 16: Physical representations of the two molds: PLA-based three-layer mold (mold A) (a); carbon black four-layer mold (mold B) (b). In Figure 1 (a) the white arrows represent the dimension of the PLA support of the two molds.

Table 4. 9: Anthropomorphic phantoms composition.

Phantom name	Characteristics	
	Trabecular bone	Mold type (see Figure 4.16)
P1	Healthy	A
P2	Osteoporotic	A
P3	Osteoarthritic	A
P4	Healthy	B
P5	Osteoporotic	B
P6	Osteoarthritic	B

4.4.2. Imaging setup

The proposed imaging prototype is depicted in Figure 4.17. The measured signals were collected through nine microstrip antennas which were arranged in a planar configuration and equally spaced around a specific 3D-printed PLA support container where the mold A and B were housed. The antennas have been connected through flexible cables to a ZN-Z84 24-port switching

matrix followed by a 2-port ZNB40 VNA (Rohde and Schwartz GmbH, Munich, Germany). These microstrip antennas were previously employed in different works regarding other medical contexts. As an example, they have been used in a system involving a 16-element antenna array on patients in the field of breast imaging applications [61], [155], [156]. Earlier, these antennas were designed to be put in contact with the skin directly [61], [155], [156]. For this reason, even in the present work no matching medium has been employed for the proposed investigations.

The measurements have been carried out in the frequency range of 1 - 4 GHz over 200 linearly spaced points and a single record for each transmit-receive antenna pair has been considered for the 2D tomographic reconstructions, for a total of 36 signals (i.e., N(N-1)/2 where N stands for the number of antennas). The VNA input power has been set to -10 dBm. Since the ZNB40 VNA used in the measurements has a dynamic range of 90 dB, this input level is high enough to produce a strong signal above the noise floor, yet low enough to prevent saturation of the VNA receivers or any non-linear effects in the material under test. The experimental setup has been calibrated automatically through a R&S®ZN-Z129E Network Analyzer Calibration Kit, Rhode & Schwarz, in such a way to perform the calibration at the nine coaxial cables ends.

Data have been acquired with and without the liquid TMMs in place. The measurements related to empty mold A and B have been used to calibrate the data.

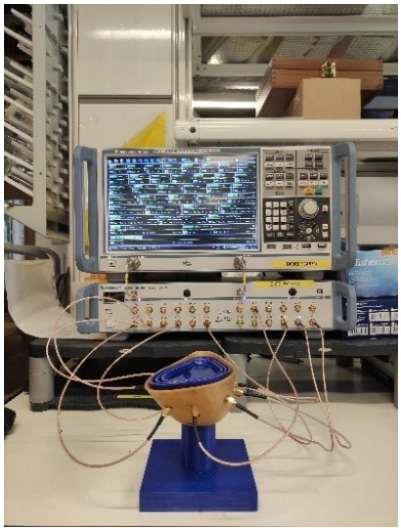

Figure 4. 17: Imaging setup with the mold A in place.

4.4.3. FDTD modelling and calibration of measured data

As previously outlined, 36 EM scattered signals from the nine microstrip antennas were collected. The experimental imaging scenario has been reproduced as a 2D imaging model to perform the numerical simulations. To do this in a two-dimensional numerical representation of the

anthropomorphic phantom, the antennas were modelled as point sources. A finite-difference-time-domain (FDTD) method has been adopted to carry out the simulations. The same homogeneous loss-less and non-dispersive background medium as in the earlier numerical analysis has been considered as the initial guess for the DBIM method (with Debye's parameters ε_∞= 2.848, $\Delta\varepsilon$ = 1.104, σ_s = 0.005 S/m). The relaxation time constant was set equal to the constant value of 0.05 ps in such a way to simplify the FDTD simulations and no a-priori information has been considered to perform the inversion method. The comparison between the measured data and the simulated EM scattered ones provides the solution to the inverse problem [157], [158]. Since the antennas employed in the FDTD 2D numerical model are not realistic, this may lead to propagation and scattering errors. As already done in previous works, a calibration procedure was applied before inversion, which followed different step [25], [143]. Firstly, two measurements were carried out in order to obtain the incident field of the considered system (i.e., the field without the phantom in place ($S_{obj}^m(f)$) and the total field (i.e., the field with the phantom in place within the 3D model ($S_{ref}^m(f)$). Secondly, a 2D FDTD simulation (i.e., $E_{ref}^s(f)$) has been performed to evaluate the incident field at receiver locations via a Matlab FDTD code, which simulates the reference data. Hence, the calibration of the signals was carried out before the inversion process, as displayed below:

$$E_{cal}^m(f) = \frac{S_{obj}^m(f)}{S_{ref}^m(f)} * E_{ref}^s(f) \tag{4.12}$$

4.4.4. Results and discussion

4.4.4.1. Dielectric properties of the TMMs

The liquid TMMs were arranged in plastic containers and underwent dielectric characterization in a frequency range between 1 and 4 GHz. The measurements have been performed through a similar setup as that described in Chapter 2. It was composed by an open-ended coaxial slim probe (i.e., Keysight slim form probe 85070E) and a Keysight E5063A Vector Network Analyzer (VNA). A mechanical mover has been employed to correctly position the probe within the liquid TMMs, as shown in Figure 4.18. The real part of the complex dielectric permittivity (ε') and the conductivity (σ (S/m)) were computed by collecting five measurements for each TMM to get more reliable results. The experimental setup has been calibrated through the use of three known loads (i.e., deionized air, water, and short circuit) and the measurements have been carried out at 22° C. The dielectric properties of a saline solution at 0.1 M were measured as well to verify the calibration [17], [25]. In particular, the uncertainty (in percentage) ACC_{UC} of the accuracy has been calculated as:

$$ACC_{UC} = \frac{(y_{meas}(f) - y_{ref}(f))}{y_{ref}(f)} \times 100 \quad (4.13)$$

where y_{meas} represents the measured dielectric properties of the 0.1 M saline solution, while y_{ref} is the corresponding reference dielectric properties from [159]; f indicates the frequency vector. Moreover, the uncertainty REP_{UC} related to the repeatability of the performed measurements has been calculate as follows:

$$REP_{UC} = \frac{(y_{meas}(f) - y_{mean}(f))}{y_{mean}(f)} \times 100 \quad (4.14)$$

where y_{mean} represents the mean of 9 measurements performed on the 0.1 M saline solution. Both the metrics have been calculated separately in terms of ε' (i.e., real part of the relative permittivity) and σ (S/m) (i.e., conductivity) respectively. The values achieved from this analysis are tabulated in Table 4.10, where the total combined uncertainty (defined as the sum of the two metrics) is reported as well.

Table 4. 10: Percent uncertainty of accuracy and repeatability of measurements.

Parameter	**ε'**	**σ (S/m)**
Uncertainty of the accuracy ACC_{UC} (%)	0.05	1.36
Uncertainty of the repeatability REP_{UC} (%)	0.04	0.1
Combined (%)	0.09	1.46

The results of the dielectric measurements of the liquid mixtures are shown in Figure 4.19, where a comparison with the corresponding reference human tissues dielectric properties is provided as well [134], [159]. The dielectric properties of the TMMs demonstrated to be overall compliant with the dielectric properties of the corresponding human tissues. Indeed, the average difference between the real part of the complex permittivity of each pair of experimental-reference curves is less than ±10% for every liquid TMM. The strongest difference between the reference and reconstructed dielectric properties values has been observed for the osteoarthritic TMM, especially in terms of conductivity (i.e., green curve). Table 4.11 shows the average values of the dielectric properties of these materials and the corresponding human tissues at 3 GHz.

The results of the dielectric characterization of the solid carbon black TMMs (i.e., the skin and cortical bone solid TMM involved in this study) have been reported previously in [152]. The characterization of such materials followed the same procedure described previously. Measurements were obtained from different positions to assess the homogeneity of the layer and get reliable results.

Table 4. 11: Dielectric properties of the TMMs and the corresponding biological tissues at 3 GHz.

Target tissue		Dielectric properties @ 3 GHz	
		ε'	σ (S/m)
CB	TMM	9.81	0.86
	Tissue	11.06	0.50
Healthy TB	TMM	18.84	1.48
	Tissue	17.94	1.00
OP TB	TMM	16.57	1.27
	Tissue	17.18	2.83
OA TB	TMM	28.95	2.14
	Tissue	26.37	4.35
Skin	TMM	38.33	2.57
	Tissue	37.45	1.74

CB = cortical bone, TB = trabecular bone, OP = osteoporotic, OA = osteoarthritic.

In Figure 4.20 the dielectric properties of the solid TMMs (i.e., the skin, cortical bone and normal trabecular bone TMM) from [152] are reported; a comparison with the properties of the corresponding human tissues is provided as well, from [134], [159]. A small mismatch can be noticed between the trends of the reference-reconstructed curves referred to as the conductivity of the skin. Nonetheless, as can be noticed from Figures 4.19 and 4.20, good results have been achieved and the mixtures were found suitable to represent the target human tissue in the investigated frequency range.

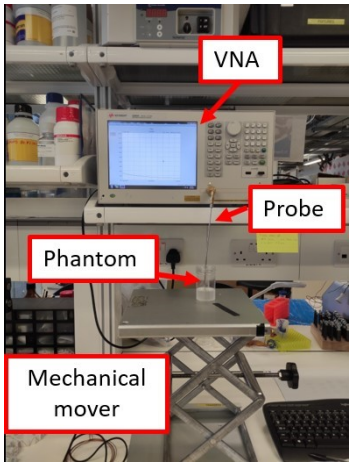

Figure 4. 18: Dielectric characterization setup.

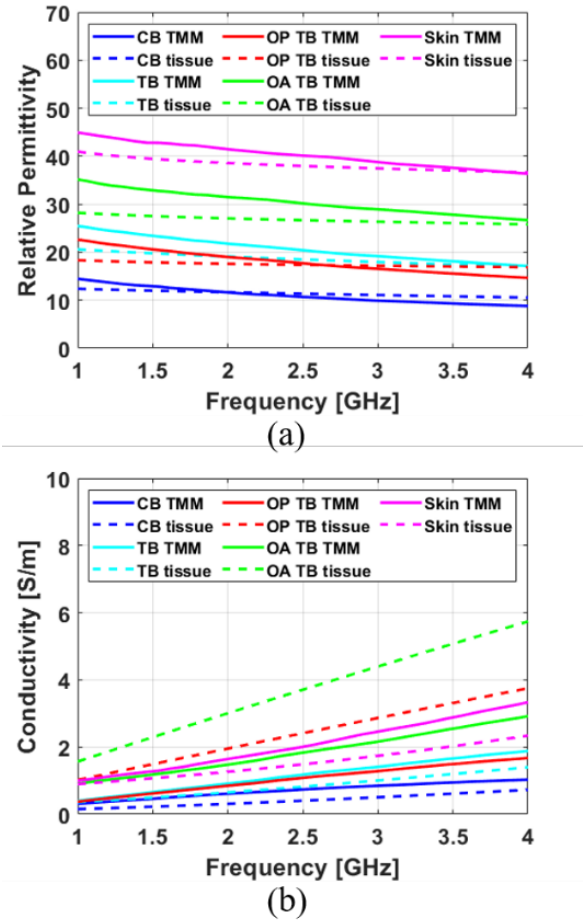

Figure 4. 19: Dielectric properties of the liquid TMMs (solid lines) and the corresponding biological tissues (dashed lines): (a) Relative permittivity and (b) Conductivity. (CB = cortical bone, TB = trabecular bone, OP = osteoporotic, OA = osteoarthritic.)

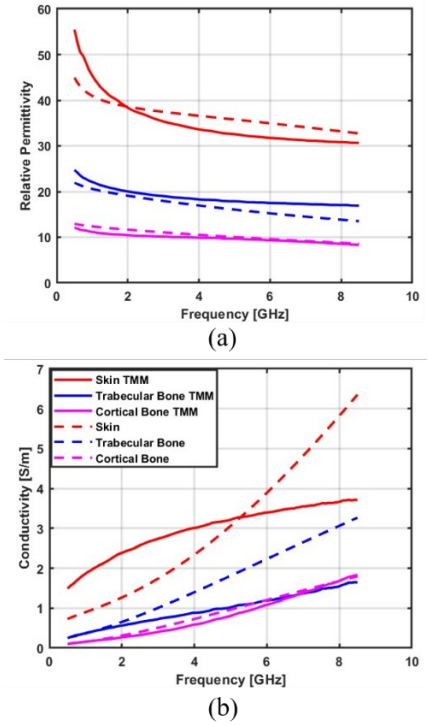

Figure 4. 20: Dielectric properties of the solid TMMs (solid lines) and the corresponding biological tissues (dashed lines) over the 0.5–8.5 GHz frequency band, from **[152]**: (a) relative permittivity and (b) conductivity.

4.4.4.2. 2D image reconstructions of experimental phantoms

The liquid TMMs of skin, cortical bone and trabecular bone were poured within the corresponding tissue layers of the PLA 3D models. For the imaging acquisition, priority was given to the mold A measurements (i.e., phantoms P1, P2, P3), since it involved the presence of the skin liquid TMM which was the most challenging to handle because of its viscosity. Data were acquired through the nine microstrip antennas and the DBIM/L_2-IMATCS algorithm was applied to the 36 recorded signals.

As already mentioned, also a measurement for each empty mold was conducted, which was used to calibrate the experimental data. The implemented FDTD simulations, described in Section 4.4.3, were used as a forward solver during the inversion process, as already done previously [157], [158]. This procedure was performed in a uniform grid cell size of 1 mm.

A parametric analysis was performed to properly set the values of the different parameters of the algorithms. The reconstruction frequency of phantoms P1 and P2 was set at 3.35 GHz, whereas the properties of P3 were reconstructed at 3.41 GHz since the results were found to carry more information at this frequency value. The reason for this choice refers to the fact that the main principle of MWI relies on the dielectric contrast between the different investigated materials. Several tests on the optimization of the reconstruction frequency have been conducted, leading to the conclusion that

the nature of the trabecular phantoms (i.e., healthy, osteoporotic and osteoarthritic) and its contrast against the cortical one determined a difference in the selection of the proper frequency. Particularly, the contrast between the osteoarthritic trabecular bone and the healthy cortical one is higher, resulting in the optimized choice of 3.41 GHz for the reconstruction. Instead, 3.35 GHz was set as the reconstruction frequency for the healthy and osteoporotic cases, where the contrast against the cortical tissue is similar. This allowed us to achieve more significant results in terms of reconstructed properties. Nonetheless, it is worth observing that the imaginary part of the complex dielectric permittivity was the most challenging to reconstruct regardless of the conditions (thus, the properties) of the trabecular bone. However, the main aim of the study was to determine whether it was possible to distinguish between the different analyzed cases based on the reconstructed properties. The study demonstrated that the employed materials and the selected frequencies of reconstructions made it feasible to discriminate the conditions (i.e., healthy, osteoporotic, osteoarthritic bone) of the trabecular bone region based on the retrieved properties. The 2D reconstructed real and imaginary parts of complex permittivity profiles for each phantom using mold A (i.e., P1, P2 and P3) are reported in Figure 4.21, Figure 4.22 and Figure 4.23, respectively.

As can be noticed from these qualitative reconstructions, the method performed well in reconstructing all the phantoms, even when the osteoarthritic trabecular bone TMM, which has higher dielectric properties than the surrounding layers, was involved (i.e., P3). Apparently, within the reconstructions referred to the cases involving the osteoporotic trabecular TMM (i.e., P2), the shape and location of the target trabecular region are less accurate than in the other cases. The osteoporotic tissue is the one characterized by the lowest dielectric properties. This could have affected the reconstructions, suggesting that the proposed method in experimental conditions performs better in contexts with higher contrast between adjacent layers.

It was observed that when employing phantoms including the osteoarthritic trabecular bone TMMs (i.e., P3), higher values of the threshold were required to achieve better performance. This may probably be related to the higher dielectric properties of the osteoarthritic trabecular bone compared to the other tissues involved in the measurements.

Moreover, in every reconstruction, the skin layer was not recovered, as previously observed in numerical and experimental scenarios involving simpler phantoms [147], and even in the numerical analysis performed in the present thesis. However, that is expected as documented in other works concerning MWT when skin is implied [150]. Additionally, for all the reconstructed cases, the desired values of the imaginary part of the complex dielectric permittivity, as mentioned before, were never reached. For this reason, Figures 4.21-4.23 show a different upper limit of the color bars between the reference (b) and reconstructed (d) distribution of the imaginary

part of the complex dielectric permittivity, in such a way to highlight the retrieved contrast between the different layers.

The liquid TMMs representing the human fat and the different kinds of trabecular bone have been arranged within the four-layered carbon black structure for the imaging acquisition of mold B phantoms. The skin-like layer and the cortical bone-like one, in this case, are represented by solid carbon black phantoms with compatible human tissues' properties, as shown before. Again, the acquisitions of phantom P4 and P5 (i.e., normal and osteoporotic trabecular TMM) have been performed at 3.35 GHz while the measurements regarding P6, involving the osteoarthritic trabecular TMM, have been performed at 3.41 GHz.

The reconstructed dielectric properties of the phantoms using mold B are reported in Figure 4.24, Figure 4.25 and Figure 4.26. Almost the same considerations regarding mold A phantoms, can be done for mold B phantoms. In particular, both the real and the imaginary part of the complex permittivity of phantom P6 report a very high contrast between the reconstructed trabecular bone properties and the surrounding tissues.

Even in this case, the skin is never reconstructed, and the strongest antenna reflections can be seen within the reconstruction of P6. Moreover, the overall reconstructed imaginary part, as observed for mold A phantoms, never reached the desired value.

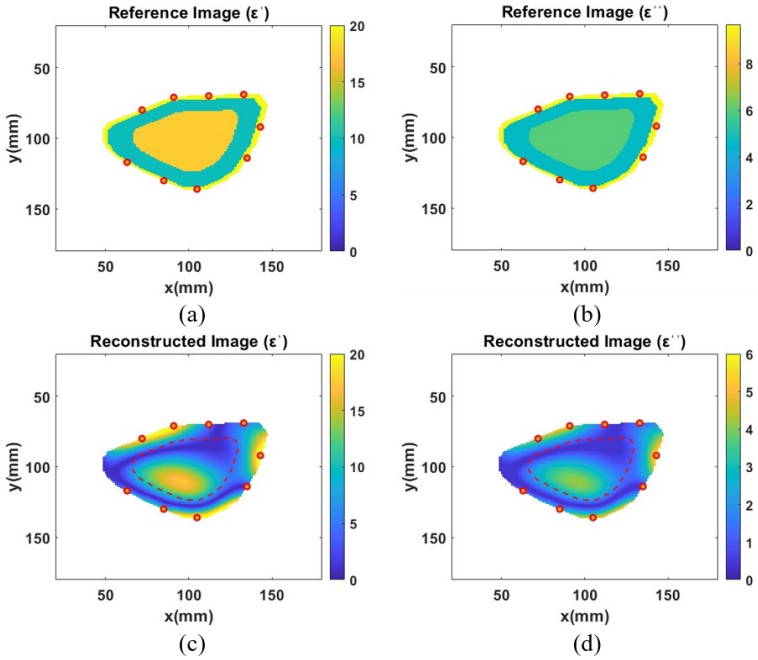

Figure 4. 21: 2D reference (a), (b) and reconstructed (c), (d) distributions of the real (left) and imaginary (right) parts of complex permittivity at 3.35 GHz of P1. The red dotted line represents the reference target profiles, while the orange circles stand for the antennas.

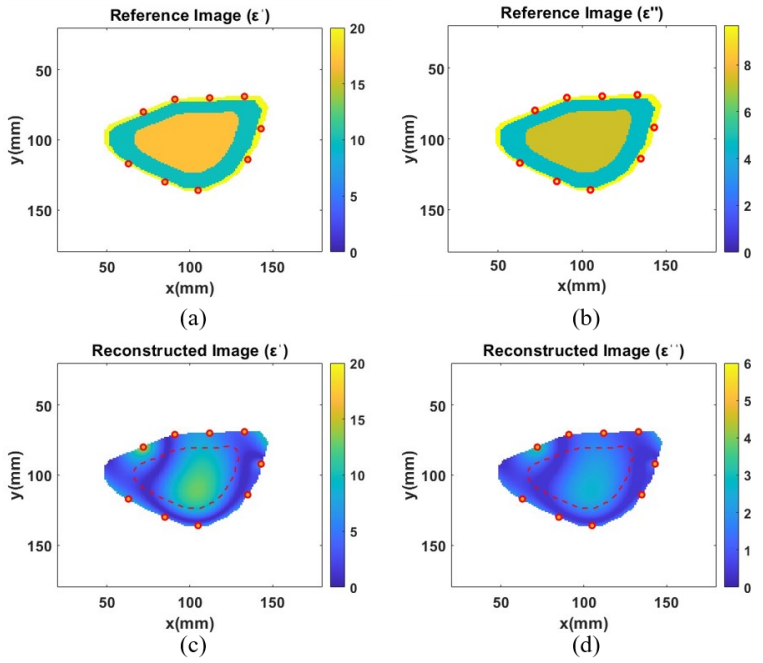

Figure 4. 22: 2D reference (a), (b) and reconstructed (c), (d) distributions of the real (left) and imaginary (right) parts of complex permittivity at 3.35 GHz of P2. The red dotted line represents the reference target profiles, while the orange circles stand for the antennas.

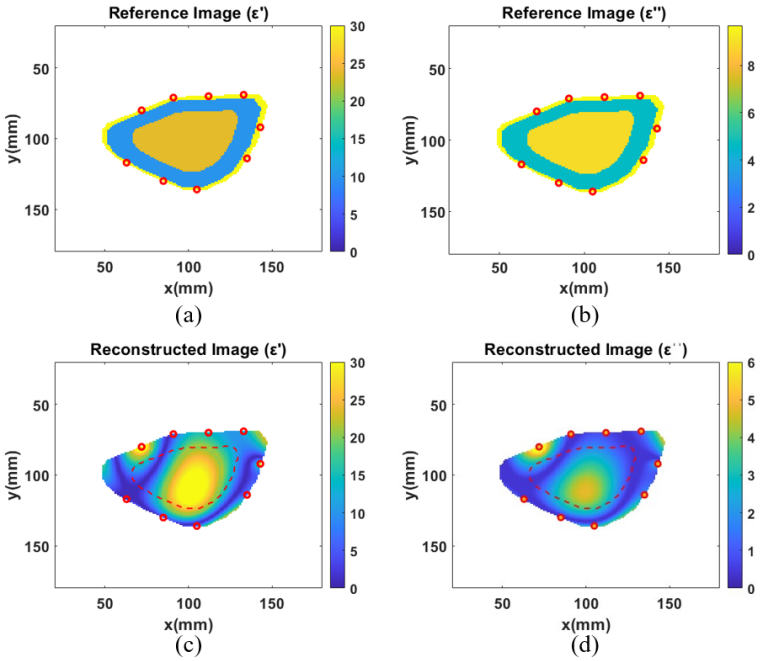

Figure 4. 23: 2D reference (a), (b) and reconstructed (c), (d) distributions of the real (left) and imaginary (right) parts of complex permittivity at 3.41 GHz of P3. The red dotted line represents the reference target profiles, while the orange circles stand for the antennas.

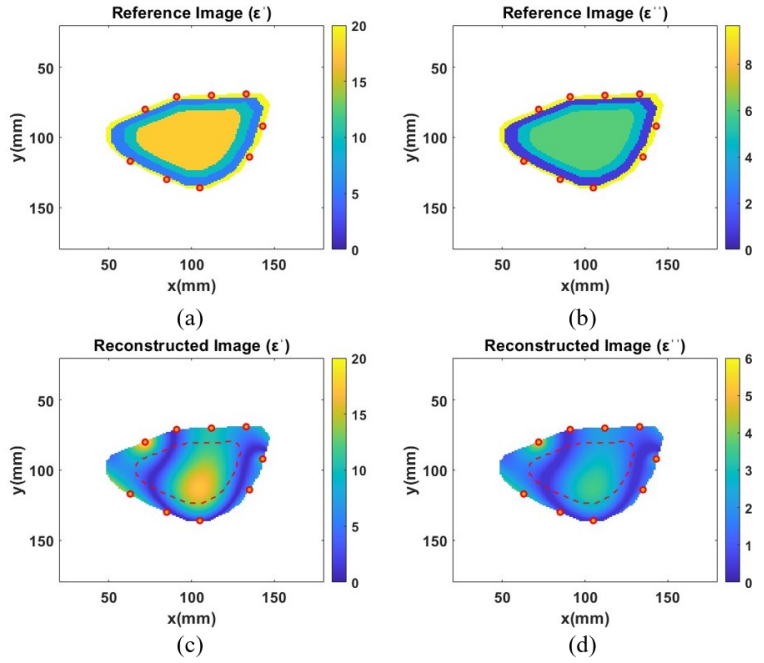

Figure 4. 24: 2D reference (a), (b) and reconstructed (c), (d) distributions of the real (left) and imaginary (right) parts of complex permittivity at 3.35 GHz of P4. The red dotted line represents the reference target profiles, while the orange circles stand for the antennas.

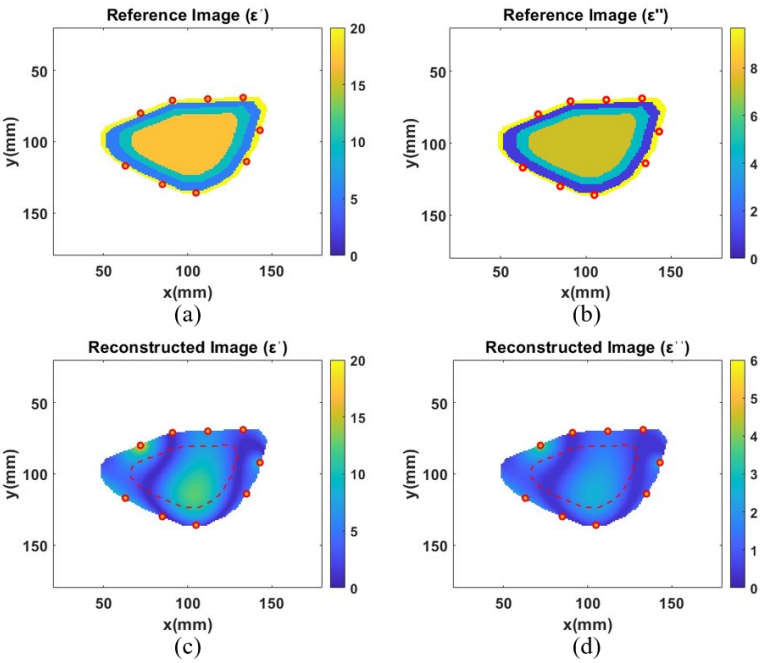

Figure 4. 25: 2D reference (a), (b) and reconstructed (c), (d) distributions of the real (left) and imaginary (right) parts of complex permittivity at 3.35 GHz of P5. The red dotted line represents the reference target profiles, while the orange circles stand for the antennas.

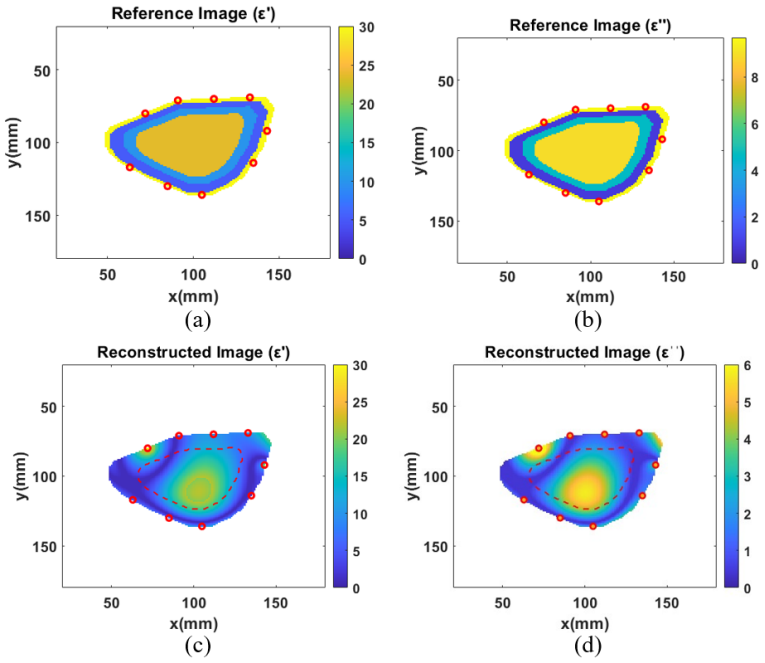

Figure 4. 26: 2D reference (a), (b) and reconstructed (c), (d) distributions of the real (left) and imaginary (right) parts of complex permittivity at 3.41 GHz of P6. The red dotted line represents the reference target profiles, while the orange circles stand for the antennas.

4.4.4.3. Quantitative performance evaluation

Following the same procedure as in the numerical analysis, the employed imaging algorithm has been evaluated even in terms of robustness. In particular, for each case, a comparison between the peak value of the real and the imaginary parts of the complex permittivity of the reference and reconstructed bone phantoms has been investigated. In Figures 4.27 the results of this analysis are displayed. As can be noticed, the peak values of the reconstructed properties related to mold A are slightly higher than the ones related to mold B, except for what concerns the reconstructions of the osteoarthritic phantoms P3 and P6 (i.e., the third column of the bar plots).

Moreover, for what concerns the reconstructed imaginary part of all the phantoms, Figure 4.27 (b) shows that the reference value is never reached, regardless of the mold type involved.

However, based on the calculated peak values, the healthy and the diseased scenarios can be distinguished based on the reconstructed properties at the chosen reconstruction frequency.

The NRMSE and the SSIM have been calculated to quantitatively evaluate the performance of the proposed imaging algorithm. The results of the two metrics for both ε' and ε'' are reported in Table 4.12. The table shows overall good values for each experiment. Indeed, as can be seen also in Figures 4.21 - 4.26, the method succeeded in detecting and positioning the target region (i.e., the trabecular bone region) and reliable recovery of the properties can be noticed.

The achieved NRMSE values, which suggest a relatively high error computed by comparing the reference and the reconstructed models, could be due to the measurements carried out in a noisy environment, where it is difficult to predict the level of signal-to-noise ratio (SNR). However, the proposed calibration method (described in section 4.4.3) has been used to ensure the removal of experimental noise as much as possible. Moreover, as previously mentioned, this metric has been calculated considering the entire reference and reconstructed images, which may have influenced the obtained performance.

Table 4. 12: NRMSE and SSIM between the reference and reconstructed bone phantom dielectric properties.

Phantoms		NRMSE	SSIM
P1	ε'	0.591	0.955
	ε''	0.774	0.840
P2	ε'	0.727	0.958
	ε''	0.963	0.825
P3	ε'	0.806	0.958
	ε''	0.961	0.825
P4	ε'	0.722	0.966
	ε''	0.927	0.840
P5	ε'	0.716	0.952
	ε''	0.945	0.821
P6	ε'	0.804	0.946
	ε''	0.966	0.825

In [25], a similar investigation as in this study has been conducted, employing a simpler phantom (i.e., a circular two-layer phantom) reconstructed through the same DBIM/L_2-IMATCS imaging algorithm. The resulting NRMSE, in the present study, as expected, is higher due to the more geometrically complex scenario involving more layers. The performance in terms of SSIM, which was calculated among pixels within the target region only, revealed good values suggesting that promising reconstruction in terms of similarity with the reference complex dielectric profiles can be achieved.

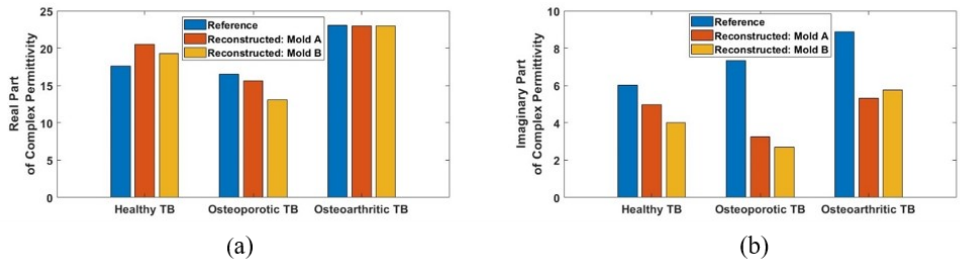

Figure 4. 27: Peak values of the imaginary part of complex permittivity of reference and reconstructed bone phantoms across the two different molds.

4.5. Conclusion

This work has provided a numerical and experimental evaluation of an MWT algorithm in a realistic 2D imaging scenario. For what concerns the numerical investigations, the phantoms under test have been designed as a two-layered calcaneus-shaped model. Both a healthy and a diseased context have been considered. The simulated data were generated using two different antenna configurations. The first circular configuration was evaluated in a previous study employing a simpler phantom consisting of a two-layered circular structure. In contrast, the second configuration, which had a calcaneus-shaped array, was tested for the first time in this current work. The dielectric properties of the phantoms were reconstructed at 1 GHz using a DBIM approach combined with an L_2-IMATCS algorithm, which has shown promising results in several studies. The results of the present work show that it is possible to extend this method to a more complex scenario involving a realistic phantom. The method proved its efficacy in accurately reconstructing the dielectric properties of the phantom, specifically designed to mimic the complex anatomical structure of the human calcaneus. Moreover, the results provided by the calcaneus-shaped simulation testbed suggest that this method is robust in terms of changes referred to the spatial configuration of the antennas.

The reconstructions of the numerical phantoms have shown that the normal, osteoporotic and osteoarthritic bones can be accurately distinguished based on their reconstructed complex permittivity profiles.

Moreover, a three-layer realistic numerical bone phantom was tested which included a thin outer layer of skin surrounding the 2D electromagnetic model composed of cortical and trabecular bone layers. The reconstructions were achieved using the previously proposed DBIM-IMATCS algorithm. The resulting maps of the distribution of the complex dielectric permittivity showed that it is possible to achieve reliable recovery of the reference properties even when the skin is included. By increasing the thickness of the skin layer, it is visible that the position, shape and dimension of the target region are not properly conserved. However, the quantitative evaluation of the study showed that good performance in terms of NRMSE and SSIM can

be achieved. Moreover, when realistic cases are considered (i.e., 1- or 2-mm skin thickness) results remain satisfying.

Nonetheless, the proposed method is not able to reconstruct the properties of the skin layer, which is expected when working in the microwave field as documented in previous works concerning the same topic.

Further investigation may focus in the optimized selection of the regularization parameters (i.e., the adaptive threshold parameters of the IMATCS algorithm), which can lead to a more precise properties recovery. Also, it is worth investigating the role of the involved matching medium: in this work a loss-less, non-dispersive matching medium was employed. A possible next step could be to use a lossy medium, as already tried in breast imaging contexts, since it may limit signal perturbations and noise during the propagation of the EM waves.

As a final step of this work, this study explores the MWT reconstruction of different experimental bone phantoms considering both healthy and diseased scenarios. Five liquid TMMs including phantoms mimicking both healthy and diseased trabecular tissues of the human bones have been realized and dielectrically characterized. The dielectric properties of the developed TMMs were found to be compliant with the reference dielectric properties of corresponding human tissues in the investigated frequency range.

Two different 3D models have been considered to perform imaging investigations, representing healthy, osteoporotic and osteoarthritic scenarios. These models involved the use of different solid molds (i.e., a PLA mold and carbon black-based one). The 2D reconstructed images at 3.35 GHz and 3.41 GHz showing the complex dielectric profiles of the phantoms exhibited good reconstructions in terms of position and properties of the retrieved target trabecular bone region. The reconstructions of the osteoporotic scenarios were the most challenging, probably due to the low dielectric properties of the osteoporotic trabecular bone TMM compared to the surrounding TMMs.

No significant differences have been observed between the reconstructions across the two different molds, suggesting the possibility of using indistinctly liquid and solid phantoms for this kind of application. However, within the reconstructions of the different molds, it is possible to notice an artifact on the top left antenna, which may probably be due to the irregular geometric configuration of the proposed array.

The results of the study proved the validity of the proposed imaging method involving the designed phantoms in reconstructing the desired scenarios, in both healthy and diseased cases. The normal, osteoporotic and osteoarthritic trabecular bones can be distinguished based on the retrieved properties in an experimental context with an average percentage difference of 25%.

Future works may focus towards the realization of more complex and realistic phantoms reproducing as accurately as possible the anatomic structure of the human bones.

Chapter 5

Conclusion and future developments

The present thesis explored several aspects related to the development, characterization, and evaluation of novel microwave and millimeter-wave imaging systems, focusing on two diagnostic areas: the early detection of breast cancer and bone health assessment. The conducted research and the achievements allowed to address three main aspects: the design of tissue-mimicking phantoms for such applications, the realization of two acquisition architectures based on different imaging approaches for the two diagnostic questions (i.e., radar-based and tomographic imaging techniques) and the optimization of the corresponding imaging algorithms. The developed methods have been validated through the use of numerical and experimental phantoms.

The research presented in **Chapter 2** has provided an in-depth analysis of the dielectric, mechanical, and acoustic characterization of phantoms mimicking human healthy and diseased breast tissues. These phantoms were created using simple mixtures based on safe, non-expensive and easy-to-handle materials (resulting in oil-in-gelatin and oil-in-agar mixtures), and were originally tailored to reproduce the dielectric properties of the corresponding human tissues. The recipes were based on previous works, with adjustments to better improve the suitability to emulate, specifically, the mechanical and the acoustic properties of breast tissues while maintaining their previously studied dielectric properties.

Dielectric properties were initially measured up to 14 GHz and fitted using the Cole-Cole model to predict their trends up to 50 GHz. Overall, the dielectric permittivity curves showed a good agreement with *ex-vivo* human breast tissues data, even when modifying the phantoms recipes. However, while dielectric measurement methods are well-established, uncertainties remain regarding mechanical characterization. A significant effort in this context has been made to establish a protocol for the mechanical characterization of the produced semi-solid phantoms, with the aim to fill the existing gap in the literature, where measurement conditions are rarely provided. The analysis focused on the impact of two key factors—preload and test speed—on the mechanical properties. Tests under different conditions (preloads of 0.1 N, 0.2 N, and 0.4 N, and speeds of 0.5 mm/min to 80 mm/min) showed that preload significantly affects the

mechanical behavior of tumor phantoms (i.e., with high gelatin percentage content and thus increased stiffness), but not that of soft-tissue-mimicking phantoms.

The comparison of the achieved mechanical properties and literature data showed consistency for healthy-like phantoms but revealed a need for new formulations to better mimic malignant tissue properties. To address this, materials with modified solidifying agents were introduced. Agar-based phantoms proved better ability to reproduce stiffer tissues properties than gelatin-based ones, but showed more complicated efforts to simultaneously match mechanical and dielectric properties.

The mechanical contrast between malignant and healthy tissues was explored as well, highlighting compatible results with the poor existing literature and proving the suitability of the developed materials to reproduce the desired properties.

Two of the established bi-modal phantoms, one mimicking tumor tissue and the other healthy fat tissue, underwent even acoustic characterization, which showed that both were suitable representations of real breast tissues from a dielectric, mechanical, and acoustic point of view. Future research may involve creating and acoustically testing a fibro-glandular tissue phantom, along with further investigations into improving echogenicity and acoustic properties using materials like graphite or glass beads.

Finally, multi-layer breast phantoms for microwave imaging were constructed in this part of the thesis, highlighting the potential of these materials in advancing, training, and refining microwave breast imaging systems, aligning with trends in radar-based microwave imaging.

Chapter 3 has provided insights into the development of a novel microwave/millimeter-wave radar-based imaging prototype, specifically for breast cancer detection, including the hardware design and software optimization. The performance of such system was assessed also using the phantoms developed earlier in Chapter 2. An experimental protocol dedicated to signals and images acquisition has been proposed, which involved antennas of three different frequency bands, highlighting the possibility to extend the functionality of the system up to the millimeter-wave range, aligning with the current literature on the same topic. Preliminary analyses regarding the signal propagation were conducted without any target in X-band (8-12 GHz), Ku-band (12-18 GHz) and K/Ka-band (18-40 GHz) frequency ranges. This helped to set the proper values of the acquisition parameters of interest and the optimal hardware configuration. The resulting standard acquisition and calibration parameters defined in Chapter 3 can be summarized as follows: calibration bandwidth ranging between 10 MHz – 44 GHz, according to the VNA operating band; 4001 acquired points for each measurement, which were found suitable to obtain reliable Fourier Transforms in each of the acquisition frequency bands; Intermediate Frequency set to 100 kHz; VNA output power: 0 dBm and no signal averaging in acquisition/calibration. The combination of such parameters allowed for the collection of reproducible and reliable signals. The crosstalk phenomenon occurring between antennas has been investigated and quantified as well, which showed reproducibility over a series of measurements employing the same antennas in different days.

Hence, several target detection measurements have been performed employing some of the previously developed tissue-mimicking phantoms in order to study the power and the losses of the reflected signals. Subsequently, imaging tests have been conducted both in numerical and experimental contexts. Different scenarios have been considered (which included different media with inclusions in varying positions) and tests were performed in all the three frequency bands mentioned above. The collected radar signals were used as input for two beamforming algorithms (i.e., DAS and F-DMAS). An optimization analysis has been carried out to find the optimal value of the scan parameters to be used in transmission (including the Gaussian pulse type, width, and the kind of adopted modulation), showing that good quality image reconstructions can be achieved through the proposed settings through both beamforming algorithms. Further developments of this research will focus on the study of new antennas configurations (i.e., conformal) for imaging purposes and the testing of more complex geometry phantoms with multiple layers and interfaces. The feasibility of the realization of such phantoms has been already assessed in Chapter 2. Another interesting next step of this work could be the implementation of a tomographic approach to image the data acquired by the proposed system prototype.

Chapter 4, finally, explores a tomographic imaging approach in a non-oncological application. The focus of this Chapter refers to microwave imaging for bone health assessment, with validation through numerical and experimental phantoms. Specifically, this part of the research, which has been conducted in collaboration with the Translational Medical Device Lab at the University of Galway, in Ireland, evaluated a microwave tomography (MWT) algorithm in a realistic 2D imaging scenario, focusing on both healthy and diseased bone tissue models. The study has been split into a numerical and an experimental analysis. The former utilized a two-layered calcaneus-shaped phantom (comprising a cortical and a trabecular bone layer) and compared two antenna configurations: a previously tested circular configuration and a newly introduced calcaneus-shaped array, with antennas surrounding the anthropomorphic phantom. The dielectric properties of the phantoms were reconstructed using the DBIM/L_2-IMATCS algorithm at 1 GHz, demonstrating its effectiveness in mimicking complex bone anatomy.

Results show that the method accurately allowed to distinguish between normal, osteoporotic, and osteoarthritic bones based on their complex permittivity profiles. A three-layer realistic bone phantom, including skin, cortical, and trabecular bone, was also tested. While increasing skin thickness caused slight distortions in the target region, the method still achieved good performance in terms of error metrics (NRMSE and SSIM). However, the skin dielectric properties could not be reconstructed, consistently with previous studies, probably due to the very reduced thickness of such layer.

The study also investigated experimental phantoms using liquid and solid tissue-mimicking materials (TMMs) to simulate, again, both healthy and diseased bone tissues. Six different phantoms involving three or four different layers were employed for acquisitions of signals within the 1-4 GHz frequency band in the proposed imaging prototype. The obtained images were reconstructed around 3 GHz according to the reconstruction frequency of previous studies on bone and breast microwave imaging through tomographic

approaches. The imaging results successfully differentiated between normal and diseased bones showing that healthy, osteoporotic and osteoarthritic trabecular bone phantoms could be distinguished with a 25% average percentage difference.

Further developments may focus on perfectioning the 3D phantom structures (e.g., by modeling the inner layers of the phantoms in such a way to represent as realistically as possible the corresponding human tissues stratifications). However, this study validated the MWT method for bone imaging, suggesting the potential for more complex, anatomically accurate phantoms and even for *in-vivo* studies in future works, to further refine bone health diagnostics.

References

[1] D. Koundal, V. Kadyan, P. Dutta, V. Anand, S. Aggarwal, and S. Gupta, "Computational techniques in biomedical image analysis: overview," in *Advances in Computational Techniques for Biomedical Image Analysis*, Elsevier, 2020, pp. 3–31. doi: 10.1016/B978-0-12-820024-7.00001-3.

[2] H. Kasban, M. A. M. El-Bendary, and D. H. Salama, "A Comparative Study of Medical Imaging Techniques," 2015.

[3] N. AlSawaftah, S. El-Abed, S. Dhou, and A. Zakaria, "Microwave Imaging for Early Breast Cancer Detection: Current State, Challenges, and Future Directions," *J. Imaging*, vol. 8, no. 5, p. 123, Apr. 2022, doi: 10.3390/jimaging8050123.

[4] J. S. Sung, "High-quality Breast Ultrasonography," *Radiol. Clin. North Am.*, vol. 52, no. 3, pp. 519–526, May 2014, doi: 10.1016/j.rcl.2014.02.012.

[5] J.-L. Gennisson, T. Deffieux, M. Fink, and M. Tanter, "Ultrasound elastography: Principles and techniques," *Diagn. Interv. Imaging*, vol. 94, no. 5, pp. 487–495, May 2013, doi: 10.1016/j.diii.2013.01.022.

[6] E.-M. Lochmüller, R. Müller, V. Kuhn, C. A. Lill, and F. Eckstein, "Can Novel Clinical Densitometric Techniques Replace or Improve DXA in Predicting Bone Strength in Osteoporosis at the Hip and Other Skeletal Sites?," *J. Bone Miner. Res.*, vol. 18, no. 5, pp. 906–912, May 2003, doi: 10.1359/jbmr.2003.18.5.906.

[7] S. Di Meo, A. Cannatà, S. Morganti, G. Matrone, and M. Pasian, "On the dielectric and mechanical characterization of tissue-mimicking breast phantoms," *Phys. Med. Biol.*, vol. 67, no. 15, p. 155018, Aug. 2022, doi: 10.1088/1361-6560/ac7bcc.

[8] S. Di Meo *et al.*, "Tissue-mimicking materials for breast phantoms up to 50 GHz," *Phys. Med. Biol.*, vol. 64, no. 5, p. 055006, Feb. 2019, doi: 10.1088/1361-6560/aafeec.

[9] M. Lazebnik, E. L. Madsen, G. R. Frank, and S. C. Hagness, "Tissue-mimicking phantom materials for narrowband and ultrawideband microwave applications," *Phys. Med. Biol.*, vol. 50, no. 18, pp. 4245–4258, Sep. 2005, doi: 10.1088/0031-9155/50/18/001.

[10] C. Hahn and S. Noghanian, "Heterogeneous Breast Phantom Development for Microwave Imaging Using Regression Models," *Int. J. Biomed. Imaging*, vol. 2012, pp. 1–12, 2012, doi: 10.1155/2012/803607.

[11] A. A. Bakar, A. Abbosh, and M. Bialkowski, "Fabrication and characterization of a heterogeneous breast phantom for testing an ultrawideband microwave imaging system".

[12] R. S. Akki and K. Arunachalam, "Breast tissue phantoms to assist compression study for cancer detection using microwave radiometry," in *2014 36th Annual International Conference of the IEEE Engineering in Medicine and Biology Society*, Chicago, IL: IEEE, Aug. 2014, pp. 1119–1122. doi: 10.1109/EMBC.2014.6943791.

[13] B. Henin and A. M. Abbosh, "Electro-biomechanical breast phantom for hybrid breast imaging".

[14] G. Ruvio *et al.*, "Multimodal Breast Phantoms for Microwave, Ultrasound, Mammography, Magnetic Resonance and Computed Tomography Imaging," *Sensors*, vol. 20, no. 8, p. 2400, Apr. 2020, doi: 10.3390/s20082400.

[15] S. Li, E. Fear, and L. Curiel, "Breast tissue mimicking phantoms for combined ultrasound and microwave imaging," *Phys. Med. Biol.*, vol. 66, no. 24, p. 245011, Dec. 2021, doi: 10.1088/1361-6560/ac3d18.

[16] N. Joachimowicz, B. Duchêne, C. Conessa, and O. Meyer, "Anthropomorphic Breast and Head Phantoms for Microwave Imaging," *Diagnostics*, vol. 8, no. 4, p. 85, Dec. 2018, doi: 10.3390/diagnostics8040085.

[17] B. Amin, D. Kelly, A. Shahzad, M. O'Halloran, and M. A. Elahi, "Microwave calcaneus phantom for bone imaging applications," in *2020 14th European Conference on Antennas and Propagation (EuCAP)*, Copenhagen, Denmark: IEEE, Mar. 2020, pp. 1–5. doi: 10.23919/EuCAP48036.2020.9135355.

[18] A. Cannatà, S. Di Meo, G. Matrone, S. Morganti, and M. Pasian, "Multimodal tissue-mimicking breast phantoms for mm-wave and ultrasound imaging," in *2023 17th European Conference on Antennas and Propagation (EuCAP)*, Florence, Italy: IEEE, Mar. 2023, pp. 1–5. doi: 10.23919/EuCAP57121.2023.10133246.

[19] L. A. Groves *et al.*, "A Review of Low-Cost Ultrasound Compatible Phantoms," *IEEE Trans. Biomed. Eng.*, vol. 70, no. 12, pp. 3436–3448, Dec. 2023, doi: 10.1109/TBME.2023.3288071.

[20] M. Cavagnaro, R. Pinto, and V. Lopresto, "Phantoms in hyperthermia and thermal ablation applications at microwave frequencies: a review".

[21] H. M. Ismail, C. G. Pretty, M. K. Signal, M. Haggers, C. Zhou, and J. G. Chase, "Mechanical behaviour of tissue mimicking breast phantom materials," *Biomed. Phys. Eng. Express*, vol. 3, no. 4, p. 045010, Jul. 2017, doi: 10.1088/2057-1976/aa7992.

[22] M. Relva and S. Devesa, "Dielectric Stability of Triton X-100-Based Tissue-Mimicking Materials for Microwave Imaging," *Spectrosc. J.*, vol. 1, no. 2, pp. 72–85, Aug. 2023, doi: 10.3390/spectroscj1020007.

[23] J. A. T. Vasquez *et al.*, "Experimental assessment of qualitative microwave imaging using a 3-D realistic breast phantom," in *2017 11th European Conference on Antennas and Propagation (EUCAP)*, Paris: IEEE, Mar. 2017, pp. 2728–2731. doi: 10.23919/EuCAP.2017.7928477.

[24] T. Reimer, S. Christie, and S. Pistorius, "A Quantitative Analysis of the Plastic Shell Effects in 3D- Printed Breast Phantoms for Microwave Imaging," in *2022 16th European Conference on Antennas and Propagation (EuCAP)*, Madrid, Spain: IEEE, Mar. 2022, pp. 1–5. doi: 10.23919/EuCAP53622.2022.9768915.

[25] B. Amin, A. Shahzad, M. O'halloran, B. Mcdermott, and A. Elahi, "Experimental Validation of Microwave Imaging Prototype and DBIM-IMATCS Algorithm for Bone Health Monitoring," *IEEE Access*, vol. 10, pp. 42589–42600, 2022, doi: 10.1109/ACCESS.2022.3167715.

[26] L. Kranold, J. Boparai, L. Fortaleza, and M. Popovic, "A Comparative Study of Skin Phantoms for Microwave Applications," in *2020 42nd Annual International Conference of the IEEE Engineering in Medicine &*

Biology Society (EMBC), Montreal, QC, Canada: IEEE, Jul. 2020, pp. 4462–4465. doi: 10.1109/EMBC44109.2020.9175857.

[27] J. Garrett and E. Fear, "Stable and Flexible Materials to Mimic the Dielectric Properties of Human Soft Tissues," *IEEE Antennas Wirel. Propag. Lett.*, vol. 13, pp. 599–602, 2014, doi: 10.1109/LAWP.2014.2312925.

[28] E. C. Fear, P. M. Meaney, and M. A. Stuchly, "Microwaves for breast cancer detection?," *IEEE Potentials*, vol. 22, no. 1, pp. 12–18, Feb. 2003, doi: 10.1109/MP.2003.1180933.

[29] V. Zhurbenko, "Challenges in the Design of Microwave Imaging Systems for Breast Cancer Detection," *Adv. Electr. Comput. Eng.*, vol. 11, no. 1, pp. 91–96, 2011, doi: 10.4316/AECE.2011.01015.

[30] R. Chandra, H. Zhou, I. Balasingham, and R. M. Narayanan, "On the Opportunities and Challenges in Microwave Medical Sensing and Imaging," *IEEE Trans. Biomed. Eng.*, vol. 62, no. 7, pp. 1667–1682, Jul. 2015, doi: 10.1109/TBME.2015.2432137.

[31] E. C. Fear, X. Li, S. C. Hagness, and M. A. Stuchly, "Confocal microwave imaging for breast cancer detection: localization of tumors in three dimensions," *IEEE Trans. Biomed. Eng.*, vol. 49, no. 8, pp. 812–822, Aug. 2002, doi: 10.1109/TBME.2002.800759.

[32] H. Been Lim, N. Thi Tuyet Nhung, E.-P. Li, and N. Duc Thang, "Confocal Microwave Imaging for Breast Cancer Detection: Delay-Multiply-and-Sum Image Reconstruction Algorithm," *IEEE Trans. Biomed. Eng.*, vol. 55, no. 6, pp. 1697–1704, Jun. 2008, doi: 10.1109/TBME.2008.919716.

[33] Yao Xie, Bin Guo, Luzhou Xu, Jian Li, and P. Stoica, "Multistatic Adaptive Microwave Imaging for Early Breast Cancer Detection," *IEEE Trans. Biomed. Eng.*, vol. 53, no. 8, pp. 1647–1657, Aug. 2006, doi: 10.1109/TBME.2006.878058.

[34] E. J. Bond, Xu Li, S. C. Hagness, and B. D. Van Veen, "Microwave imaging via space-time beamforming for early detection of breast cancer," *IEEE Trans. Antennas Propag.*, vol. 51, no. 8, pp. 1690–1705, Aug. 2003, doi: 10.1109/TAP.2003.815446.

[35] M. Persson *et al.*, "Microwave-Based Stroke Diagnosis Making Global Prehospital Thrombolytic Treatment Possible," *IEEE Trans. Biomed. Eng.*, vol. 61, no. 11, pp. 2806–2817, Nov. 2014, doi: 10.1109/TBME.2014.2330554.

[36] S. Mustafa, B. Mohammed, and A. Abbosh, "Novel Preprocessing Techniques for Accurate Microwave Imaging of Human Brain," *IEEE Antennas Wirel. Propag. Lett.*, vol. 12, pp. 460–463, 2013, doi: 10.1109/LAWP.2013.2255095.

[37] B. J. Mohammed, A. M. Abbosh, S. Mustafa, and D. Ireland, "Microwave System for Head Imaging," *IEEE Trans. Instrum. Meas.*, vol. 63, no. 1, pp. 117–123, Jan. 2014, doi: 10.1109/TIM.2013.2277562.

[38] S. Brovoll, T. Berger, Y. Paichard, O. Aardal, T. S. Lande, and S.-E. Hamran, "Time-lapse imaging of human heartbeats using UWB radar," in *2013 IEEE Biomedical Circuits and Systems Conference (BioCAS)*, Rotterdam, Netherlands: IEEE, Oct. 2013, pp. 142–145. doi: 10.1109/BioCAS.2013.6679659.

[39] S. Brovoll, T. Berger, Y. Paichard, O. Aardal, T. S. Lande, and S.-E. Hamran, "Time-Lapse Imaging of Human Heart Motion With Switched Array UWB Radar," *IEEE Trans. Biomed. Circuits Syst.*, vol. 8, no. 5, pp. 704–715, Oct. 2014, doi: 10.1109/TBCAS.2014.2359995.

[40] N. Nikolova, "Microwave Imaging for Breast Cancer," *IEEE Microw. Mag.*, vol. 12, no. 7, pp. 78–94, Dec. 2011, doi: 10.1109/MMM.2011.942702.

[41] S. Di Meo *et al.*, "On the Feasibility of Breast Cancer Imaging Systems at Millimeter-Waves Frequencies," *IEEE Trans. Microw. Theory Tech.*, vol. 65, no. 5, pp. 1795–1806, May 2017, doi: 10.1109/TMTT.2017.2672938.

[42] S. Di Meo, G. Matrone, and M. Pasian, "Experimental Validation on Tissue-Mimicking Phantoms of Millimeter-Wave Imaging for Breast Cancer Detection," *Appl. Sci.*, vol. 11, no. 1, p. 432, Jan. 2021, doi: 10.3390/app11010432.

[43] F. Topfer and J. Oberhammer, "Millimeter-Wave Tissue Diagnosis: The Most Promising Fields for Medical Applications," *IEEE Microw. Mag.*, vol. 16, no. 4, pp. 97–113, May 2015, doi: 10.1109/MMM.2015.2394020.

[44] P. Mojabi, M. Ostadrahimi, L. Shafai, and J. LoVetri, "Microwave tomography techniques and algorithms: A review," in *2012 15 International Symposium on Antenna Technology and Applied Electromagnetics*, Toulouse, France: IEEE, Jun. 2012, pp. 1–4. doi: 10.1109/ANTEM.2012.6262367.

[45] C. Gilmore, A. Abubakar, W. Hu, T. M. Habashy, and P. M. Van Den Berg, "Microwave Biomedical Data Inversion Using the Finite-Difference Contrast Source Inversion Method," *IEEE Trans. Antennas Propag.*, vol. 57, no. 5, pp. 1528–1538, May 2009, doi: 10.1109/TAP.2009.2016728.

[46] R. Scapaticci, I. Catapano, and L. Crocco, "Wavelet-Based Adaptive Multiresolution Inversion for Quantitative Microwave Imaging of Breast Tissues," *IEEE Trans. Antennas Propag.*, vol. 60, no. 8, pp. 3717–3726, Aug. 2012, doi: 10.1109/TAP.2012.2201083.

[47] P. M. Meaney *et al.*, "Initial Clinical Experience with Microwave Breast Imaging in Women with Normal Mammography," *Acad. Radiol.*, vol. 14, no. 2, pp. 207–218, Feb. 2007, doi: 10.1016/j.acra.2006.10.016.

[48] J. D. Shea, P. Kosmas, S. C. Hagness, and B. D. Van Veen, "Three-dimensional microwave imaging of realistic numerical breast phantoms via a multiple-frequency inverse scattering technique," *Med. Phys.*, vol. 37, no. 8, pp. 4210–4226, Aug. 2010, doi: 10.1118/1.3443569.

[49] A. Cannatà *et al.*, "Microwave Bone Imaging: Reconstruction of Anthropomorphic Numerical Calcaneus Phantoms for Bone Diseases Diagnosis," *IEEE Access*, pp. 1–1, 2024, doi: 10.1109/ACCESS.2024.3454523.

[50] B. Amin, A. Shahzad, M. O'Halloran, and M. A. Elahi, "Microwave Bone Imaging: A Preliminary Investigation on Numerical Bone Phantoms for Bone Health Monitoring," *Sensors*, vol. 20, no. 21, p. 6320, Nov. 2020, doi: 10.3390/s20216320.

[51] K. D. Paulsen, S. P. Poplack, Dun Li, M. W. Fanning, and P. M. Meaney, "A clinical prototype for active microwave imaging of the breast," *IEEE*

Trans. Microw. Theory Tech., vol. 48, no. 11, pp. 1841–1853, Nov. 2000, doi: 10.1109/22.883861.

[52] P. M. Meaney *et al.*, "Microwave imaging for neoadjuvant chemotherapy monitoring: initial clinical experience," *Breast Cancer Res.*, vol. 15, no. 2, p. R35, Apr. 2013, doi: 10.1186/bcr3418.

[53] R. Scapaticci, M. Bjelogrlic, J. A. Tobon Vasquez, F. Vipiana, M. Mattes, and L. Crocco, "Microwave Technology for Brain Imaging and Monitoring: Physical Foundations, Potential and Limitations," in *Emerging Electromagnetic Technologies for Brain Diseases Diagnostics, Monitoring and Therapy*, L. Crocco, I. Karanasiou, M. L. James, and R. C. Conceição, Eds., Cham: Springer International Publishing, 2018, pp. 7–35. doi: 10.1007/978-3-319-75007-1_2.

[54] R. Scapaticci, L. Di Donato, I. Catapano, and L. Crocco, "A FEASIBILITY STUDY ON MICROWAVE IMAGING FOR BRAIN STROKE MONITORING," *Prog. Electromagn. Res. B*, vol. 40, pp. 305–324, 2012, doi: 10.2528/PIERB12022006.

[55] J. A. Tobon Vasquez *et al.*, "A Prototype Microwave System for 3D Brain Stroke Imaging," *Sensors*, vol. 20, no. 9, p. 2607, May 2020, doi: 10.3390/s20092607.

[56] S. Y. Semenov, A. E. Bulyshev, V. G. Posukh, Y. E. Sizov, T. C. Williams, and A. E. Souvorov, "Microwave Tomography for Detection/Imaging of Myocardial Infarction. I. Excised Canine Hearts," *Ann. Biomed. Eng.*, vol. 31, no. 3, pp. 262–270, Mar. 2003, doi: 10.1114/1.1553452.

[57] P. M. Meaney *et al.*, "Clinical Microwave Tomographic Imaging of the Calcaneus: A First-in-Human Case Study of Two Subjects," *IEEE Trans. Biomed. Eng.*, vol. 59, no. 12, pp. 3304–3313, Dec. 2012, doi: 10.1109/TBME.2012.2209202.

[58] J. E. Fajardo, F. P. Lotto, F. Vericat, C. M. Carlevaro, and R. M. Irastorza, "Microwave tomography with phaseless data on the calcaneus by means of artificial neural networks," *Med. Biol. Eng. Comput.*, vol. 58, no. 2, pp. 433–442, Feb. 2020, doi: 10.1007/s11517-019-02090-y.

[59] C. Gilmore, A. Zakaria, S. Pistorius, and J. LoVetri, "Microwave Imaging of Human Forearms: Pilot Study and Image Enhancement," *Int. J. Biomed. Imaging*, vol. 2013, pp. 1–17, 2013, doi: 10.1155/2013/673027.

[60] B. Amin *et al.*, "A feasibility study on microwave imaging of bone for osteoporosis monitoring," *Med. Biol. Eng. Comput.*, vol. 59, no. 4, pp. 925–936, Apr. 2021, doi: 10.1007/s11517-021-02344-8.

[61] E. Porter, M. Coates, and M. Popovic, "An Early Clinical Study of Time-Domain Microwave Radar for Breast Health Monitoring," *IEEE Trans. Biomed. Eng.*, vol. 63, no. 3, pp. 530–539, Mar. 2016, doi: 10.1109/TBME.2015.2465867.

[62] T. M. Grzegorczyk, P. M. Meaney, P. A. Kaufman, R. M. Di Florio-Alexander, and K. D. Paulsen, "Fast 3-D Tomographic Microwave Imaging for Breast Cancer Detection," *IEEE Trans. Med. Imaging*, vol. 31, no. 8, pp. 1584–1592, Aug. 2012, doi: 10.1109/TMI.2012.2197218.

[63] A. Fasoula *et al.*, "Pilot patient study with the Wavelia Microwave Breast Imaging system for breast cancer detection: Clinical feasibility and identified technical challenges," in *2020 14th European Conference on*

Antennas and Propagation (EuCAP), Copenhagen, Denmark: IEEE, Mar. 2020, pp. 1–5. doi: 10.23919/EuCAP48036.2020.9135549.

[64] M. T. Bevacqua, G. G. Bellizzi, T. Isernia, and L. Crocco, "A METHOD FOR EFFECTIVE PERMITTIVITY AND CONDUCTIVITY MAPPING OF BIOLOGICAL SCENARIOS VIA SEGMENTED CONTRAST SOURCE INVERSION," *Prog. Electromagn. Res.*, vol. 164, pp. 1–15, 2019, doi: 10.2528/PIER18071704.

[65] M. T. Bevacqua, G. G. Bellizzi, L. Crocco, and T. Isernia, "A method for quantitative imaging of electrical properties of human tissues from only amplitude electromagnetic data," *Inverse Probl.*, vol. 35, no. 2, p. 025006, Feb. 2019, doi: 10.1088/1361-6420/aaf5b8.

[66] P. E. Summers *et al.*, "Towards mm-wave spectroscopy for dielectric characterization of breast surgical margins," *The Breast*, vol. 45, pp. 64–69, Jun. 2019, doi: 10.1016/j.breast.2019.02.008.

[67] A. Martellosio *et al.*, "Dielectric Properties Characterization From 0.5 to 50 GHz of Breast Cancer Tissues," *IEEE Trans. Microw. Theory Tech.*, vol. 65, no. 3, pp. 998–1011, Mar. 2017, doi: 10.1109/TMTT.2016.2631162.

[68] M. Lazebnik *et al.*, "A large-scale study of the ultrawideband microwave dielectric properties of normal breast tissue obtained from reduction surgeries," *Phys. Med. Biol.*, vol. 52, no. 10, pp. 2637–2656, May 2007, doi: 10.1088/0031-9155/52/10/001.

[69] S. Di Meo *et al.*, "Experimental validation of the dielectric permittivity of breast cancer tissues up to 50 GHz," in *2017 IEEE MTT-S International Microwave Workshop Series on Advanced Materials and Processes for RF and THz Applications (IMWS-AMP)*, Pavia: IEEE, Sep. 2017, pp. 1–3. doi: 10.1109/IMWS-AMP.2017.8247408.

[70] S. Di Meo *et al.*, "Dielectric properties of breast tissues: experimental results up to 50 GHz," in *12th European Conference on Antennas and Propagation (EuCAP 2018)*, London, UK: Institution of Engineering and Technology, 2018, p. 572 (5 pp.)-572 (5 pp.). doi: 10.1049/cp.2018.0931.

[71] E. Porter, J. Fakhoury, R. Oprisor, M. Coates, and M. Popovi, "Improved tissue phantoms for experimental validation of microwave breast cancer detection".

[72] T. A. Krouskop, T. M. Wheeler, F. Kallel, B. S. Garra, and T. Hall, "Elastic Moduli of Breast and Prostate Tissues under Compression," *Ultrason. Imaging*, vol. 20, no. 4, pp. 260–274, Oct. 1998, doi: 10.1177/016173469802000403.

[73] A. Cannata, M. Pasian, S. Di Meo, G. Matrone, and S. Morganti, "Dielectric, Mechanical and Acoustic Characterization of Multi-Modal Tissue-Mimicking Breast Phantoms," in *2022 IEEE International Ultrasonics Symposium (IUS)*, Venice, Italy: IEEE, Oct. 2022, pp. 1–4. doi: 10.1109/IUS54386.2022.9958752.

[74] E. L. Madsen, J. A. Zagzebski, and G. R. Frank, "Oil-in-gelatin dispersions for use as ultrasonically tissue-mimicking materials," *Ultrasound Med. Biol.*, vol. 8, no. 3, pp. 277–287, Jan. 1982, doi: 10.1016/0301-5629(82)90034-5.

[75] L. M. Cannon, A. J. Fagan, and J. E. Browne, "Novel Tissue Mimicking Materials for High Frequency Breast Ultrasound Phantoms," *Ultrasound*

Med. Biol., vol. 37, no. 1, pp. 122–135, Jan. 2011, doi: 10.1016/j.ultrasmedbio.2010.10.005.

[76] A. Józefczak, K. Kaczmarek, M. Kubovčíková, Z. Rozynek, and T. Hornowski, "The effect of magnetic nanoparticles on the acoustic properties of tissue-mimicking agar-gel phantoms," *J. Magn. Magn. Mater.*, vol. 431, pp. 172–175, Jun. 2017, doi: 10.1016/j.jmmm.2016.09.118.

[77] J. Dahmani, C. Laporte, D. Pereira, P. Belanger, and Y. Petit, "Predictive Model for Designing Soft-Tissue Mimicking Ultrasound Phantoms With Adjustable Elasticity," *IEEE Trans. Ultrason. Ferroelectr. Freq. Control*, vol. 67, no. 4, pp. 715–726, Apr. 2020, doi: 10.1109/TUFFC.2019.2953190.

[78] J. E. Browne, K. V. Ramnarine, A. J. Watson, and P. R. Hoskins, "Assessment of the acoustic properties of common tissue-mimicking test phantoms," *Ultrasound Med. Biol.*, vol. 29, no. 7, pp. 1053–1060, Jul. 2003, doi: 10.1016/S0301-5629(03)00053-X.

[79] T. J. Hall, M. Bilgen, M. F. Insana, and T. A. Krouskop, "Phantom materials for elastography," *IEEE Trans. Ultrason. Ferroelectr. Freq. Control*, vol. 44, no. 6, pp. 1355–1365, Nov. 1997, doi: 10.1109/58.656639.

[80] K. Zell, J. I. Sperl, M. W. Vogel, R. Niessner, and C. Haisch, "Acoustical properties of selected tissue phantom materials for ultrasound imaging," *Phys. Med. Biol.*, vol. 52, no. 20, pp. N475–N484, Oct. 2007, doi: 10.1088/0031-9155/52/20/N02.

[81] E. Lennie, C. Tsoumpas, and S. Sourbron, "Multimodal phantoms for clinical PET/MRI," *EJNMMI Phys.*, vol. 8, no. 1, p. 62, Dec. 2021, doi: 10.1186/s40658-021-00408-0.

[82] Y. He *et al.*, "3D-printed breast phantom for multi-purpose and multi-modality imaging," *Quant. Imaging Med. Surg.*, vol. 9, no. 1, pp. 63–74, Jan. 2019, doi: 10.21037/qims.2019.01.05.

[83] A. Ali, R. Wahab, J. Huynh, N. Wake, and M. Mahoney, "Imaging properties of 3D printed breast phantoms for lesion localization and Core needle biopsy training," *3D Print. Med.*, vol. 6, no. 1, p. 4, Dec. 2020, doi: 10.1186/s41205-020-00058-5.

[84] L. Di Sieno *et al.*, "Solid heterogeneous phantoms for multimodal ultrasound and diffuse optical imaging: an outcome of the SOLUS project for standardization," in *Novel Biophotonics Techniques and Applications V*, A. Amelink and S. K. Nadkarni, Eds., Munich, Germany: SPIE, Jul. 2019, p. 39. doi: 10.1117/12.2526645.

[85] K. J. Parker, M. M. Doyley, and D. J. Rubens, "Imaging the elastic properties of tissue: the 20 year perspective," *Phys. Med. Biol.*, vol. 56, no. 1, pp. R1–R29, Jan. 2011, doi: 10.1088/0031-9155/56/1/R01.

[86] S. Y. Ng and C. L. Lin, "Tunability of Acoustic and Mechanical Behaviors in Breast Tissue Mimicking Materials," in *2019 41st Annual International Conference of the IEEE Engineering in Medicine and Biology Society (EMBC)*, Berlin, Germany: IEEE, Jul. 2019, pp. 1998–2002. doi: 10.1109/EMBC.2019.8857843.

[87] S. Di Meo, A. Cannata, C. Macchello, S. Morganti, M. Pasian, and G. Matrone, "Bi-modal tissue-mimicking breast phantoms: comparison between the performance of agar- and gelatin-based phantoms," in *2022 3rd URSI Atlantic and Asia Pacific Radio Science Meeting (AT-AP-RASC)*,

Gran Canaria, Spain: IEEE, May 2022, pp. 1–4. doi: 10.23919/AT-AP-RASC54737.2022.9814414.

[88] D. A. G. Bruggeman, "Berechnung verschiedener physikalischer Konstanten von heterogenen Substanzen. I. Dielektrizitätskonstanten und Leitfähigkeiten der Mischkörper aus isotropen Substanzen," *Ann. Phys.*, vol. 416, no. 7, pp. 636–664, Jan. 1935, doi: 10.1002/andp.19354160705.

[89] A. Cannata, S. Di Meo, S. Morganti, G. Matrone, and M. Pasian, "Gelatin-Based Tissue-Mimicking Materials for Breast Phantoms: Dielectric and Mechanical Characterization," in *2021 XXXIVth General Assembly and Scientific Symposium of the International Union of Radio Science (URSI GASS)*, Rome, Italy: IEEE, Aug. 2021, pp. 1–3. doi: 10.23919/URSIGASS51995.2021.9560361.

[90] C. Gabriel, "The Dielectric Properties of Biological Materials," in *Radiofrequency Radiation Standards*, B. J. Klauenberg, M. Grandolfo, and D. N. Erwin, Eds., Boston, MA: Springer US, 1995, pp. 187–196. doi: 10.1007/978-1-4899-0945-9_20.

[91] S. Cruciani, V. D. Santis, M. Feliziani, and F. Maradei, "Cole-Cole vs Debye models for the assessment of electromagnetic fields inside biological tissues produced by wideband EMF sources," in *2012 Asia-Pacific Symposium on Electromagnetic Compatibility*, Singapore, Singapore: IEEE, May 2012, pp. 685–688. doi: 10.1109/APEMC.2012.6237915.

[92] K. Miller, "Method of testing very soft biological tissues in compression," *J. Biomech.*, vol. 38, no. 1, pp. 153–158, Jan. 2005, doi: 10.1016/j.jbiomech.2004.03.004.

[93] H. Zhou, M. Goss, C. Hernandez, J. M. Mansour, and A. Exner, "Validation of Ultrasound Elastography Imaging for Nondestructive Characterization of Stiffer Biomaterials," *Ann. Biomed. Eng.*, vol. 44, no. 5, pp. 1515–1523, May 2016, doi: 10.1007/s10439-015-1448-7.

[94] P. S. Wellman, R. D. Howe, E. Dalton, and K. A. Kern, "Breast Tissue Stiffness in Compression is Correlated to Histological Diagnosis".

[95] S. A. Kruse *et al.*, "Tissue characterization using magnetic resonance elastography: preliminary results*," *Phys. Med. Biol.*, vol. 45, no. 6, pp. 1579–1590, Jun. 2000, doi: 10.1088/0031-9155/45/6/313.

[96] A. Samani, J. Bishop, C. Luginbuhl, and D. B. Plewes, "Measuring the elastic modulus of *ex vivo* small tissue samples," *Phys. Med. Biol.*, vol. 48, no. 14, pp. 2183–2198, Jul. 2003, doi: 10.1088/0031-9155/48/14/310.

[97] T. Matsumura *et al.*, "Measurement of elastic property of breast tissue for elasticity imaging," in *2009 IEEE International Ultrasonics Symposium*, Rome, Italy: IEEE, Sep. 2009, pp. 1451–1454. doi: 10.1109/ULTSYM.2009.5442044.

[98] T. Umemoto *et al.*, "Ex Vivo and In Vivo Assessment of the Non-linearity of Elasticity Properties of Breast Tissues for Quantitative Strain Elastography," *Ultrasound Med. Biol.*, vol. 40, no. 8, pp. 1755–1768, Aug. 2014, doi: 10.1016/j.ultrasmedbio.2014.02.005.

[99] M. Qiu *et al.*, "Study on temperature dependent broadband frequency dielectric spectrum of SD rat muscle tissues," in *2015 IEEE 11th International Conference on the Properties and Applications of Dielectric Materials (ICPADM)*, Sydney, NSW: IEEE, Jul. 2015, pp. 828–831. doi: 10.1109/ICPADM.2015.7295400.

[100] H. Fallahi, J. Sebek, and P. Prakash, "Broadband Dielectric Properties of *Ex Vivo* Bovine Liver Tissue Characterized at Ablative Temperatures," *IEEE Trans. Biomed. Eng.*, vol. 68, no. 1, pp. 90–98, Jan. 2021, doi: 10.1109/TBME.2020.2996825.

[101] P. Tortoli, L. Bassi, E. Boni, A. Dallai, F. Guidi, and S. Ricci, "ULA-OP: an advanced open platform for ultrasound research," *IEEE Trans. Ultrason. Ferroelectr. Freq. Control*, vol. 56, no. 10, pp. 2207–2216, Oct. 2009, doi: 10.1109/TUFFC.2009.1303.

[102] E. Cetin, H. O. Durmus, B. Karaboce, and N. Kavakli, "Acoustical Characterization of Tissue - Mimicking Materials," in *2019 IEEE International Symposium on Medical Measurements and Applications (MeMeA)*, Istanbul, Turkey: IEEE, Jun. 2019, pp. 1–5. doi: 10.1109/MeMeA.2019.8802203.

[103] A. Samani, J. Zubovits, and D. Plewes, "Elastic moduli of normal and pathological human breast tissues: an inversion-technique-based investigation of 169 samples," *Phys. Med. Biol.*, vol. 52, no. 6, pp. 1565–1576, Mar. 2007, doi: 10.1088/0031-9155/52/6/002.

[104] A. Samani and D. Plewes, "An inverse problem solution for measuring the elastic modulus of intact *ex vivo* breast tissue tumours," *Phys. Med. Biol.*, vol. 52, no. 5, pp. 1247–1260, Mar. 2007, doi: 10.1088/0031-9155/52/5/003.

[105] C. Dietrich *et al.*, "Strain Elastography - How To Do It?," *Ultrasound Int. Open*, vol. 03, no. 04, pp. E137–E149, Sep. 2017, doi: 10.1055/s-0043-119412.

[106] A. L. McKnight, J. L. Kugel, P. J. Rossman, A. Manduca, L. C. Hartmann, and R. L. Ehman, "MR Elastography of Breast Cancer: Preliminary Results," *Am. J. Roentgenol.*, vol. 178, no. 6, pp. 1411–1417, Jun. 2002, doi: 10.2214/ajr.178.6.1781411.

[107] A. Srivastava, Y. Verma, K. D. Rao, and P. K. Gupta, "Determination of Elastic Properties of Resected Human Breast Tissue Samples Using Optical Coherence Tomographic Elastography," *Strain*, vol. 47, no. 1, pp. 75–87, Feb. 2011, doi: 10.1111/j.1475-1305.2009.00627.x.

[108] A. P. Sarvazyan *et al.*, "Biophysical Bases of Elasticity Imaging," in *Acoustical Imaging*, vol. 21, J. P. Jones, Ed., in Acoustical Imaging, vol. 21. , Boston, MA: Springer US, 1995, pp. 223–240. doi: 10.1007/978-1-4615-1943-0_23.

[109] A. Manduca *et al.*, "Magnetic resonance elastography: Non-invasive mapping of tissue elasticity," *Med. Image Anal.*, vol. 5, no. 4, pp. 237–254, Dec. 2001, doi: 10.1016/S1361-8415(00)00039-6.

[110] S. Di Meo, L. Pasotti, M. Pasian, and G. Matrone, "On the Conservation of Materials for Breast Phantoms in the Frequency Range 0.5-50 GHz," in *2018 48th European Microwave Conference (EuMC)*, Madrid: IEEE, Sep. 2018, pp. 320–323. doi: 10.23919/EuMC.2018.8541677.

[111] S. Di Meo *et al.*, "Multi-Layer Tissue-Mimicking Breast Phantoms for Microwave-Based Imaging Systems," *IEEE J. Electromagn. RF Microw. Med. Biol.*, pp. 1–9, 2024, doi: 10.1109/JERM.2024.3379750.

[112] S. Di Meo *et al.*, "Development of Multi-Layer Tissue-Mimicking Breast Phantoms for Microwaves and Millimeter-Waves Imaging," in *2023 IEEE MTT-S International Microwave Biomedical Conference (IMBioC)*,

Leuven, Belgium: IEEE, Sep. 2023, pp. 103–105. doi: 10.1109/IMBioC56839.2023.10305139.

[113] M. Klemm, I. J. Craddock, J. A. Leendertz, A. Preece, and R. Benjamin, "Radar-Based Breast Cancer Detection Using a Hemispherical Antenna Array—Experimental Results," *IEEE Trans. Antennas Propag.*, vol. 57, no. 6, pp. 1692–1704, Jun. 2009, doi: 10.1109/TAP.2009.2019856.

[114] E. C. Fear, J. Bourqui, C. Curtis, D. Mew, B. Docktor, and C. Romano, "Microwave Breast Imaging With a Monostatic Radar-Based System: A Study of Application to Patients," *IEEE Trans. Microw. Theory Tech.*, vol. 61, no. 5, pp. 2119–2128, May 2013, doi: 10.1109/TMTT.2013.2255884.

[115] H. Bahramiabarghouei, E. Porter, A. Santorelli, B. Gosselin, M. Popovic, and L. A. Rusch, "Flexible 16 Antenna Array for Microwave Breast Cancer Detection," *IEEE Trans. Biomed. Eng.*, vol. 62, no. 10, pp. 2516–2525, Oct. 2015, doi: 10.1109/TBME.2015.2434956.

[116] M. J. Burfeindt, J. D. Shea, B. D. Van Veen, and S. C. Hagness, "Beamforming-Enhanced Inverse Scattering for Microwave Breast Imaging," *IEEE Trans. Antennas Propag.*, vol. 62, no. 10, pp. 5126–5132, Oct. 2014, doi: 10.1109/TAP.2014.2344096.

[117] M. Lazebnik *et al.*, "A large-scale study of the ultrawideband microwave dielectric properties of normal, benign and malignant breast tissues obtained from cancer surgeries," *Phys. Med. Biol.*, vol. 52, no. 20, pp. 6093–6115, Oct. 2007, doi: 10.1088/0031-9155/52/20/002.

[118] S. Di Meo *et al.*, "Correlation Between Dielectric Properties and Women Age for Breast Cancer Detection at 30 GHz," in *2018 IEEE International Microwave Biomedical Conference (IMBioC)*, Philadelphia, PA: IEEE, Jun. 2018, pp. 190–192. doi: 10.1109/IMBIOC.2018.8428851.

[119] R. Matthes and J. H. Bernhardt, Eds., *Guidelines on limiting exposure to non-ionizing radiation: a reference book based on the guidelines on limiting exposure to non-ionizing radiation and statements on special applications*. in ICNIRP, no. 7. Oberschleißheim: International Commission on Non-Ionizing Radiation Protection, 1999.

[120] E. Boni *et al.*, "Architecture of an Ultrasound System for Continuous Real-Time High Frame Rate Imaging," *IEEE Trans. Ultrason. Ferroelectr. Freq. Control*, vol. 64, no. 9, pp. 1276–1284, Sep. 2017, doi: 10.1109/TUFFC.2017.2727980.

[121] S. Di Meo, M. T. Bevacqua, G. Matrone, L. Crocco, T. Isernia, and M. Pasian, "Millimeter-wave breast cancer imaging by means of a dual-step approach combining radar and tomographic techniques: preliminary results," in *2022 44th Annual International Conference of the IEEE Engineering in Medicine & Biology Society (EMBC)*, Glasgow, Scotland, United Kingdom: IEEE, Jul. 2022, pp. 508–511. doi: 10.1109/EMBC48229.2022.9871999.

[122] Xu Li and S. C. Hagness, "A confocal microwave imaging algorithm for breast cancer detection," *IEEE Microw. Wirel. Compon. Lett.*, vol. 11, no. 3, pp. 130–132, Mar. 2001, doi: 10.1109/7260.915627.

[123] R. Nilavalan, A. Gbedemah, I. J. Craddock, X. Li, and S. C. Hagness, "Numerical investigation of breast tumour detection using multi-static radar," *Electron. Lett.*, vol. 39, no. 25, p. 1787, 2003, doi: 10.1049/el:20031183.

[124] S. K. Davis, H. Tandradinata, S. C. Hagness, and B. D. VanVeen, "Ultrawideband Microwave Breast Cancer Detection: A Detection-Theoretic Approach Using the Generalized Likelihood Ratio Test," *IEEE Trans. Biomed. Eng.*, vol. 52, no. 7, pp. 1237–1250, Jul. 2005, doi: 10.1109/TBME.2005.847528.

[125] P. Kosmas and C. M. Rappaport, "FDTD-based time reversal for microwave breast cancer Detection-localization in three dimensions," *IEEE Trans. Microw. Theory Tech.*, vol. 54, no. 4, pp. 1921–1927, Jun. 2006, doi: 10.1109/TMTT.2006.871994.

[126] M. Mozaffarzadeh, M. Sadeghi, A. Mahloojifar, and M. Orooji, "Double-Stage Delay Multiply and Sum Beamforming Algorithm Applied to Ultrasound Medical Imaging," *Ultrasound Med. Biol.*, vol. 44, no. 3, pp. 677–686, Mar. 2018, doi: 10.1016/j.ultrasmedbio.2017.10.020.

[127] G. Matrone, A. S. Savoia, G. Caliano, and G. Magenes, "The Delay Multiply and Sum Beamforming Algorithm in Ultrasound B-Mode Medical Imaging," *IEEE Trans. Med. Imaging*, vol. 34, no. 4, pp. 940–949, Apr. 2015, doi: 10.1109/TMI.2014.2371235.

[128] P. M. Oliveira and V. Barroso, "Uncertainty in the time-frequency plane," in *Proceedings of the Tenth IEEE Workshop on Statistical Signal and Array Processing (Cat. No.00TH8496)*, Pocono Manor, PA, USA: IEEE, 2000, pp. 607–611. doi: 10.1109/SSAP.2000.870197.

[129] M. A. Stuchly and E. C. Fear, "Microwave detection of breast cancer," *IEEE Trans. Microw. Theory Tech.*, vol. 48, no. 11, pp. 1854–1863, Nov. 2000, doi: 10.1109/22.883862.

[130] S. H. Ignacio Barboza, J. A. Amaya Palacio, E. Pontes, and S. T. Kofuji, "Fifth derivative Gaussian pulse generator for UWB Breast Cancer Detection System," in *2014 IEEE International Conference on Ultra-WideBand (ICUWB)*, Paris, France: IEEE, Sep. 2014, pp. 269–273. doi: 10.1109/ICUWB.2014.6958991.

[131] S. S. Ahmed, A. Schiessl, and L.-P. Schmidt, "A Novel Fully Electronic Active Real-Time Imager Based on a Planar Multistatic Sparse Array," *IEEE Trans. Microw. Theory Tech.*, vol. 59, no. 12, pp. 3567–3576, Dec. 2011, doi: 10.1109/TMTT.2011.2172812.

[132] M. T. Bevacqua, S. Di Meo, L. Crocco, T. Isernia, and M. Pasian, "Millimeter-Waves Breast Cancer Imaging via Inverse Scattering Techniques," *IEEE J. Electromagn. RF Microw. Med. Biol.*, vol. 5, no. 3, pp. 246–253, Sep. 2021, doi: 10.1109/JERM.2021.3052096.

[133] I. Iliopoulos *et al.*, "Enhancement of Penetration of Millimeter Waves by Field Focusing Applied to Breast Cancer Detection," *IEEE Trans. Biomed. Eng.*, vol. 68, no. 3, pp. 959–966, Mar. 2021, doi: 10.1109/TBME.2020.3014277.

[134] B. Amin *et al.*, "Dielectric characterization of diseased human trabecular bones at microwave frequency," *Med. Eng. Phys.*, vol. 78, pp. 21–28, Apr. 2020, doi: 10.1016/j.medengphy.2020.01.014.

[135] Office of the Surgeon General (US), *Bone Health and Osteoporosis: A Report of the Surgeon General*. in Reports of the Surgeon General. Rockville (MD): Office of the Surgeon General (US), 2004. Accessed: Aug. 12, 2024. [Online]. Available: http://www.ncbi.nlm.nih.gov/books/NBK45513/

[136] P. M. Meaney, T. Zhou, D. Goodwin, A. Golnabi, E. A. Attardo, and K. D. Paulsen, "Bone Dielectric Property Variation as a Function of Mineralization at Microwave Frequencies," *Int. J. Biomed. Imaging*, vol. 2012, pp. 1–9, 2012, doi: 10.1155/2012/649612.

[137] M. Azghani, P. Kosmas, and F. Marvasti, "Microwave Medical Imaging Based on Sparsity and an Iterative Method With Adaptive Thresholding," *IEEE Trans. Med. Imaging*, vol. 34, no. 2, pp. 357–365, Feb. 2015, doi: 10.1109/TMI.2014.2352113.

[138] Z. Miao and P. Kosmas, "Multiple-Frequency DBIM-TwIST Algorithm for Microwave Breast Imaging," *IEEE Trans. Antennas Propag.*, vol. 65, no. 5, pp. 2507–2516, May 2017, doi: 10.1109/TAP.2017.2679067.

[139] L. M. Neira, B. D. Van Veen, and S. C. Hagness, "High-Resolution Microwave Breast Imaging Using a 3-D Inverse Scattering Algorithm With a Variable-Strength Spatial Prior Constraint," *IEEE Trans. Antennas Propag.*, vol. 65, no. 11, pp. 6002–6014, Nov. 2017, doi: 10.1109/TAP.2017.2751668.

[140] B. Amin, M. A. Elahi, A. Shahzad, E. Porter, B. McDermott, and M. O'Halloran, "Dielectric properties of bones for the monitoring of osteoporosis," *Med. Biol. Eng. Comput.*, vol. 57, no. 1, pp. 1–13, Jan. 2019, doi: 10.1007/s11517-018-1887-z.

[141] I. Catapano *et al.*, "ON QUANTITATIVE MICROWAVE TOMOGRAPHY OF FEMALE BREAST," *Prog. Electromagn. Res.*, vol. 97, pp. 75–93, 2009, doi: 10.2528/PIER09080604.

[142] M. Alkhodari, A. Zakaria, and N. Qaddoumi, "Monitoring Bone Density Using Microwave Tomography of Human Legs: A Numerical Feasibility Study," *Sensors*, vol. 21, no. 21, p. 7078, Oct. 2021, doi: 10.3390/s21217078.

[143] M. Ambrosanio, P. Kosmas, and V. Pascazio, "A Multithreshold Iterative DBIM-Based Algorithm for the Imaging of Heterogeneous Breast Tissues," *IEEE Trans. Biomed. Eng.*, vol. 66, no. 2, pp. 509–520, Feb. 2019, doi: 10.1109/TBME.2018.2849648.

[144] B. Khalesi, B. Sohani, N. Ghavami, M. Ghavami, S. Dudley, and G. Tiberi, "Free-Space Operating Microwave Imaging Device for Bone Lesion Detection: A Phantom Investigation," *IEEE Antennas Wirel. Propag. Lett.*, vol. 19, no. 12, pp. 2393–2397, Dec. 2020, doi: 10.1109/LAWP.2020.3034039.

[145] K. C. Santos, C. A. Fernandes, and J. R. Costa, "Validation of a Compact Microwave Imaging System for Bone Fracture Detection," *IEEE Access*, vol. 11, pp. 63690–63700, 2023, doi: 10.1109/ACCESS.2023.3287486.

[146] Y. Jiang, M. Liu, and T. Li, "Feasibility Analysis Of Bone Abnormality Diagnosis Based On Microwave Technology," in *2022 3rd International Conference on Computer Vision, Image and Deep Learning & International Conference on Computer Engineering and Applications (CVIDL & ICCEA)*, Changchun, China: IEEE, May 2022, pp. 926–930. doi: 10.1109/CVIDLICCEA56201.2022.9825307.

[147] A. Cannatà *et al.*, "Microwave Tomography Bone Imaging: Analysing the Impact of Skin Thickness on the Reconstruction of Numerical Bone Phantoms," in *2024 18th European Conference on Antennas and*

Propagation (EuCAP), Glasgow, United Kingdom: IEEE, Mar. 2024, pp. 1–5. doi: 10.23919/EuCAP60739.2024.10501621.

[148] Z. Wang, A. C. Bovik, H. R. Sheikh, and E. P. Simoncelli, "Image Quality Assessment: From Error Visibility to Structural Similarity," *IEEE Trans. Image Process.*, vol. 13, no. 4, pp. 600–612, Apr. 2004, doi: 10.1109/TIP.2003.819861.

[149] S. Gabriel, R. W. Lau, and C. Gabriel, "The dielectric properties of biological tissues: III. Parametric models for the dielectric spectrum of tissues," *Phys. Med. Biol.*, vol. 41, no. 11, pp. 2271–2293, Nov. 1996, doi: 10.1088/0031-9155/41/11/003.

[150] P. Meaney, S. Geimer, A. Golnabi, and K. Paulsen, "Impact of Skin on Microwave Tomography in the Lossy Coupling Medium," *Sensors*, vol. 22, no. 19, p. 7353, Sep. 2022, doi: 10.3390/s22197353.

[151] A. Shahzad, M. O'Halloran, E. Jones, and M. Glavin, "A multistage selective weighting method for improved microwave breast tomography," *Comput. Med. Imaging Graph.*, vol. 54, pp. 6–15, Dec. 2016, doi: 10.1016/j.compmedimag.2016.08.007.

[152] B. Amin, A. Shahzad, D. Kelly, M. O'Halloran, and M. Adnan Elahi, "Anthropomorphic Calcaneus Phantom for Microwave Bone Imaging Applications," *IEEE J. Electromagn. RF Microw. Med. Biol.*, vol. 5, no. 3, pp. 206–213, Sep. 2021, doi: 10.1109/JERM.2020.3029938.

[153] N. Joachimowicz, B. Duchene, C. Conessa, and O. Meyer, "Reference phantoms for microwave imaging," in *2017 11th European Conference on Antennas and Propagation (EUCAP)*, Paris, France: IEEE, Mar. 2017, pp. 2719–2722. doi: 10.23919/EuCAP.2017.7928497.

[154] N. Joachimowicz, B. Duchene, C. Conessa, and O. Meyer, "Easy-to-produce adjustable realistic breast phantoms for microwave imaging," in *2016 10th European Conference on Antennas and Propagation (EuCAP)*, Davos, Switzerland: IEEE, Apr. 2016, pp. 1–4. doi: 10.1109/EuCAP.2016.7481715.

[155] D. O'Loughlin *et al.*, "Sensitivity and Specificity Estimation Using Patient-Specific Microwave Imaging in Diverse Experimental Breast Phantoms," *IEEE Trans. Med. Imaging*, vol. 38, no. 1, pp. 303–311, Jan. 2019, doi: 10.1109/TMI.2018.2864150.

[156] B. L. Oliveira, D. O'Loughlin, M. O'Halloran, E. Porter, M. Glavin, and E. Jones, "Microwave Breast Imaging: experimental tumour phantoms for the evaluation of new breast cancer diagnosis systems," *Biomed. Phys. Eng. Express*, vol. 4, no. 2, p. 025036, Feb. 2018, doi: 10.1088/2057-1976/aaaaff.

[157] A. Fhager, S. K. Padhi, and J. Howard, "3D Image Reconstruction in Microwave Tomography Using an Efficient FDTD Model," *IEEE Antennas Wirel. Propag. Lett.*, vol. 8, pp. 1353–1356, 2009, doi: 10.1109/LAWP.2009.2039032.

[158] R. Ciocan and H. Jiang, "Model-based microwave image reconstruction: simulations and experiments: Model-based microwave image reconstruction: simulations and experiments," *Med. Phys.*, vol. 31, no. 12, pp. 3231–3241, Dec. 2004, doi: 10.1118/1.1812871.

[159] C. Gabriel and A. Peyman, "Dielectric measurement: error analysis and assessment of uncertainty," *Phys. Med. Biol.*, vol. 51, no. 23, pp. 6033–6046, Dec. 2006, doi: 10.1088/0031-9155/51/23/006.